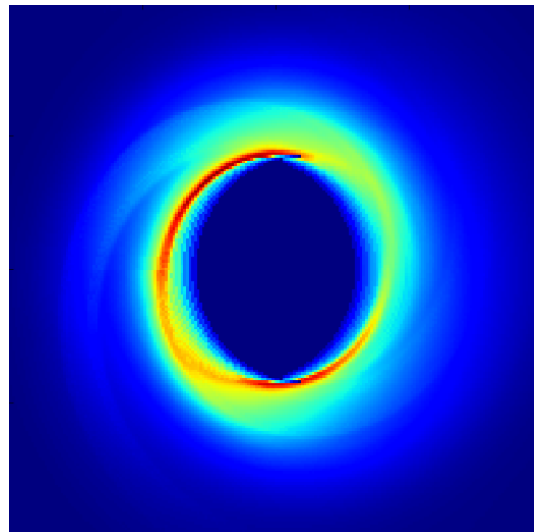


# Modeling the dusty disk surrounding the post-AGB binary V390 Vel



**Ilya STRAUMIT**

Supervisor: Dr. Jacques Kluska  
Institute of Astronomy, KU Leuven

Co-supervisor: Prof. Dr. Hans Van Winckel  
Institute of Astronomy, KU Leuven

Thesis presented in  
fulfillment of the requirements  
for the degree of Master of Science  
in Astronomy and Astrophysics

© Copyright by KU Leuven

Without written permission of the promotors and the authors it is forbidden to reproduce or adapt in any form or by any means any part of this publication. Requests for obtaining the right to reproduce or utilize parts of this publication should be addressed to KU Leuven, Faculteit Wetenschappen, Geel Huis, Kasteelpark Arenberg 11 bus 2100, 3001 Leuven (Heverlee), Telephone +32 16 32 14 01.

A written permission of the promotor is also required to use the methods, products, schematics and programs described in this work for industrial or commercial use, and for submitting this publication in scientific contests.

# Summary for a general audience

At the end of their lives, solar-like stars loose most of their mass in an intense episode of stellar wind and end up as remnants consisting of primarily carbon and oxygen. The ejected matter is in a form of a gas and, as it moves away from the star, it cools down and condenses to form dust grains. Binary stellar systems, which are two stars orbiting each other, follow a similar path, although the presence of a second star perturbs the way the mass is lost from the most evolved star. Part of the ejected mass forms a stable disk, surrounding the two stars, where dust particles move in an orbit under the influence of the gravity from the central binary. Formation of such disks, as well as their interaction with the host binary systems is currently not well understood. One can observe the effects of the disk-binary interaction such as the perturbation of the orbit of the binary by the disk. High angular resolution observations by interferometry (observing technique consisting in combining the light of two or more telescopes) revealed complex morphology of disks around binary systems, showing the presence of spiral arms or asymmetric appearance of the disk. Understanding the mechanisms that produce these features is important for attaining a complete picture of stellar evolution in binary systems. In this work, we study an evolved binary system V390 Velorum, which is known to contain a dusty disk, asymmetric in brightness. We attempt to explain the origin of this asymmetry by constructing a computational model of the disk that allows us to simulate the heating of the disk by the central star and the propagation of light inside it. Based on our model we construct simulated images of the disk and compare them to the observational data.

# Scientific summary

It is now well established that all post-AGB systems with disks are binaries. Disks around binary post-AGB systems are formed by the gas and dust ejected from the central star after a period of strong binary interaction at the end of the AGB stage. Binary evolution channels of post-AGB systems are currently not well understood, which is evident from the mismatch of model predictions with the observational data. In particular, a large number of eccentric post-AGB systems with long orbital periods is unexplained because the orbits of such systems are known to be efficiently circularized at certain stages in their evolution. One mechanism that could potentially explain the existence of such systems is the perturbation of the binary by the disk, resulting in the increased eccentricity of the system (eccentricity pumping). Better understanding of this disk-binary interaction requires knowledge of the structure of disks in post-AGB binary systems. Observations show that this structure can be quite complex, featuring spiral density waves or azimuthal asymmetry. In this work we study a binary post-AGB system V390 Vel, which is known to contain a dusty disk. The brightness distribution from the disk was previously reconstructed from the interferometric data. The aim of this thesis is to reproduce the observed brightness distribution by constructing a radiative transfer model of the disk in V390 Vel.

V390 Vel is a binary with an orbital period of 506 days and an eccentricity 0.22. Near-infrared interferometric image reconstruction of the inner parts of the disk around V390 Vel shows a non-centro-symmetric brightness distribution of the disk and features two local maxima at approximately opposite sides of the disk's inner rim. Our working hypothesis is that this asymmetry is caused by the asymmetric irradiation of the disk by the primary, which is located closer to one side of the disk due to the fact that it is a part of a binary. In addition, we study the effect of density enhancements such as spiral waves in the disk, on the brightness distribution.

In order to establish an approach that is the most suitable for the modeling of the disk around V390 Vel, we first study micro-scale processes in the disk: dynamics of thermal interaction between dust, gas and radiation, and the dynamics of dust sublimation. Of particular interest are the timescales of thermal equili-

bration of the dust grains with the radiation field, and cooling of the dust grains by the gas. Our calculations show that dust grains achieve thermal equilibrium with radiation on a timescale much shorter than the orbital period, and that the cooling of the dust by the gas is negligible and cannot shift the temperature of the grains away from the point of equilibrium with the radiation. An additional question is whether the dust sublimation front shifts in response to the varying irradiation by the primary due to its orbital motion. To answer this question we conduct simulations of the growth and sublimation of dust grains in the conditions of thermal cycling due to the orbital motion of the primary, which show that the dust sublimation front is stable and does not shift within one orbital period. These results allow us to proceed with modeling the disk in a steady state setting in regard to its temperature distribution, and with the inner rim of the disk having a fixed position determined by the dust sublimation temperature.

The radiative transfer modeling is done using lambda-operator approach. Lambda-operator is a functional that connects the source function distribution with the mean intensity at a point. We discretize the lambda-operator on a cylindrical grid, so that the radiative transfer problem translates into a system of linear equations, which we solve directly. The disk density structure is represented by a double-power law along the radial coordinate, and a Gaussian function along the vertical coordinate. In addition to the axially symmetric disk structure, we introduce non-symmetric density enhancements in the form of spiral density waves. The temperature distribution inside the disk is found via an iterative procedure, which uses the discrete lambda-operator to take into account self-irradiation of the disk. Synthetic images of the disk are computed based on the obtained source function distribution, which is used to integrate the radiative transfer equation along the line of sight.

Results of our radiative transfer simulations show that the asymmetric irradiation by the primary is indeed capable of producing the asymmetry of brightness, comparable to that found from interferometry, although with a single maximum of brightness. This asymmetry is produced by the thermal emission of dust, as a result of an asymmetric temperature distribution along the inner rim of the disk. Addition of spiral density enhancements to the disk allows reproducing a secondary maximum, for certain combinations of the primary orbital position and orientation of the disk. We conclude that the observed brightness distribution of the disk around V390 Vel can be explained by the asymmetric irradiation in combination with the presence of spiral density waves in the disk.

# Contents

<b>Summary for a general audience</b>	<b>i</b>
<b>Scientific summary</b>	<b>ii</b>
<b>1 Introduction</b>	<b>2</b>
1.1 Single star evolution beyond main sequence . . . . .	2
1.1.1 Evolution on the asymptotic giant branch . . . . .	4
1.1.2 Post-AGB evolution . . . . .	6
1.1.3 Observed post-AGB samples . . . . .	6
1.2 Binary evolution . . . . .	8
1.2.1 Common envelope . . . . .	12
1.2.2 Orbital evolution and period-eccentricity puzzle . . . . .	13
1.2.3 Formation of disks around binary post-AGB systems . . . . .	16
1.2.4 Physics and structure of circumbinary disks . . . . .	17
1.3 The aim of this thesis . . . . .	20
<b>2 Observational properties of post-AGB binaries</b>	<b>23</b>
2.1 General properties of post-AGB binaries . . . . .	23
2.1.1 Spectral energy distribution . . . . .	23
2.1.2 Keplerian velocity field traced by CO . . . . .	25
2.1.3 Infrared dust properties . . . . .	25
2.1.4 Depletion of refractory elements . . . . .	26
2.1.5 Jets . . . . .	27
2.2 Properties of V390 Vel . . . . .	27
2.2.1 Spectral energy distribution . . . . .	27
2.2.2 Radial velocity . . . . .	27
2.2.3 CO lines . . . . .	28
2.2.4 Interferometry and disk structure . . . . .	31
<b>3 Binary evolution history of V390 Vel</b>	<b>33</b>
3.1 Estimating binary masses and separation . . . . .	33

3.2	Binary evolution code binary_c . . . . .	36
3.3	Binary evolution modeling . . . . .	39
3.4	Conclusions . . . . .	41
<b>4</b>	<b>Micro-scale physical processes in the disk: dust sublimation and interaction with gas</b>	<b>45</b>
4.1	Asymmetric irradiation of the disk by the primary . . . . .	45
4.2	Thermal interaction between dust, gas and radiation . . . . .	47
4.2.1	Dust-radiation equilibrium . . . . .	48
4.2.2	Collisional heat transfer between dust and gas . . . . .	48
4.2.3	Radiation-dust-gas equilibrium . . . . .	50
4.3	Disk cooling timescale . . . . .	51
4.4	Stability of the sublimation front . . . . .	52
4.5	Conclusions . . . . .	56
<b>5</b>	<b>Modeling the radiative transfer in the disk</b>	<b>60</b>
5.1	Disk structure . . . . .	60
5.1.1	Vertical structure . . . . .	61
5.1.2	Radial structure . . . . .	63
5.1.3	Spiral density waves . . . . .	64
5.2	Position of the primary . . . . .	65
5.3	Radiative transfer . . . . .	65
5.3.1	Formulation of the lambda-operator . . . . .	65
5.3.2	Computation grid and the interpolation of the source function	67
5.3.3	Construction of the lambda-matrix . . . . .	68
5.3.4	Temperature structure . . . . .	70
5.3.5	Synthetic images . . . . .	70
5.4	Results . . . . .	72
5.4.1	Symmetric disk structure . . . . .	73
5.4.2	Disk with spiral density waves . . . . .	73
5.5	Discussion . . . . .	74
<b>6</b>	<b>Conclusions and future research</b>	<b>79</b>
6.1	Conclusions . . . . .	79
6.2	Future research . . . . .	80
<b>Bibliography</b>		<b>81</b>

Table 1: Symbols used in the text

Symbol	Units, cgs	Units, SI	Description
$a$	[cm]	[m]	Dust grain radius
$\rho$	[g/cm <sup>3</sup> ]	[kg/m <sup>3</sup> ]	Bulk density of a dust grain
$\rho_X$	[g/cm <sup>3</sup> ]	[kg/m <sup>3</sup> ]	Density of refractory elements in gas phase
$\rho_d$	[g/cm <sup>3</sup> ]	[kg/m <sup>3</sup> ]	Density of refractory elements in solid phase
$\bar{\rho}_X$	[g/cm <sup>3</sup> ]	[kg/m <sup>3</sup> ]	Total density of refractory elements
$\rho_{gas}$	[g/cm <sup>3</sup> ]	[kg/m <sup>3</sup> ]	Gas density
$T_d$	[K]	[K]	Dust temperature
$m_d$	[g]	[kg]	Mass of a dust grain
$\Sigma$	[g/cm <sup>2</sup> ]	[kg/m <sup>2</sup> ]	Surface density of a disc
$H_\rho$	[cm]	[m]	Density scale height of a disc
$\Omega$	[rad/s]	[rad/s]	Angular velocity
$n_d$	[1/cm <sup>3</sup> ]	[1/m <sup>3</sup> ]	Dust number density
$n_X$	[1/cm <sup>3</sup> ]	[1/m <sup>3</sup> ]	Number density of refractory elements
$r$	[cm]	[m]	Radial coordinate
$z$	[cm]	[m]	Vertical coordinate (orthogonal to the disc plane)
$P$	[s]	[s]	Orbital period
$G$	[cm <sup>3</sup> /g/s <sup>2</sup> ]	[m <sup>3</sup> /kg/s <sup>2</sup> ]	Gravitation constant
$k$	[erg/K]	[J/K]	Boltzmann constant
$T_*$	[K]	[K]	Stellar temperature
$L_*$	[erg/s]	[J/s]	Stellar luminosity
$M_*$	[g]	[kg]	Stellar mass
$R_*$	[cm]	[m]	Stellar radius
$F$	[erg/s/cm <sup>2</sup> ]	[J/s/m <sup>2</sup> ]	Flux
$B_\lambda(T)$	[erg/s/cm <sup>2</sup> /nm/sr]	[J/s/m <sup>2</sup> /nm/sr]	Planck function
$J_\lambda$	[erg/s/cm <sup>2</sup> /nm]	[J/s/m <sup>2</sup> /nm]	Mean specific intensity
$J_\nu^*$	[erg/s/cm <sup>2</sup> /Hz]	[J/s/m <sup>2</sup> /Hz]	Mean intensity from the primary
$\chi_\lambda$	[1/cm]	[1/m]	Wavelength-dependent linear absorption
$\kappa_\lambda$	[cm <sup>2</sup> /g]	[m <sup>2</sup> /kg]	Mass absorption coefficient
$\Lambda_\nu$			Lambda-matrix

# Chapter 1

## Introduction

Unlike more massive stars, which explode as supernovae at the end of their lives, lower-mass stars end up as stellar remnants known as white dwarfs that consist mostly of carbon and oxygen. Between the start of hydrogen burning, which signifies the start of main sequence, and the final white dwarf stage, the star goes through a number of evolutionary stages, during which its structure and chemical composition changes drastically. At a certain point in their evolution, low-mass stars loose most of their mass due to strong stellar winds, and end up with a final mass between  $0.4\ldots 0.8 M_{\odot}$ . The ejected matter, enriched with heavy elements at previous evolutionary stages, condenses into dust as soon as it becomes cold enough for the condensation to occur. Further fate of this dust depends on whether the star is a single or a binary. In case of a single star, the dust forms an expanding shell, gravitationally unbound from the star. If the star has a companion, i.e. if it is a part of a binary system, part of this dust usually forms a stable circumbinary disk. The close connection between the presence of such a disk and binarity of the system is now well established from observations. Presence of a disk around a binary system introduces an additional level of complexity into the evolution of such a system. The interaction between the binary and the disk, which is poorly understood at the moment, may lead to various phenomena such as eccentricity pumping of the binary orbit or gravitational instabilities in the disk. This is why this thesis focuses on the disk structure. In this chapter we discuss different stages in the evolution of single low-mass stars, and introduce basic concepts of binary evolution.

### 1.1 Single star evolution beyond main sequence

*This section, excluding subsections, is based on Kippenhahn et al (2012).*

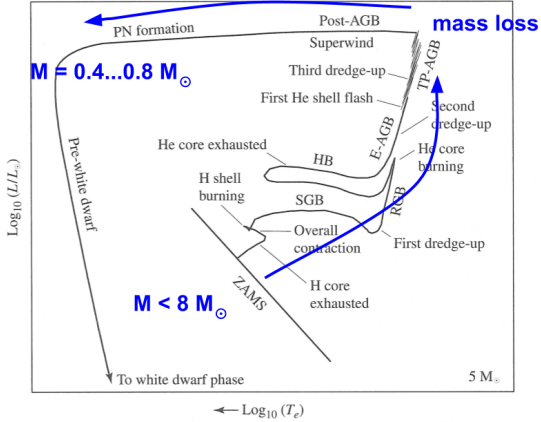


Figure 1.1: Hertzsprung-Russell diagram, showing evolution of a 5 solar mass star.

At the end of the main sequence, when most of the hydrogen in the core of a star has been converted into helium, the nuclear burning shifts to the shell surrounding the core, where the hydrogen concentration is still high. At this point, the temperature of the He core is not high enough to initiate triple-alpha reaction. Depending on the initial mass of the star, the mass of the He core can be below or above the Schönberg-Chandrasekhar (SC) mass, which is the maximum mass of a He core that can still support the outer layers (and its own mass). Stars with an initial mass below  $3M_{\odot}$  have He core masses below SC limit; the core becomes degenerate and maintains hydrostatic equilibrium while hydrogen burning continues in a shell, thus slowly increasing He core mass. When the He core mass reaches the SC limit, the core starts contracting quickly, heating in the process as the gravitational energy transforms into the thermal energy. At the very center of the core the temperature becomes high enough for the plasmon neutrino cooling process ( $\gamma \rightarrow \nu\bar{\nu}$ ) to take place. Due to this, the initiation of the helium burning occurs off-center, whenever the temperature becomes high enough for triple-alpha reaction to proceed. Stars with an initial mass above  $3M_{\odot}$  reach He core masses above the SC limit without experiencing electron degeneracy, and initiate triple-alpha reaction in the centre.

After the initiation of the He burning, the star arrives on the horizontal branch in the HR diagram (HB in Figure 1.1). At this stage the star has a non-degenerate He core, surrounded by a hydrogen-rich envelope. The luminosity is sustained by the central He burning and a shell hydrogen burning. As the central He burning continues, the star moves along the horizontal branch where it crosses the instability strip and experiences large-amplitude radial oscillations. Cepheids and RR Lyra are examples of stars at this stage of evolution. Both temperature and luminosity of the stars on horizontal branch depends positively on the metallicity, which was shown by comparing evolution of different clusters of stars.

### 1.1.1 Evolution on the asymptotic giant branch

*This section is mainly based on Lattanzio & Wood (2004).*

As the He core burning proceeds, an inner carbon-oxygen (C/O) core starts to develop. At the end of the evolution on the horizontal branch, the remaining He is located in a shell between the C/O core and the hydrogen envelope. However, burning of He in a shell proceeds quite differently from the hydrogen shell burning. The energy production rate for the triple-alpha reaction is  $\epsilon \propto T^\nu$  with  $\nu \approx 30\ldots40$ , whereas for pp-chain  $\nu \approx 4$ . In addition, the electron degeneracy inside the He shell makes pressure independent of temperature, leading to the situation when adding energy into the shell leads to the heating, rather than expansion and cooling of the shell. Therefore, there is a positive feedback between temperature and energy production, which results in a series of runaway reactions when the luminosity of the He layer reaches  $10^8 L_\odot$ . This energy is absorbed by the outer layers, which expand and cool. This instability was first discovered by Schwarzschild and Härm (1965), who showed that the condition for it to occur is

$$\frac{\Delta T}{T} > \frac{4}{\nu}$$

where  $T$  and  $\Delta T$  are the average temperature and the temperature gradient across the shell. These thermal runaways, also known as thermal pulses, occur every  $10^4$  to  $10^5$  years, depending on the mass of the star (the more massive the star is, the more frequent the pulses are), and the total number of pulses ranges from 5 for solar-mass stars, to  $\sim 30$  for a  $5M_\odot$  star (Vassiliadis & Wood, 1993). The consequence of the thermal pulsing is that the excess energy, released inside the He intershell below the hydrogen-rich envelope, triggers convection in the intershell, because radiative transport is not efficient enough in transporting this energy to the envelope above it. After a shell flash (thermal pulse), during the relaxation and before the hydrogen shell burning is initiated, the convective envelope can penetrate the intershell and bring nucleosynthetic products to the surface. This process is known as third dredge-up and play an important role in the chemical evolution of the star, as it helps transport to the surface heavy elements synthesized at the site of the s-process.

As the luminosity of the star continues to increase, it enters the region of intrinsic Mira instability. Mira-type variability have amplitude larger than 2.5 magnitudes in the visual part of the spectrum, although the bolometric amplitude is usually smaller ( $\sim 1$  mag), because most of the energy emitted by AGB variables comes out in the infrared (Whitelock et al, 2000). The period of pulsations ranges from  $\sim 100$  days to  $\sim 1000$  days and shows a positive correlation with luminosity (linear in  $L - \log P$  space). The mechanism of Mira pulsations

is still not completely understood. The first explanation was suggested by Eddington (1941), who showed that the existence of period-luminosity relation is connected to the partial ionization layer of hydrogen, which drives the instability. This explanation was widely accepted; the variability was thought to be caused by radial oscillations due to the shock waves originating below the atmosphere and expanding outwards. Although consistent with the shape of Mira light curves, the radial (centrally symmetric) character of pulsations is difficult to reconcile with the presence of convective envelope and large convective cells at the surface of AGB stars. The existence of such convective cells was predicted by Schwarzschild (1975) based on theoretical arguments, later reproduced in 3D radiative hydrodynamics simulations (Freytag & Höfner, 2008), and recently confirmed with interferometry observations of R Sculptoris (Wittkowski et al, 2017).

Regardless of the exact nature of the pulsation mechanism, it is clear that pulsations play an important role in the mass loss of AGB stars. With typical stellar radii of several hundred solar radii, the surface gravity of AGB stars is 4...5 orders of magnitude below that of the Sun, according to the relation

$$g = \frac{GM_\star}{R_\star^2} \quad (1.1)$$

As an example, for a  $1 M_\odot$  and  $100 R_\odot$  star the surface gravity is only  $\sim 3 \text{ cm/s}^2$ . The surface layers of an AGB star are therefore loosely bound and easily ejected by shock waves, triggered by pulsations. An additional factor facilitating the outflow is the radiation pressure, which is quite significant for AGB stars with typical luminosities of  $10^3 \dots 10^4 L_\odot$ . The radiation pressure however cannot act directly on the gas due to insufficient absorption. Instead, the momentum is transferred to the gas from the dust grains that form in the cool layers of the atmosphere (at  $\sim 2 \dots 3 R_\star$  from the surface) and efficiently absorb stellar radiation even at infrared wavelengths. The radiation pressure and pulsation-induced shock waves act together in driving the mass loss: the shock waves lift the outer layer of the atmosphere to a radius where it is cool enough for dust grains to form, and after the dust has condensed, the radiation pressure accelerates the grains, which push the gas along. At a certain radius the outflow velocity exceeds the local escape velocity and the material is ejected into the interstellar medium.

The rate of mass loss is most reliably determined based on CO rotational line emission at mm and sub-mm wavelengths. Observations of CO emission show that the mass loss rate ranges from  $10^{-7}$  to  $10^{-5} M_\odot/\text{year}$  and correlates with terminal wind velocity as  $\dot{M} \propto v_\infty^{2.7}$ . The typical range of the terminal wind velocities around AGB stars is 5...20 km/s (Danilovich et al, 2015). The mass loss rate is highly variable in time and may exhibit short (a few hundred years) bursts when the rate may increase by two orders of magnitude, which is evident from concentric shells of gas traced by CO emission around some AGB stars. For example, an almost

perfectly spherical shell is observed around an AGB star TT Cyg, formed by the matter that was ejected  $\sim$ 7000 years ago (Olofsson et al, 1998). The period of intensive mass loss signifies the end of the AGB phase. The star has lost most of its hydrogen-rich envelope and its mass is now close to that of a white dwarf, which is  $\sim 0.6 M_{\odot}$ .

### 1.1.2 Post-AGB evolution

The asymptotic giant branch phase of evolution is considered to be finished when the star has lost most of its hydrogen envelope. From this point on, the star is evolving on the post-AGB track. The exact moment when the post-AGB phase starts is a matter of definition, which is based on the mass of the remaining hydrogen envelope. We adopt a limit of  $0.01 M_{\odot}$ , so that stars with the mass of the remaining envelope below this limit are considered to be post-AGB stars. The mass of the remaining envelope can be inferred from the effective temperature using evolutionary models (Frankowski, 2003). At the start of the post-AGB track, the effective temperature of the star is in the range of 3000...4000 K, which is not high enough to produce UV photons that could ionize hydrogen in the vicinity of the star. The subsequent evolution proceeds with approximately constant luminosity and with the temperature gradually increasing because the core of the star becomes visible through the diminishing hydrogen envelope. In the HR diagram, this corresponds to the horizontal shift to the left. When the temperature of the star reaches approximately  $10^4$  K, the radiation from the star starts to ionize the surrounding hydrogen and the system enters the Planetary Nebula (PNe) phase.<sup>1</sup> PNe are expanding shells of ionized gas, visible in the hydrogen emission lines, produced by the recombination of electrons with ions in the plasma. After reaching a maximum temperature of  $10^5$ ... $10^{5.5}$  K, depending on the initial mass, the star transitions to the white dwarf cooling track, where its luminosity decreases by at least three orders of magnitude (Vassiliadis & Wood, 1993). The end results of post-AGB evolution is a stellar remnant, consisting mostly of a mixture of carbon and oxygen.

### 1.1.3 Observed post-AGB samples

Post-AGB stars are identified by their high luminosity with a typical range from  $3000 L_{\odot}$  to  $20000 L_{\odot}$  (Kamath et al, 2014), and effective temperature from  $\sim$

---

<sup>1</sup>The term “Planetary Nebula” was coined in the 18th century by William Herschel, who was uncertain whether PNe were members of the Solar System, or more distant objects. Today we know that PNe are unrelated to planets. For the details on the origin of the name, see Hoskin, M. (2014). William Herschel and The Planetary Nebulae. *Journal for the History of Astronomy*, 45(2), 209–225.

4000 K to  $\sim$  10000 K. Stars with effective temperatures higher than this range are able to ionize the surrounding hydrogen that was ejected during the mass loss and are classified as “Planetary Nebulae”. A catalogue of galactic post-AGB stars was compiled by Szczerba et al (2007), which includes 326 objects “very likely” to be post-AGB stars and 107 “possible” post-AGB stars. The catalogue includes the following types of post-AGB objects (not mutually exclusive):

1. **Sources selected based on IRAS color.** This is the largest class in the catalog that contains 115 sources. A star is assigned to this class if it is located within a region in the IRAS color-color diagram bounded by  $F_{12}/F_{25} \leq 0.50$  and  $F_{25}/F_{60} \geq 0.35$  where  $F_\lambda$  is the flux at the wavelength  $\lambda$  in  $\mu\text{m}$ . The same region in the IRAS color-color diagram is also occupied by planetary nebulae, young stellar objects (YSO), galaxies and infrared objects without optical counterparts. The discrimination between classes was done using additional data from optical spectroscopy, near-IR photometry and by searching for optical counterparts. To separate YSOs from post-AGB stars; location of the object relative to known star-forming regions was taken into account (Suárez et al, 2006).
2. **RV Tauri stars.** These are highly luminous variable stars that show alternating deep and shallow minima in their light curves with periods between 30 and 150 days. A subclass labelled RVb shows, in addition to the short-period variation, a long-period dimming with periods of the order of  $10^3$  days. All RVb stars are binaries, and the long-period variation is interpreted as due to the obscuration of the primary star by the circumbinary disk.
3. **High Galactic latitude supergiants.** This class consists of mimics of massive supergiants, but their location at high Galactic latitude is indicative of a low-mass nature. They are now generally acknowledged to be low-mass stars of high luminosity due to their highly evolved nature. Their distances are generally unknown, even in the GAIA era.
4. **Bright stars with infrared excess.** The excess of radiation in the infrared indicates the presence of dust, which is produced at the AGB stage in large amounts. The shape of the spectral energy distribution (SED) of post-AGB objects, in particular the wavelength at which the IR excess starts, indicates that the highest temperature of the dust in these systems is very close to the sublimation temperature of the dust material. Taking into account the luminosity, the sublimation edge must be located within 10 AU from the central source. It can therefore be inferred that at least part of the dust must be gravitationally bound, i.e. located in a Keplerian disk, because with the typical AGB outflow velocity, a dust shell would expand to much

cooler regions in the system within years. The ratio of the IR lluminosity to the bolometric luminosity  $L_{IR}/L_\star$  for post-AGB objects is within a range of 0...0.5. From this it can be inferred that the scale hight of these disks is rather large - for  $L_{IR}/L_\star = 0.4$  the opening angle of the disk as seen from the star must be  $\approx 45^\circ$  (De Ruyter et al, 2006).

5. **R Coronae Borealis stars.** R CrB stars are H-deficient and C-rich supergiants that undergo irregular declines of up to 8 mag on a timescale of weeks. The return to normal brightness is slower and lasts up to several months (Clayton, 1996). This brightness variation was explained as due to dust clouds forming in the vicinity of the star and gradually dissipating, driven away by radiation pressure (O'Keefe, 1939). This explanation was confirmed when dust clumps were first directly observed around an R CrB star RY Sgr (de Laverny & D.Mekarnia, 2004). The origin and evolutionary stage of R CrB objects is uncertain: they are thought to be either products of white dwarf mergers, or post-AGB stars experiencing final thermal pulse.
6. **21 micron emission sources.** The common features of these sources is the presence of an emission band around 21 micron, large infrared excess and overabundance of s-process elements (Van Winckel & Reyniers, 2000). The presence of s-process elements indicates that these are post-third dredge up objects. The source of the 21 micron feature is not definitely identified; one possible candidate is TiC (von Helden et al, 2000). This feature was also detected in planetary nebulae (Hony et al, 2001), which shows that the source of the emission is a stable dust component capable of surviving UV radiation.

## 1.2 Binary evolution

Approximately one third of solar-type systems is binary (Raghavan et al, 2010). This fraction is even higher for massive stars ( $\sim 50\%$ ; Sana et al, 2009), however, massive stars follow a different evolutionary path that does not pass through AGB stage since they explode as supernovae before reaching this stage. The stellar evolution described in §1.1 assumes a single star without any companions. How does this picture of evolution changes in the presence of a companion star?

The gravitational potential around a single star of mass  $M$  has the following form:

$$\Phi_{single}(x, y, z) = -\frac{GM}{\sqrt{x^2 + y^2 + z^2}} \quad (1.2)$$

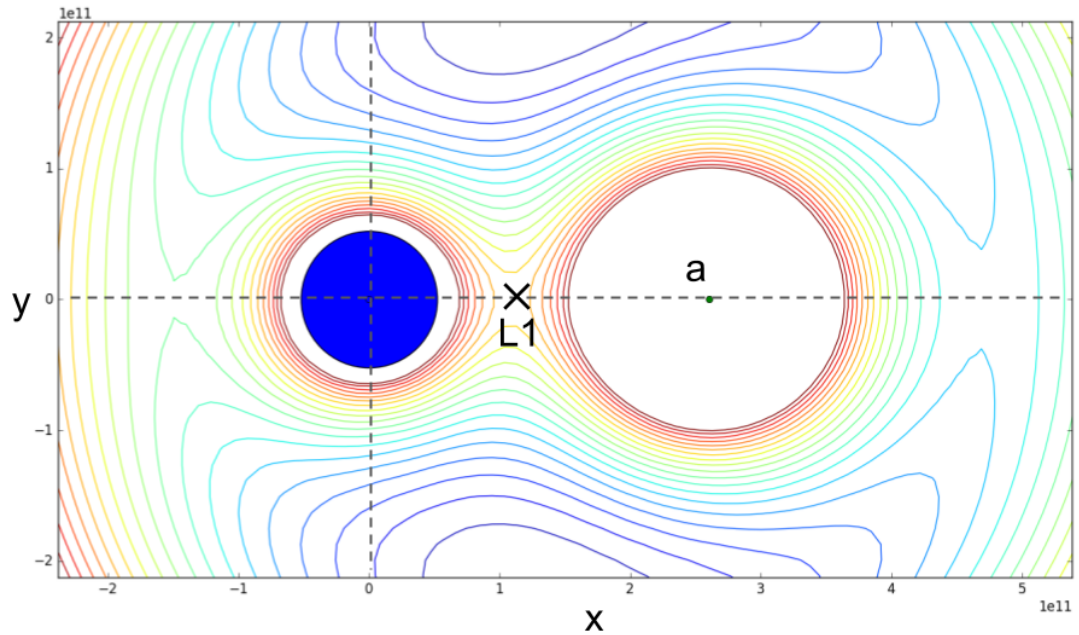


Figure 1.2: Isolines of potential energy in the Roche potential in the cross-section orthogonal to the orbital angular momentum vector. The potential is rendered in scale with a star of a radius  $75 R_{\odot}$  (filled blue circle), typical for AGB stars. L1 marks the first Lagrangian point.

In a binary system, in addition to the presence of a second star (companion), we also have to take into account the rotation of the entire system. Let us place the origin of the coordinate system at the center of the star with mass  $M_1$ , and define the separation between the stars  $a$ , so that the coordinates of the companion are  $(a, 0, 0)$ . If the orbital angular velocity of the system is  $\Omega$  [rad/s] ( $\Omega = 2\pi/P$ , with  $P$  being the period), then the gravitational potential around the binary system, in the co-rotating frame of reference is given by:

$$\Phi(x, y, z) = -\frac{GM_1}{\sqrt{x^2 + y^2 + z^2}} - \frac{GM_2}{\sqrt{(x - a)^2 + y^2 + z^2}} - \frac{1}{2}\Omega^2 [(x - \mu a)^2 + y^2] \quad (1.3)$$

where  $\mu = \frac{M_2}{M_1 + M_2}$ . The last term on the right-hand side is due to the Coriolis force, arising because we consider the potential in the co-rotating frame of reference. Equipotential surfaces of the Roche potential are shown in Figure 1.2, at a cross-section orthogonal to the rotation axis. The equipotential surface that goes through the Lagrangian point L1 contains two volumes called *Roche lobes* (Figure 1.3). A Roche lobe defines a volume, inside which a particle corotating with the system is gravitationally bound. As soon as a particle goes outside of the Roche lobe it becomes unbound and can escape to infinity. Matter can also flow through the L1 point from one Roche lobe to the other, for example in the case when the primary star expands and fills its Roche lobe. The matter flowing into the Roche lobe of the companion in this case will be accreted by the companion, thus resulting in a mass transfer between the two stars. This process is called *Roche lobe overflow (RLOF)*; it makes a significant impact on the evolution of both stars in the system. The timescale, on which the mass transfer occurs, depends on the response of the donor (the star that loses mass) to the mass loss, and can be governed by dynamic, thermal, or nuclear timescales. If the donor contracts in response to the mass loss, the mass transfer is stable and proceeds as fast as the donor's intrinsic expansion. However, if the donor expands in response to the mass loss, the transfer becomes unstable and may lead to the loss of the entire envelope.

In order to characterise the size of the Roche lobe relative to the radius of the star, a term *Roche lobe radius* was introduced. Since Roche lobe is not a sphere, the term Roche lobe radius means a radius of a sphere that has the same volume as the Roche lobe. A useful approximation to the radii of Roche lobes was suggested by Eggleton (1983). If the orbital separation of the binary is taken as a unit of length, then the radius of the Roche lobe  $r_L$  is approximately given by:

$$r_L = \frac{0.49q^{2/3}}{0.6q^{2/3} + \ln(1 + q^{1/3})} \quad (1.4)$$

where  $q = M_2/M_1$  is the mass ratio of the binary.

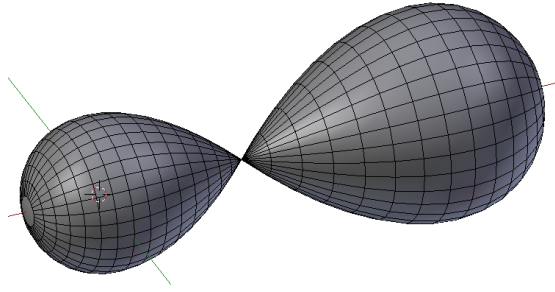


Figure 1.3: Three-dimensional surface, forming Roche lobes in the Roche potential around a binary system.

In a binary system, when the masses of the two stars are not exactly equal, one of the stars will evolve faster. The time that it takes for a main-sequence star to burn down the hydrogen in the core is given by the nuclear timescale:

$$\tau_{nuc} \propto \frac{M_\star}{L_\star} \propto \frac{M_\star}{M_\star^{3.35}} = \frac{1}{M_\star^{2.25}} \quad (1.5)$$

where we used the mass-luminosity relation  $L \sim M^{3.35}$  for stars with  $M \in [1, 10] M_\odot$ . This relation shows that more massive stars evolve faster than less massive ones. For example, even if the mass difference between the two stars is only 1%, the nuclear timescale of the more massive star is  $\sim 2\%$  shorter. For a solar-mass star, the nuclear timescale is  $\approx 7$  bln years; this means that the more massive star in this example will finish its main-sequence evolution 150 mln years earlier. So by the time when the more massive star reaches AGB stage, its companion is still on the main sequence. On the AGB, the stellar radius increases by two orders of magnitude and the expanding envelope fills the gravitational potential whatever configuration it has. For a single star, the potential is approximately spherically symmetric; the star has a condensed core whose density is much higher than that of the envelope. In a binary system, the spherically symmetric potential of the primary<sup>2</sup> star is altered by the presence of a companion, as a result of which the envelope of the expanding star may overflow into the Roche lobe of the companion. The resulting mass transfer creates a bifurcation point where the evolution of single and binary systems diverges, and adds a new level of complexity to the problem of stellar evolution.

---

<sup>2</sup>In binary systems, the *initially* more massive and more luminous star is usually called primary and the less massive - secondary or companion. The mass ratio may reverse, but the primary still remains more luminous, at least in case of post-AGB stars.

### 1.2.1 Common envelope

The common envelope stage is triggered by an unstable dynamic mass transfer, when the Roche lobe radius shrinks faster than the radius of the star in response to the mass loss. In this case, the Roche lobe of the primary is completely filled and the matter is flowing into the Roche lobe of the companion through the L1 point. However, the companion can only accrete matter with a limited speed, which is usually not enough to accrete all the inflowing matter. As a result, the matter fills the Roche lobe of the companion as well and forms an envelope around both stars. Due to the frictional drag between the binary and the envelope, the orbit of the immersed binary shrinks, which is known as spiral-in phase. The spiral-in phase lasts at most a few 100 years and produces a short-orbit binary or may result in a merger (Podsiadlowski, 2001). More specifically, if the primary is a red supergiant with a convective envelope, then there are three main outcomes of the common envelope phase, which depend on the mass of the companion (Podsiadlowski, 2008):

- For low-mass companions, the orbital energy released during spiral-in is much less than the gravitational binding energy of the common envelope, the envelope does not expand and the spiral-in occur on the dynamical timescale, leading to a fast (dynamic) merger.
- For intermediate-mass companions, the orbital energy is enough to unbind and eject the common envelope, provided that the energy transfer between the orbit and the envelope is faster than the hydrostatic timescale of the envelope. The system ends as a short-orbit binary.
- For higher-mass companions, the initial expansion of the envelope is very rapid, but the overall expansion is self-regulating; the spiral-in is slow and most likely leads to a slow merger of the system.

A simple formalism adopted to describe the envelope ejection process is:

$$E_{env} = \alpha \Delta E_{orb} \quad (1.6)$$

where  $E_{env}$  is the final gravitational (binding) energy of the envelope,  $\Delta E_{orb}$  is the change in orbital energy of the binary; and  $0 < \alpha < 1$  is a parameter that describes the efficiency of ejecting the envelope, i.e. converting the orbital energy into the kinetic energy of the envelope (Tauris & van den Heuvel, 2006). The efficiency of ejection depends on the fraction of orbital energy that is lost to increase the internal thermal energy of the envelope. The envelope is ejected if  $\alpha$  is below some critical value. In the ideal case of zero loss to the thermal energy this critical value is 1, but for more realistic scenarios it was shown using hydrodynamical simulations that the actual value is  $\sim 0.3$  (Livio & Soker, 1988). Furthermore,  $\alpha$  has been

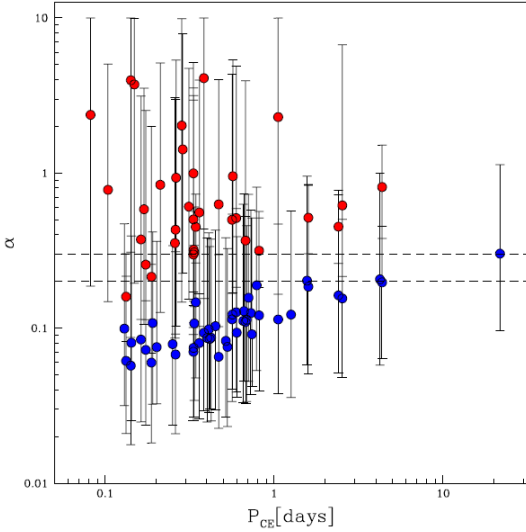


Figure 1.4: Common envelope ejection efficiency from (Zorotovic et al, 2010) as a function of the post-common envelope orbital period. Blue points are for AGB progenitors, while red points are for progenitors from an earlier evolutionary stage (referred to as “first giant branch” by the authors).

constrained from observations (Zorotovic et al, 2010) and was found to be  $\sim 0.1$  for AGB progenitors and correlating with the orbital period (Figure 1.4). However, in the simulations of disk formation after the common envelope, (Izzard & Jermyn, 2018) had to set the efficiency parameter to  $\alpha = 1$  to match the observed periods of post-AGB systems with disks (100-1000 days). Achieving the match with  $\alpha < 1$  was possible by adjusting other parameters.<sup>3</sup>

### 1.2.2 Orbital evolution and period-eccentricity puzzle

The orbital parameters of importance for the binary evolution are those that define the size and shape of the orbit: semi-major axis, period and eccentricity. The semi-major axis and period are connected to the total mass of the system via the Kepler’s third law so that any two of these parameters determine the third one. The initial distribution of semi-major axes of solar-type binary systems covers a wide range of values from  $10^{-2}$  to  $10^4$  AU (Raghavan et al, 2010). Depending on the initial value of the semi-major axis, the mass transfer is initiated at different evolution stages of the primary, or does not happen at all if the separation is too large for the envelope of the primary to overfill its Roche lobe. Another

---

<sup>3</sup>The authors (Izzard & Jermyn, 2018) remark: “We do not pretend to better understand common envelope evolution with our simple model.”

extreme is the common envelope evolution when the expanding envelope of the primary engulfs both stars. Eccentricity affects the evolution because it determines the periastron distance, i.e. the shortest separation between the stars in the orbit. For two systems with the same semi-major axis but different eccentricities, the higher-eccentricity system can initiate the mass transfer earlier, because the shortest separation is smaller, thus the mass transfer can happen close to or at the periastron. The initial eccentricity of binary systems covers a full range from 0 to almost<sup>4</sup> 1; in addition, eccentricity is correlated with orbital period – the short-period systems tend to have eccentricity closer to zero. The reason for this correlation is that the orbits of short-period systems are circularized by the tidal dissipation of energy and the transfer of rotational to orbital angular momentum (Zahn, 1977).

Depending on the initial orbital separation, two theoretical evolutionary scenarios can be distinguished. (a) If the separation is less than  $\sim 2$  AU, the primary will initiate unstable mass transfer while on AGB, producing a common envelope. Hydrodynamical simulations of this scenario (Yorke et al, 1995) show that the entire common envelope is ejected as a result of the transfer of the orbital angular momentum to the angular momentum of the envelope. The ejected mass can remain partly confined to the orbital plane and forms a thick disk around the system. The orbit of the binary shrinks substantially and may result in merger depending on the initial mass of the primary and the mass of its remnant core after the envelope ejection; the merger happens if the ratio of the remnant mass to the initial mass is too low. (b) If the initial separation is wider than  $\sim 2$  AU, the common envelope phase is avoided. Instead, the interaction happens when the primary experiences the strong wind phase at the end of the AGB. Conventional understanding of this type of interaction is that the companion accretes a fraction of the material from the primary via the Bondi-Hoyle-Lyttleton (Hoyle & Lyttleton, 1939; Bondi & Hoyle, 1944) accretion model. The rest of the material escapes and removes the angular momentum from the system, leading to the widening of the orbit. The distribution of orbital periods of post-AGB binaries is therefore expected to have a bimodal shape, with two distinct populations produced by either common envelope interaction or wind overflow. This theoretical model, however is in contradiction with observational data, which show that the orbital period distribution is unimodal and in fact located in the gap between the two theoretical populations.

The origin of this discrepancy is thought to be twofold, according to Van Winckel (2018). Firstly, the theoretical models are subject to many uncertainties: efficiency of the common envelope ejection, physical description of the common envelope phase, mass transfer efficiency, impact of radiation pressure on the shape

---

<sup>4</sup>The eccentricity of a binary system cannot be *exactly* 1 in principle.

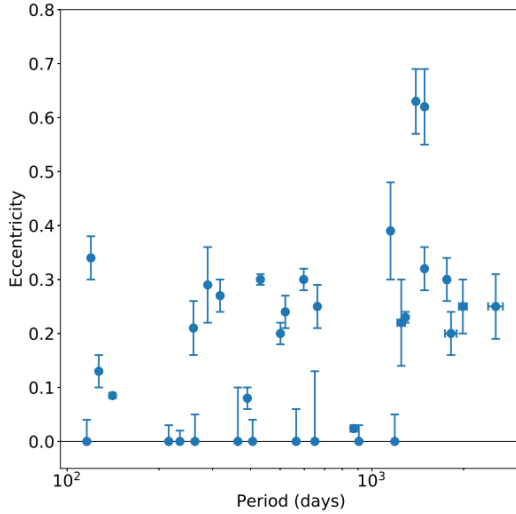


Figure 1.5: Period-eccentricity diagram for binary post-AGB systems. From Oomen et al (2018).

of the Roche potential. Secondly, the many parameters involved in predicting the outcome of the binary evolution are not well constrained due to the lack of observational data. Nevertheless, thanks to detailed hydrodynamical simulations, some progress has been made towards more complete understanding of binary interactions. In particular, Saladino et al (2018) showed that the wind accretion by the companion depends strongly on the ratio of the terminal wind velocity to the orbital velocity. When this ratio is high (fast wind), the accretion is well described by the Bondi-Hoyle-Lyttleton (BHL) approximation and the orbit of the binary tends to widen. However, for a slow wind, which is typical for AGB stars, the accretion efficiency is greatly enhanced compared to the BHL prediction due to the formation of an accretion disk around the companion, in which case the orbit will tend to shrink.

The period-eccentricity diagram for binary post-AGB systems (Figure 1.5) illustrates the contradiction of observations with theoretical models. There is an obvious lack of systems with orbital periods shorter than 100 days, which is unexpected considering that models of common envelope evolution predict inspiral that produces such short-period systems. This cannot be explained by observational bias, because short-period systems are the easiest to detect with radial velocity monitoring.

Another inexplicable feature of this diagram is the occurrence of both eccentric and zero-eccentricity systems. There are two possible scenarios of how this distribution of eccentricities could arise. (a) Since the initial distribution of eccentricities is homogeneous between 0 and 1 and does not show a distinct population of zero-

eccentricity systems, one could imagine some selective circularization mechanism that acted during the binary interaction depending on some unknown parameter. The orbital separation can be readily excluded as such a parameter because zero-eccentricity post-AGB systems are found with both small and large orbital separations. (b) The initially eccentric post-AGB systems could all be circularized at some point during their evolution, and then became eccentric again due to the action of some eccentricity-pumping mechanism. One such mechanism is the interaction with the circumbinary disk, which results in the angular momentum transfer from the binary to the disk (Dermine et al, 2013). This model predicts that over the typical disk lifetime of 25 thousand years the eccentricity increases from 0 to  $\sim 0.4$ , which is enough to explain the observed orbits of post-AGB binaries apart from two systems with orbital periods longer than 1000 days and  $\sim 0.6$  eccentricity. These two systems could have started the post-AGB phase in a circular orbit, because systems with such long periods are not efficiently circularized during the AGB phase. Alternatively, the disk lifetime could be underestimated, thus leaving more time for the eccentricity pumping mechanism to act. However, a more important discrepancy is that the model predicts smaller final eccentricities for longer-period systems, whereas the data show the opposite trend. A possible explanation of this discrepancy, suggested by the authors (Dermine et al, 2013), is that the properties of the disk and the binary are correlated in such a way that eccentricity-pumping is more efficient in longer-period systems. However, current understanding of the disk formation around post-AGB binaries is insufficient to provide any arguments in support of this hypothesis.

### 1.2.3 Formation of disks around binary post-AGB systems

If the initial orbit of the binary is wide enough, it can avoid the common envelope phase and the interaction will proceed via stable Roche lobe overflow and/or wind accretion. A scenario of the circumbinary disk formation, proposed by Frankowski & Jorissen (2007) is as follows:

1. During the strong wind phase experienced by the primary, an accretion disk forms around the companion. The companion accretes mass and angular momentum, spinning up in the process. The orbital evolution proceeds roughly as in spherically symmetric Jeans mode, which assumes that the mass is lost by the system gradually and produces no forces (“kicks”) on the components of the binary (Huang, 1963). The period  $P$  of the system increases according to

$$\frac{\delta P}{P} = -2 \frac{\delta M}{M} \quad (1.7)$$

where  $M$  is the total mass of the system. Eccentricity of the orbit is not affected. The system is well detached at this stage.

2. Tidal forces and evolutionary expansion of the primary bring it closer to filling its Roche lobe. The outflow becomes concentrated in the direction of the companion, and happens even before the actual Roche lobe overflow (Frankowski & Tylenda, 2001). The total mass loss rate is enhanced by the presence of the companion and increases with the Roche lobe filling factor:

$$\frac{\Delta \dot{M}}{\dot{M}} \sim \left( \frac{R}{R_{RL}} \right)^3 \quad (1.8)$$

where  $R$  and  $R_{RL}$  are radii of the primary and its Roche lobe respectively. The matter is funneled through the vicinity of the  $L_1$  Lagrangian point. At the same time, a substantial amount of matter is outflowing through  $L_2$  or (after mass ratio reversal)  $L_3$  points.

3. The matter escaping through  $L_2/L_3$  points forms a spiral around the system (Figure 1.6). After one orbital period every portion of ejecta becomes shadowed from the primary by the newly ejected matter and is no longer accelerated outwards by the radiation pressure on dust. Part of the older ejecta gravitationally falls back onto the binary and collides with the outgoing flow. This process leads to the formation of a thick circumbinary torus.
4. The torus receives angular momentum from the binary and at the same time it is slowly pushed outwards by the radiation pressure on dust. The leftovers become a Keplerian disk. Only small part of the ejecta is pulled into Keplerian motion, so the angular momentum removal from the central binary is moderate and the orbital period can stay as long as a few hundred days.

#### 1.2.4 Physics and structure of circumbinary disks

The disks around post-AGB binaries are considered as passive disks, i.e. they are heated by the central star as opposed to accretion disks around black holes, which produce heat from the internal friction. Theoretical derivations based on the continuity and conservation of angular momentum show that the radial structure of the disk is governed by the following simple equation (see e.g. Dullemond & Penzlin, 2018):

$$\Sigma(r)\nu(r) = \text{const} \quad (1.9)$$

where  $\Sigma(r)$  is the surface density of the disk [ $\text{g}/\text{cm}^2$ ]; and  $\nu(r)$  is the turbulent viscosity arising due to the exchange of angular momentum between different radial layers of the disk. Turbulent viscosity depends on temperature and a turbulence parameter, which is not well constrained. Solutions of this equation with certain

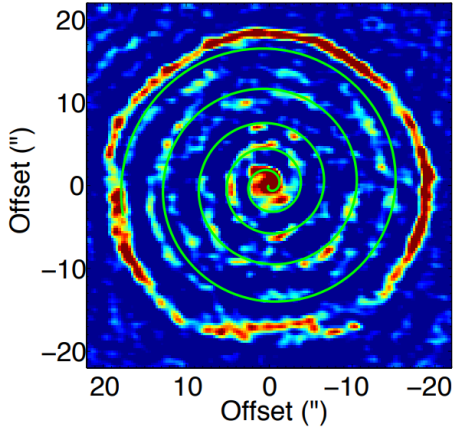


Figure 1.6: Spiral density waves of gas and dust around AGB binary R Scl, traced by CO( $J=3-2$ ) emission (Maercker et al, 2012). The material originates from a thermal pulse occurred  $\approx 1800$  years ago, which triggered a period of intense mass loss by the primary.

assumptions on the temperature profile of the disk show a monotonic decline of the disk surface density with increasing radius. Hydrodynamic simulations agree with the theory at larger radial distances, but show a different behavior closer to the central mass, where the density of the disk reaches a maximum value and then declines again. A more realistic model is therefore a double power law, where the density first increases till some critical radius and then declines more steeply to the outer edge of the disk (Figure 1.7, left). Another interesting feature found in simulations is the eccentricity of the inner edge of the disk, with typical values of 0.2...0.4 (Thun et al, 2017). Similar eccentricity was also found by Lines et al (2015) in hydrodynamic simulations as well. Probably as a result of the eccentric inner edge, the surface density is axially non-symmetric and shows a local densification at the point of apastron of the disk's inner edge (Figure 1.7, left). This densification is consistent with the lower orbital velocity at apastron, so that the disk particles accumulate at that position in their orbit.

Gravitational perturbation by the binary may induce various inhomogeneities in the disk. Lovelace et al (1999) showed that a linear instability may arise, if the disk has steep enough temperature gradients and the surface density is above 100...1000 g/cm<sup>2</sup>. The instability, commonly referred to as *Rossby wave instability*, gives rise to vortices that are well-known in thin two-dimensional planetary atmospheres, Jupiter's "Red Spot" being an example. A possible mechanism that can trigger the formation of vortices is the interaction between the matter from the Roche lobe overflow and the disk, which can form spiral shocks (Sawada, Matsuda & Hachisu, 1986). Once formed, a Rossby vortex propagates inwards, facilitating

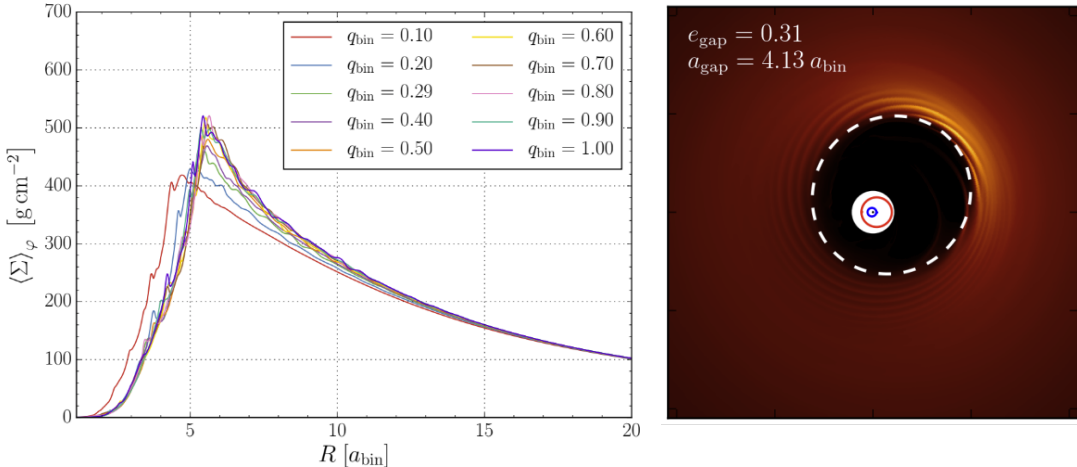


Figure 1.7: Circumbinary disk structure from hydrodynamical simulations, figures from Thun et al (2017). *Left:* Radial surface density profile, azimuthally averaged, as a function of the radial distance in the units of the orbital separation of the binary. *Right:* Disk surface density showing non-eccentricity of the inner rim and a local densification.

the transfer of angular momentum in the disk. Rossby vortices tend to accumulate dust particles, which migrate in the direction of the pressure gradient. As larger dust grains have a higher velocity relative to the gas, this migration leads to the fractionation of dust by the grain size, with larger grains accumulating in the vortex. One such “dust trap” was indeed discovered in a protoplanetary disk around the system Oph IRS 48 (van der Marel et al, 2013), where millimeter-sized grains were found accumulating on one side of the disk.

High-resolution direct imaging has also revealed spiral structures in (protoplanetary) disks, for example in the system HD 100453 (Wagner et al, 2018), which feature two spiral arms separated by  $\sim 180^\circ$ . These spiral arms are believed to be the result of the gravitational influence of a massive planet or a stellar companion. It is thus possible that similar spiral arms may exist in the disks around post-AGB binary systems. Miranda and Rafikov (2018) reproduced the formation of spiral arms analytically and in simulations and showed that the gravitational influence by the companion plays an indirect role through seeding initial perturbations, which then propagate and give rise to secondary waves.

Montesinos et al (2016) suggested that spiral structures in a disk may also be produced by the asymmetric shadowing of the outer part of the disk by its inner part. The shadow cast onto the disk leads to the periodic modulation in temperature, which affects the pressure distribution inside the disk. Such a shadowing was indeed observed (Cassassus et al, 2015), caused by an asymmetric concentration

of millimeter to centimeter-sized grains.

Advancements in interferometry provided detailed information on the structure of some of the disks around post-AGB binaries. The observable in interferometry is visibility, which is the Fourier transform of the intensity distribution over the sky. Unlike direct imaging, interferometry only gives information about Fourier transform of the object's brightness for a set of discrete spatial frequencies, determined by the interferometer baselines. However, the sampling of the Fourier space with modern interferometers is dense enough so that a reconstruction of the original brightness distribution is possible (Kluska et al, 2014). Interferometric observations of a disk around a post-AGB binary V390 Vel made by Kluska et al (2018) revealed that the position of the inner edge (rim) of the disk is consistent with the sublimation temperature of refractory elements constituting the dust. The brightness of the disk was found to be axially non-symmetric, with a maximum roughly at the azimuthal position of the primary and a secondary maximum at the other side of the inner rim (Figure 1.8).

### 1.3 The aim of this thesis

It is clear that the observed structure of circumbinary disks in post-AGB systems is quite complex. This complexity is an element of the larger puzzle of formation of such disks and their effect on the post-AGB binary evolution. Particular questions that can be asked are:

- What is the origin of the observed brightness asymmetry of the disk?
- How does the binary affect the dynamics of the inner rim of the disk?
- What determines the position of the disk surface density maximum?
- Can the inner rim of the disk be eccentric, and if so under what conditions?

The aim of this thesis is to answer the question about the origin of the disk brightness asymmetry in V390 Vel. The leading and most simple hypothesis is that the asymmetry is caused by the non-symmetric irradiation by the luminous primary. The asymmetry in irradiation acts on two different timescales: as the primary moves along its orbit, the closest point to the disk shifts with the period equal to the orbital period of the binary; in addition to that, the orbit of the binary is eccentric, consequently, one side of the disk systematically receives more radiation than the other, on average over a time period much longer than the orbital period. Confirming or disproving this explanation requires understanding of the thermal response of the disk, which is determined by the thermal interaction between radiation, dust and gas in the disk. The changing irradiation can also

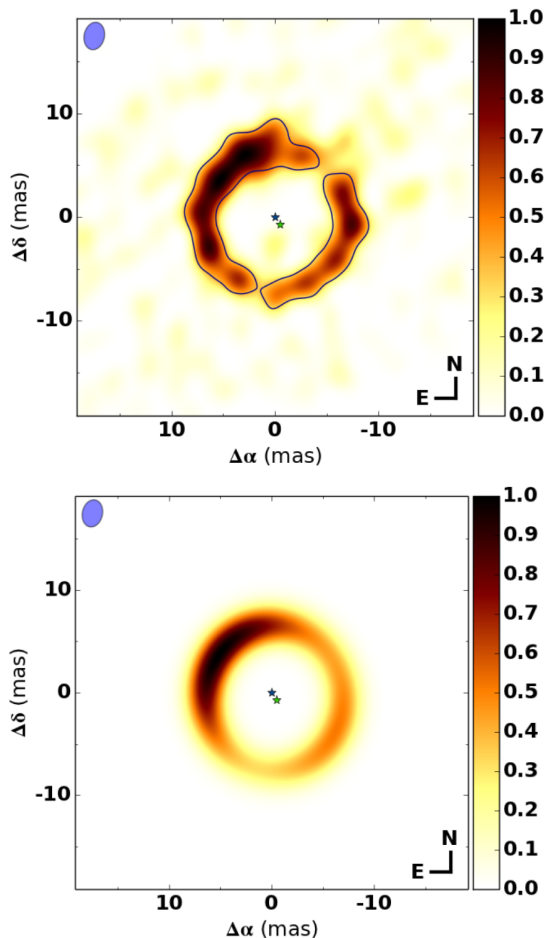


Figure 1.8: Intensity distribution of the V390 Vel system based on interferometric data; images from Hillen et al (2016). *Top:* direct reconstruction using SPARCO code developed by Kluska et al (2014). *Bottom:* parametric model of the ring fitted to interferometry data.

potentially lead to the cycles of evaporation and condensation of dust grains, thus shifting the radial position of the inner rim.

An alternative hypothesis is that the asymmetry in brightness is caused by the asymmetry in the disk structure, e.g. the surface density or the difference in grain sizes. Possible mechanisms that can cause such asymmetry are: the local Rossby wave instability, which leads to the formation of a vortex that traps the dust inside (Lovelace & Romanova, 2014); shadowing pats of the inner rim by the spiral density structures originating from the binary perturbation, as it was shown at larger scale in disks around young binaries (Monnier et al, 2019).

Finally, part of the asymmetry could be originating from the effect of the disk inclination and non-isotropic scattering of light by the dust grains.

The rest of this thesis is structured as follows. In Chapter 2 we review observational properties of post-AGB binaries in general and V390 Vel in particular. Chapter 3 deals with the estimation of the fundamental binary parameters and with the reconstruction of its binary evolution history. In Chapter 4 we study micro-scale physical processes in the disk: thermal equilibrium between dust, gas and radiation; as well as the stability of the dust sublimation front. Chapter 5 presents the radiative transfer model of the disk, irradiated by the off-center binary, and discusses the synthetic images obtained with the model. Chapter 6 contains conclusions and plans for the future research.

# Chapter 2

## Observational properties of post-AGB binaries

V390 Vel is a binary post-AGB system, located in the constellation Vela, at a distance of  $\sim 1.6$  kiloparsec from the Sun. It was first identified in IRAS data by its color, typical for RV Tauri class of post-AGB systems. V390 Vel hosts a dusty disk around the central binary, which is evident from the infrared excess, as well as the high-resolution interferometric data, which shows the hot inner edge of the disk. In this chapter we review general observational properties of post-AGB binaries and the V390 Vel system in particular.

### 2.1 General properties of post-AGB binaries

*This section is inspired by Van Winckel (2018), “Binary post-AGB stars as tracers of stellar evolution”.*

#### 2.1.1 Spectral energy distribution

Spectral energy distributions (SED) of binary post-AGB stars have common and distinct properties. Typical SED of a post-AGB binary shows a clear near-infrared excess, interpreted as due to the thermal emission of dust. The temperature of the excess emission, which is close to the dust sublimation temperature, indicates that the dust must be located near to the central star (Van Winckel, 2018). It is now well established that this type of SED indicates the presence of a stable compact circumbinary disk in the system (De Ruyter et al, 2006). The peak of the dust excess emission is located at around  $\sim 10 \mu\text{m}$ ; this is in contrast to post-AGB stars with detached shells of gas and dust that expanded and cooled, resulting in an excess emission peaked at  $30\text{-}60 \mu\text{m}$  (Van Winckel, 2003).

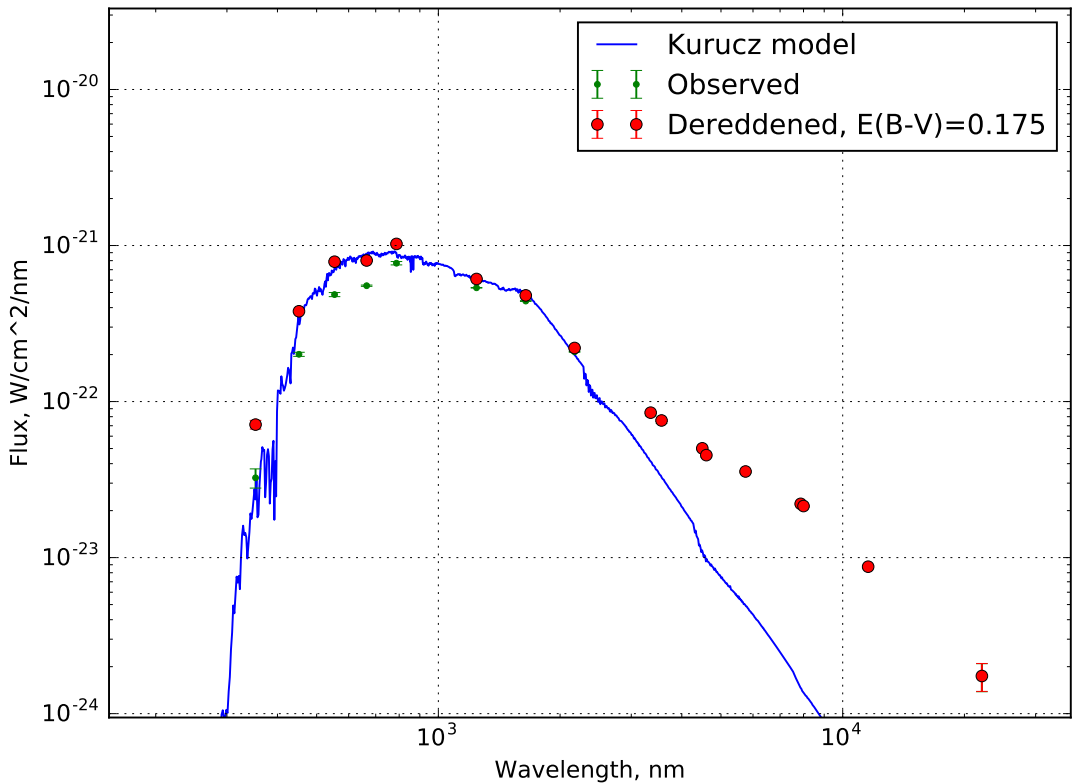


Figure 2.1: Spectral energy distribution of a post-AGB system with a disk J010254.90-722120.9 in Small Magellanic Cloud. The dots are the photometry data (observed and de-reddened) and the solid line is the Kurucz model flux of the star, fitted to the de-reddened data. The infrared excess, evident from the deviation of the photometry data from the model, indicates the presence of dust in the system, which re-radiates the energy absorbed from the star at longer wavelengths.

### 2.1.2 Keplerian velocity field traced by CO

Interferometric observations of CO emission provide a direct evidence for the presence of dust disks in post-AGB binary systems. A velocity field produced by the Keplerian motion of the dust and gas (which are kinematically coupled), can be spatially resolved with millimeter interferometry. Bujarrabal et al (2017) performed observations of post-AGB binary system IW Car using ALMA and produced intensity maps of  $^{12}\text{CO}$  and  $^{13}\text{CO}$  J=3-2 rotational lines ( $\lambda = 0.8 \text{ mm}$ ). The maps show a Keplerian velocity field with  $V=2.5 \text{ km/s}$  at 130 AU radial distance from the barycenter. This velocity corresponds to a central mass of  $1_{-0.4}^{+0.6} M_\odot$ , which is reasonable for a low-mass post-AGB system. Apart from the disk, an extended outflow of gas from the system was detected. Based on the velocity of the outflow, the authors (Bujarrabal et al, 2017) estimate that the disk was formed  $\sim 1000$  years ago and its future lifetime is  $\sim 8000$  years. A similar study was also performed for another post-AGB binary AC Her (Bujarrabal et al, 2015) and also found a Keplerian velocity field, indicating the presence of a disk.

### 2.1.3 Infrared dust properties

Infrared observations of a sample of binary post-AGB systems with SPITZER in the wavelength range of 5...37  $\mu\text{m}$  were performed by Gielen et al (2008). A number of features was observed in the spectra, identified as produced by olivine ( $\text{Mg}_{2x}\text{Fe}_{2(1-x)}\text{SiO}_4$ ), forsterite ( $\text{Mg}_2\text{SiO}_4$ ) and enstatite ( $\text{MgSiO}_3$ ). Fitting the spectra with a radiative transfer model of the dust allowed to infer that about 80% of the dust resides in 2  $\mu\text{m}$ -sized grains, and only 20% – in 0.1  $\mu\text{m}$ -sized. Therefore, small dust grains must have been efficiently reprocessed in these systems. The grains also have a high degree of crystallinity: the fraction of large grains in the crystalline component is above 70%, with both cool and hot crystalline grains identified. Crystalline phase is characterised by the ordered arrangement of molecules, as opposed to amorphous phase. Crystalline grains are formed when the cooling and condensation are slow, so that the atoms have time to find their places in the lattice. Hot grains are located in the inner region of the disk, where the temperature is above the annealing temperature. The presence of both hot and cool crystalline grains indicates either that there is a strong radial mixing in the disks, so that amorphous grains at the outer region of the disk have a chance to migrate inwards and undergo annealing; or that the crystalline dust existed from the moment of the disk formation in these systems.

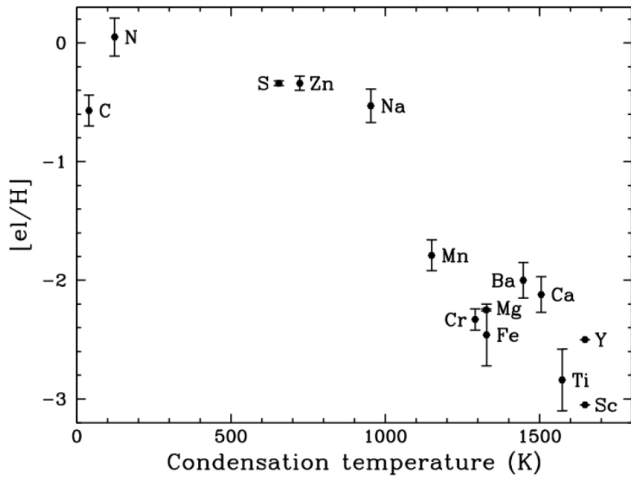


Figure 2.2: Typical depletion pattern of refractory elements in post-AGB stars, where the photospheric elemental abundances correlate with the dust condensation temperatures. Figure from Van Winckel (2018), originally adapted from Gielen et al (2009).

### 2.1.4 Depletion of refractory elements

Depletion is a chemical anomaly, observed in the photospheres of many post-AGB stars. In depleted systems, the abundance of refractory elements, i.e. elements that have high condensation temperatures, is low compared to the ambient level, while the abundance of volatile elements remains at the ambient level. A typical depletion pattern in post-AGB stars is shown in Figure 2.2. Good tracers of depletion are the  $[S/Ti]$  and  $[Zn/Ti]$  or  $[Zn/Fe]$  abundance ratios (Van Winckel, 2018). One possible explanation for the depletion is that the refractory elements are condensed into dust, the dust is fractionated from the gas by the radiation pressure, while the gas, cleaned of the refractory elements, is accreted onto the surface of the primary. Waters et al (1992) proposed that the most likely place for this process to occur is the stable dusty disk. This hypothesis is supported by the fact that depletion is only found in post-AGB systems with a disk and not in those with expanding shells. However, there are also post-AGB systems with a disk that are not depleted, such as U Mon. Another outlier is SS Gem, which is strongly depleted, but does not show any IR excess (Gezer et al, 2015). Giridhar et al (2005) suggested that the efficiency of depletion is affected by the stellar temperature: lower-temperature stars have deeper convective envelopes, which can mix the accreted material with the bulk of the envelope, thus diluting the apparent effect of depletion. However, Gezer et al (2015) found only a weak (although positive) correlation between the effective temperature and the depletion

in a sample of Galactic post-AGB stars. Thus, the presence of a disk is not a sufficient condition for the depletion to occur, but seems to be a prerequisite.

### 2.1.5 Jets

Orbital phase-resolved high-resolution spectral monitoring of a number of post-AGB binaries showed that H <sub>$\alpha$</sub>  line takes a P-Cygni profile when the companion is in front of the primary. Usually, P-Cygni profile is associated with wind outflow from massive stars. In case of binary post-AGB systems, the temporary appearance of P-Cygni profile is interpreted as due to a polar jet, originating from the companion, and becoming detectable in the spectrum only when it intersects the line of sight to the primary. The opening angle of the jet is wide ( $\sim 70^\circ$  for BD+46°442, see Bollen et al, 2017), although its accurate determination is difficult due to the degeneracy with the inclination. The presence of a polar jet indicates the ongoing accretion process. Possible sources of accretion are the direct mass transfer from the primary, or an accretion from the circumbinary disk. The outflow velocity in the jet is higher at the jet axis and lower at the cone edge. Similar phase-dependent H <sub>$\alpha$</sub>  profiles were detected in TW Cam and V421 CMa.

## 2.2 Properties of V390 Vel

*Sections 2.2.1 and 2.2.2 are based on Maas et al (2003).*

### 2.2.1 Spectral energy distribution

Photometric observations of V390 Vel were performed by Maas et al (2003). Observations in the UBVRI system were made with the Modular Photometer on the 0.5 m telescope at Sutherland on 54 nights from JD 2450858 to 2451666, and continued with the 0.75 m Automatic Photoelectric Telescope (APT) (Martinez et al, 2002) on 37 nights from JD 2451929 to 2452060. Infrared observations in the JHKL system were made with the Mark II Infrared Photometer on the 0.75 m reflector at Sutherland (SAAO). The spectral energy distribution (Figure 2.3) shows a broad infrared excess, starting at  $\sim 1 \mu\text{m}$ , which is typical for systems with disks rather than with expanding shells.

### 2.2.2 Radial velocity

A high resolution and high-SNR spectrum of V390 Vel was obtained with FEROS spectrograph, mounted on the 1.52 m ESO telescope at La Silla (Chile). This spectrum was used to construct a mask for cross-correlation, i.e. the list of lines used

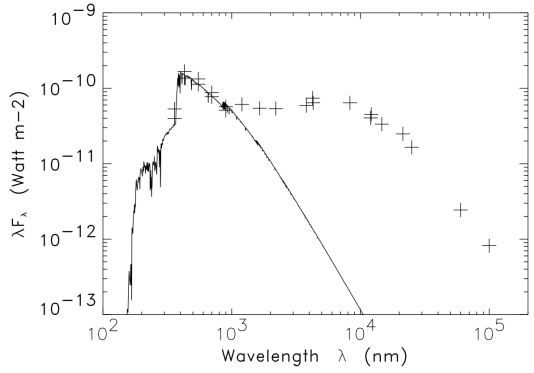


Figure 2.3: Spectral energy distribution for V390 Vel. From Maas et al (2003).

in the cross-correlation to find radial velocities. The custom mask was based on a standard mask for F-type stars, but with the number of lines reduced from 3074 to 953, by selecting only lines that are present in the FEROS spectrum of V390 Vel (Maas et al, 2003). Radial velocity monitoring was performed with CORALIE spectrograph, mounted on the Swiss telescope at La Silla (ESO, Chile). In total, 107 radial velocities were obtained (Figure 2.4), confirming that the system is a binary with a period of 499 days (later refined by Kluska et al (2018) to 506 days). Residuals from the orbital model revealed periodicities, interpreted as pulsations. The orbital parameters of V390 Vel are given in Table 2.1.

The spectra also showed a strong P-Cygni profile in H $\alpha$ , variable in time (Figure 2.5). The outflow velocity was estimated as variable between 100 and 400 km/s. Both the expansion velocity and the equivalent width of the absorption component in H $\alpha$  correlate with the orbital phase, indicating that the origin of the P-Cygni profile is a jet from the companion.

### 2.2.3 CO lines

Bujarrabal et al (2018) performed high-resolution observations of V390 Vel in  $^{12}\text{CO}$  and  $^{13}\text{CO}$  ( $J=3-2$ ) lines. Detailed modeling of the observations revealed that the material traced by CO is located in three distinct components: an inner disk in Keplerian rotation ( $r < 400$  AU), an outer disk in sub-Keplerian rotation with slow expansion ( $r < 1300$  AU), and an extended outflow with a velocity of  $\sim 5$  km/s ( $r < 1600$  AU). The authors estimate the total mass of the material around the system to be at most  $0.02 M_\odot$  with 90% of the material stored in the disk. Based on the angular momentum calculations, they conclude that the orbital separation<sup>1</sup> of the binary decreased by at least a factor of 2 due to the transfer of the angular

---

<sup>1</sup>Further on, we write “orbital separation” instead of “semi-major axis of the relative orbit”.

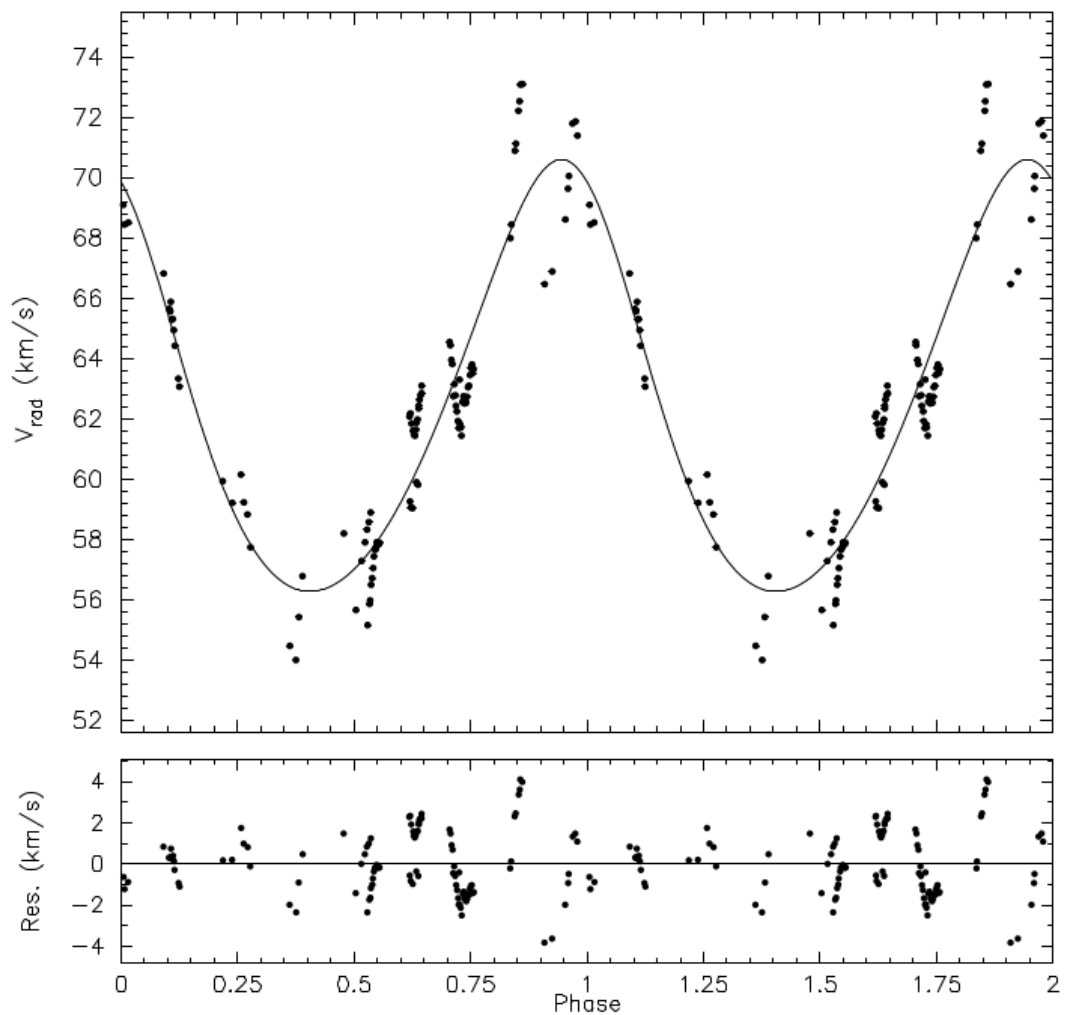


Figure 2.4: Radial velocity measurements and model for V390 Vel. From Maas et al (2003).

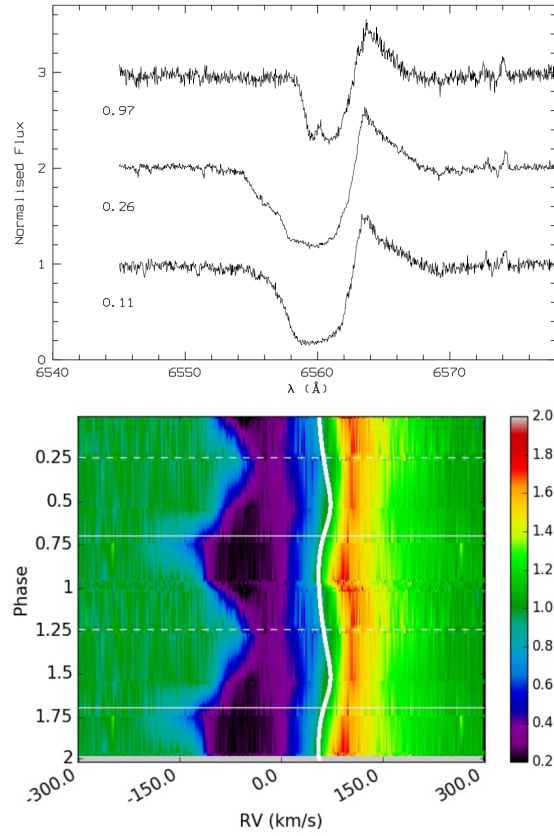


Figure 2.5: *Top:* H <sub>$\alpha$</sub>  line in the spectra of V390 Vel, from Maas et al (2003). The number inside the plot indicates orbital phase; phase 0.16 corresponds to the superior conjunction, i.e. when the companion is in front of the primary. *Bottom:* orbital phase-resolved H <sub>$\alpha$</sub>  line in the spectra of V390 Vel, from Kluska et al (2018). The thick solid curve shows the radial velocity of the primary, the solid and dashed horizontal lines indicate the superior and inferior conjunctions respectively.

momentum from the binary to the disk.

#### 2.2.4 Interferometry and disk structure

Interferometry observations by Hillen et al (2016) provided the first direct look into the disk structure around V390 Vel. The interferometric observations were made with the PIONIER instrument at VLTI. The brightness distribution was reconstructed from interferometry using SPARCO code by Kluska et al (2014). The distribution shows an asymmetric ring (Figure 1.8) with the angular diameter of  $14.15 \pm 0.10$  mas, or 18 times the binary separation, and a Gaussian FWHM= $3.2 \pm 0.1$  mas. The ring is interpreted as the inner rim of the circumbinary disk, heated by the luminous primary. The temperature of the inner rim was found to be  $\sim 1150$  K, which is close to the typical sublimation temperature of silicate dust grains (Kama et al, 2009). The ring emits a fraction of  $\sim 21\%$  of total flux from the system at the wavelength  $1.65 \mu\text{m}$ .

Emission from the companion ( $\sim 4\%$ ) and the background ( $\sim 15\%$ ) is also detected. The source of the background is unclear. The emission from the companion is most likely coming from accretion, which is consistent with the observed P-Cygni profiles in  $H\alpha$ .

Kluska et al (2018) performed a detailed modeling of the disk structure using MCMax radiative transfer code (Min et al, 2009). They were able to reproduce the spectral energy distribution of the system over a wide range of wavelengths from optical to 1 mm, with an excellent agreement. The radiative transfer model is axisymmetric, hence it does not reproduce the asymmetry of the disk. The azimuthal profile of the disk brightness, averaged between 5 and 9 mas from the centre of the disk, shows variation from 0.35 at  $140^\circ$  to 0.85 at  $240^\circ$  in arbitrary flux units. The width of the rim at the position of the maximum flux is  $\sim 2$  mas.

Table 2.1: Summary of the V390 Vel parameters (Maas et al, 2003; Kluska et al, 2018).

Parameter	Value	Description
$T_{\text{eff}}$	7250 K	Effective temperature
$\log(g)$	1.5	Surface gravity
$\xi$	4.50 km/s	Microturbulent velocity
$[M/H]$	-0.5	Metallicity
P	$506.0 \pm 1.3$ days	Orbital period
e	$0.22 \pm 0.02$	Eccentricity
$A_1 \sin(i)$	$0.39 \pm 0.01$ AU	Primary semi-major axis
$\omega$	$0.73 \pm 0.11$ rad	Argument of periastron
$T_0$	$51466 \pm 9$ MJD	Time of periastron passage
K	$8.7 \pm 0.2$ km/s	Velocity semi-amplitude
$\gamma$	$62.2 \pm 0.1$ km/s	Systemic velocity
$f(m)$	$0.031 \pm 0.002 M_{\odot}$	Mass function
$\theta_{\text{bin}}$	$0.81 \pm 0.05$ mas	Binary angular separation
$i_{\text{disk}}$	$19 \pm 2^{\circ}$	Disk inclination
PA <sub>bin</sub>	$56 \pm 3^{\circ}$	Binary position angle
PA <sub>disk</sub>	$6 \pm 6^{\circ}$	Disk position angle

# Chapter 3

## Binary evolution history of V390 Vel

In this chapter, in order to obtain a more comprehensive picture of the V390 Vel system, which is the object of this study, we refine the fundamental parameters of the binary and reconstruct its binary evolution history.

### 3.1 Estimating binary masses and separation

Kluska et al (2018) estimate only  $2\sigma$  lower limits on the masses, separation and other fundamental parameters such as luminosity and radius of the primary. The reason for this is that the angular separation of the binary ( $\theta_{bin} = 0.81 \pm 0.05$  mas) derived from interferometry data is lower than the formal resolution limit of the observations ( $\lambda/2B_{max} = 1.25$  mas). However, since the fundamental parameters of the binary will be required for the modeling, we estimate their actual values and uncertainties, *assuming* that  $\theta_{bin}$  was measured correctly.

Estimation of parameters is done in Monte-Carlo framework: we perform a number of independent simulations, where in each simulation we sample all the input parameters from their empirical distributions, calculate all the intermediate and final parameters and collect statistics for the final parameters. At the end of the calculations, the collected distributions of the final parameters are used to derive their moments (mean, two-sided errors). The calculations follow those in Kluska et al (2018), with minor differences. In particular, we assume that the mass of the primary equals to a typical mass of a white dwarf. This is justified if the primary has already lost its hydrogen envelope, so that the remnant core of the primary will evolve into a white dwarf without further mass loss. To check the validity of this assumption, we use the results for the synthetic post-AGB evolution from Frankowski (2003), where the author derived a model relation between the

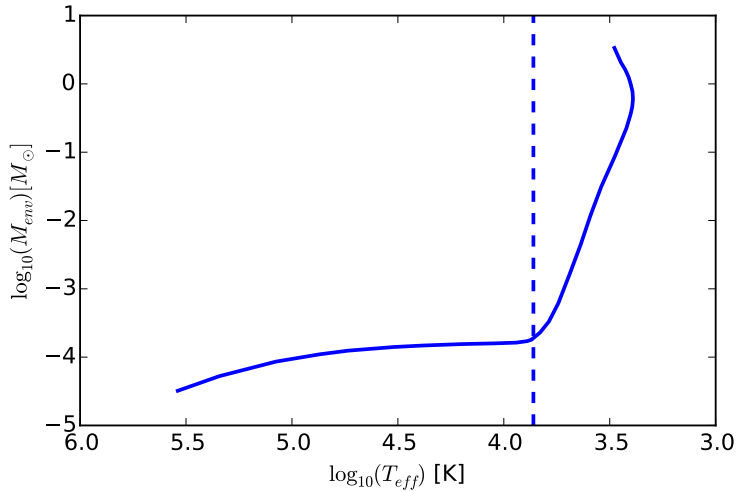


Figure 3.1: Model relation between effective temperature and the mass of the remaining envelope of a post-AGB star (solid line) from Frankowski (2003). The present effective temperature of V390 Vel (7250 K) is indicated with the vertical dashed line.

effective temperature and the mass of the remaining envelope of a post-AGB star (Figure 3.1). According to this model, the mass of the envelope in V390 Vel is  $2 \times 10^{-4} M_{\odot}$ . The mass of the primary is therefore very close to a typical mass of a white dwarf. Reliable data on the mass distribution of white dwarfs are available in Kepler et al (2007), based on SDSS DR4 data, where the authors construct the following five-component Gaussian mixture model describing the WD mass distribution:

$$\begin{aligned} P_{wd}(m) = & 0.38\mathcal{N}(m|0.603, 0.081) \\ & + 0.32\mathcal{N}(m|0.571, 0.034) \\ & + 0.19\mathcal{N}(m|0.775, 0.201) \\ & + 0.09\mathcal{N}(m|1.175, 0.076) \\ & + 0.02\mathcal{N}(m|0.358, 0.037) \end{aligned}$$

where  $P(x) = \mathcal{N}(x|\mu, \sigma)$  is a normal probability distribution. Sampling from this distribution is done by first randomly choosing a component according to its fraction in the mixture, and then sampling a random variable from the selected component. Each Monte-Carlo run involves the following sequence of steps:

1. Sample random values for  $P$ ,  $e$ ,  $\omega$ ,  $i_{disk}$ ,  $T_0$ ,  $A_1 \sin(i)$ ,  $f(m)$ ,  $\theta_{bin}$  (see Table 2.1), as well as the primary mass  $m_1$  from the WD mass distribution

and the bolometric flux  $F_{bol} = (2.31 \pm 0.20) \times 10^{-10}$  J/s/m<sup>2</sup> (derived from photometry). The value of a sampled random variable is given by:

$$x = \mu_x + \zeta \sigma_x \quad (3.1)$$

where  $\mu_x \pm \sigma_x$  is the empirical value of the variable, and  $\zeta$  is a standard normal random variable generated using **numpy.random.randn()** routine.

2. Calculate eccentric anomaly  $E$  from  $e$ ,  $P$ ,  $T_0$  at the epoch of the interferometric observation (2015-01-21) by solving Kepler's equation using Newton-Raphson algorithm.
3. Calculate the following Thiele-Innes constants:

$$X = \cos(E) - e \quad (3.2)$$

$$Y = \sin(E)\sqrt{1 - e^2} \quad (3.3)$$

4. Calculate companion mass  $m_2$  from the mass function by solving the cubic equation

$$m_2^3 \sin^3(i) - m_2^2 f(m) - 2m_2 m_1 f(m) - f(m) m_1^2 = 0 \quad (3.4)$$

using **numpy.roots()** routine and taking the real part of the zeroth root.

5. Calculate absolute binary separation as

$$A = \frac{m_1 + m_2}{m_2} \frac{A_1 \sin(i)}{\sin(i_{disk})} \quad (3.5)$$

6. Calculate projected binary separation using  $A$  and Thiele-Innes constants:

$$r_{proj} = A \sqrt{(\cos(\omega)X - \sin(\omega)Y)^2 + \cos^2(i_{disk})(\sin(\omega)X + \cos(\omega)Y)^2} \quad (3.6)$$

7. Calculate the distance to the system:

$$d = \frac{r_{proj}}{\theta_{bin}} \text{ kpc} \quad (3.7)$$

8. Calculate luminosity of the primary:

$$L_\star = 4\pi d^2 F_{bol} \quad (3.8)$$

9. Recalculate mass of the primary using mass-luminosity relation (Vassiliadis & Wood, 1994):

$$m_1/M_\odot = 0.5 + \frac{L_\star/L_\odot}{56694} \quad (3.9)$$

Table 3.1: Binary parameters of V390 Vel with  $1\sigma$  errors.

Parameter	Value
Distance, kpc	$1.57^{+0.18}_{-0.15}$
Luminosity of the primary, $L_\odot$	$17500^{+4600}_{-3500}$
Primary mass, $M_\odot$	$0.79 \pm 0.07$
Companion mass, $M_\odot$	$1.86^{+0.47}_{-0.33}$
Orbital separation, AU	$1.72^{+0.11}_{-0.08}$
Radius of the primary, $R_\odot$	$84^{+10}_{-9}$

10. Recalculate mass of the companion  $m_2$  from the mass function using the updated primary mass.
11. Recalculate semi-major axis of the relative orbit using Kepler's third law:

$$\frac{A}{[AU]} = \left[ \frac{m_1 + m_2}{M_\odot} \left( \frac{P}{[year]} \right)^2 \right]^{1/3} \quad (3.10)$$

The resulting estimates for the binary parameters are given in Table 3.1. The luminosity of the primary according to this estimate is at the very end of the typical luminosity distribution of post-AGB stars (Figure 3.3). It can therefore be argued that the angular separation  $\theta_{bin}$  of the binary is in fact close to its true value, because a smaller value of  $\theta_{bin}$  would result in a larger distance to the system according to Eq.(3.7) and, as a consequence, much higher luminosity according to Eq.(3.8). The distribution of the primary mass and its comparison to the WD mass distribution are shown in Figure 3.2.

## 3.2 Binary evolution code **binary\_c**

We use binary evolution code **binary\_c** to reconstruct evolution history of V390 Vel, i.e. the changes in the masses, separation and orbital period of the system with time. **binary\_c** takes as input initial parameters of the system and evolves it taking into account multiple factors affecting binary evolution such as mass transfer,

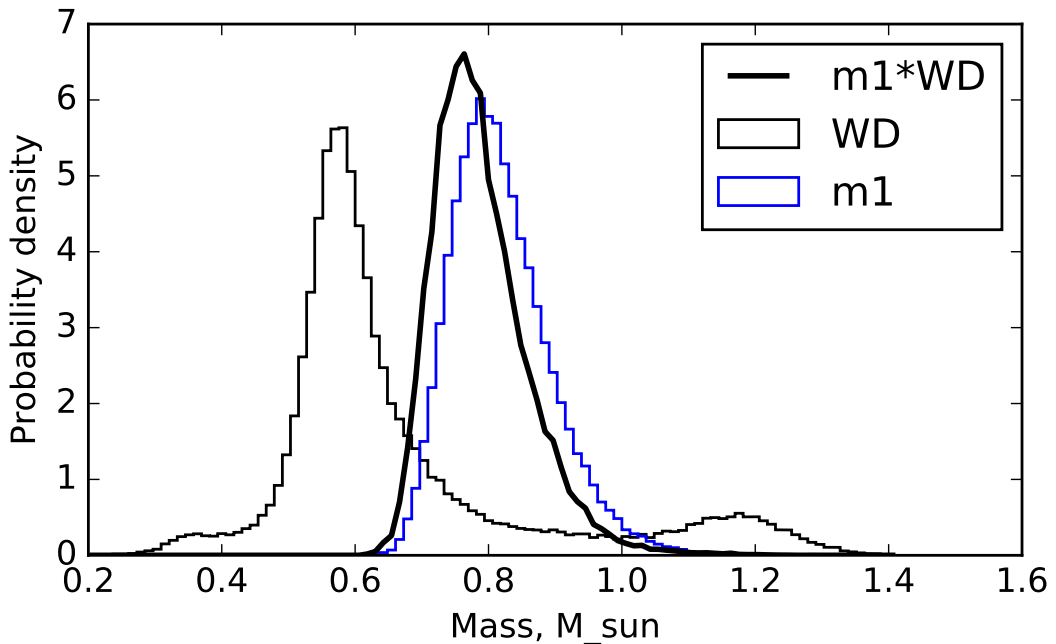


Figure 3.2: Primary mass distribution ( $m_1$ ), white dwarf (WD) mass distribution, and the posterior distribution for the primary mass (“ $m1*WD$ ”) using WD mass distribution as a prior.

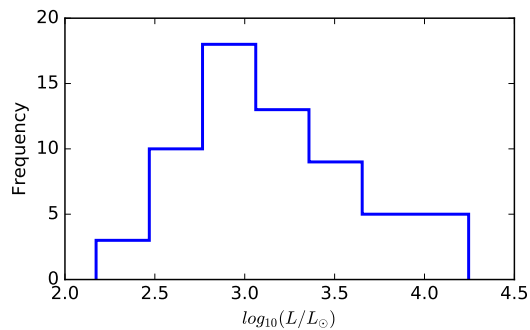


Figure 3.3: Luminosity distribution of post-AGB stars based on data from Kamath et al (2014).

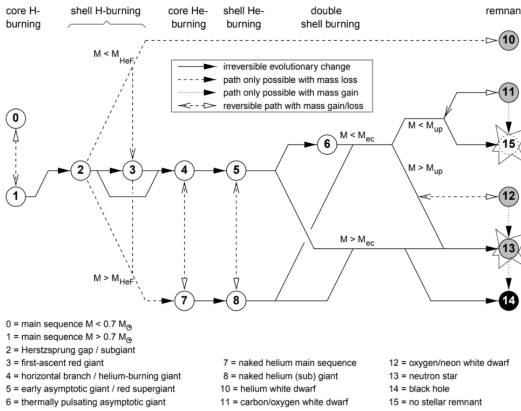


Figure 3.4: Possible paths through different stellar evolution stages, covered by `binary_c` code. Diagram from Hurley et al (2000).

mass loss due to wind, common envelope, loss of angular momentum, circularization of the orbit, etc. The description of physics and algorithms in `binary_c` can be found in Hurley et al (2000, 2002), Izzard et al (2004, 2006, 2009), Claeys et al (2014), de Mink et al (2014), Abate et al (2015). At the moment of writing, implementing the eccentricity pumping from the interaction with a disk in `binary_c` is still in development, so the results below do not take this effect into account.

The stellar structure part of the code is based on the analytical approximations given in Hurley et al (2000), based on a grid of stellar models computed by Pols et al (1998). The approximate formulas allow calculating the changes in the luminosity and radius of a star, as a function of age, for a given initial mass and metallicity. The evolutionary stages covered by the code are: main sequence, Hertzsprung gap, first giant branch, core helium burning, asymptotic giant branch, naked helium star. Possible evolutionary paths between different stages are shown in Figure 3.4. The mass loss on AGB is based on the formulation of Vassiliadis & Wood (1993).

The binary evolution part of the code is based on the rapid binary evolution algorithm presented in Hurley et al (2002). The initial state of the system is described by the masses  $M_1$ ,  $M_2$  of the stars, period  $P$  and eccentricity  $e$ . The system begins with both stars on the zero-age main sequence. Each star has its own evolution time step, restricted to prevent the change of the mass by more than 1% and the radius by more than 10%. An additional restriction to the time step is for the change of the angular momentum of the binary system to be below 2%. If the primary fills its Roche lobe, then the time step is interpolated so that the radius of the primary is just above the Roche lobe radius ( $1 \leq R_1/R_{L1} \leq 1.002$ ).

An important aspect of binary evolution is the tidal dissipation of energy. The most efficient form of tidal dissipation is turbulent viscosity in the convective

regions. Tidal dissipation has two effects: synchronization of the spins with the orbital motion, and circularization of the orbit. The final state, where the binary system rotates as a solid body, has the lowest total energy. The evolution of spins and eccentricity under the effect of tidal dissipation is modeled in `binary_c` code based on equations from Hut (1981).

### 3.3 Binary evolution modeling

In order to obtain an independent estimate for the initial mass of the primary, we used initial-final mass relations (IFMR) from Vassiliadis & Wood (1994) and Cummings et al (2018). The IFMR from Cummings et al (2018) is based on the analysis of 79 white dwarf from 13 star clusters, for which the authors measured  $T_{\text{eff}}$ ,  $\log(g)$  and derived the mass, cooling age and luminosity of each WD. The evolution time of a white dwarf equals the age of its parent cluster minus the cooling age. The knowledge of the evolution time allows to estimate the initial mass using stellar evolution models. We used the IFMR based on MESA models, which is given by:

$$M_f = (0.187 \pm 0.061)M_i + (0.184 \pm 0.199)M_{\odot} \quad (3.11)$$

where  $M_i$  and  $M_f$  are the initial and final mass respectively. We calculated the initial mass and its uncertainty by randomly sampling the final mass from its distribution obtained in the previous section, and the coefficients of Eq.(3.11). The resulting estimate for the initial mass of the primary is  $M_1 = 3.25^{+2.0}_{-1.3} M_{\odot}$ .

The IFMR from Vassiliadis & Wood (1994) is based on stellar evolution models with mass loss. The relation is given by:

$$M_f = 0.473 + 0.084M_i - 0.058 \log_{10}(Z/Z_{\odot}) \quad (3.12)$$

where  $Z$  is the metallicity ( $\log_{10}(Z/Z_{\odot}) = -0.5$ , see Table 2.1). Calculations according to this relation give the initial primary mass  $M_1 = 3.4 \pm 0.8$ . The probability distributions of the initial mass for both relations are shown in Figure 3.5.

With the obtained estimate for the primary mass, we constructed a grid of binary evolution models, covering a range of primary masses from 1.5 to 5.0  $M_{\odot}$ . The grid was later refined for the primary mass range from 3.6 to 4.0  $M_{\odot}$  with smaller steps for orbital separation and eccentricity. The parameters of the grid are given in Table 3.2. The models were computed for the maximum evolution time 15 Gyr, with default `binary_c` settings except for the `ROTATION-ALLY_ENHANCED_MASS_LOSS` parameter switched from “2” to “0”. The total number of models in the grid is 43380. Searching the grid for the best-fit model was done using  $\chi^2$  for the three parameters: primary mass, companion mass and

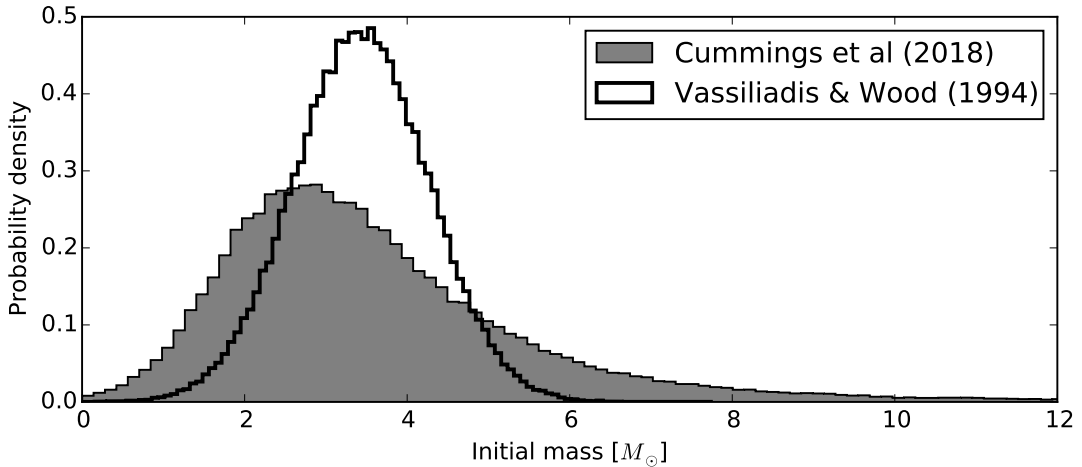


Figure 3.5: Initial mass of the primary estimated using two different initial-final mass relations.

orbital separation. We did not include eccentricity into the  $\chi^2$  criterion because the current eccentricity of V390 Vel is believed to be due to the interaction with the disk, which is not taken into account in the **binary\_c** version we used (v2.0pre29).

The best-fit model achieves a  $\chi^2 = 0.09$ , which can be considered a good fit ( $1\sigma$  is at 5.2 for  $\chi^2$  with 3 degrees of freedom). The best-fit initial parameters of the binary are:  $m_1 = 3.8 M_\odot$ ,  $m_2 = 1.7 M_\odot$ ,  $e = 0.3$ ,  $A = 8.4$  AU. Thus the orbital separation has shrunk by a factor of 5 to the present value of 1.7 AU. The non-zero initial eccentricity is favoured by the majority of models with  $\chi^2 < 5.2$ , which is interesting considering that the system went through the common envelope stage, where the orbit is circularized. There is a positive correlation between the eccentricity and orbital separation (Figure 3.6); it can be understood taking into account that stars on more eccentric orbits have a closer approach at periastron, so that a higher eccentricity compensates for a larger separation in regard to the initiation of the mass transfer.

The evolution of the system, according to the best-fit model, proceeds as follows. After 200 Myr the primary finishes its main sequence life and 40 Myr later reaches thermally pulsing AGB stage. It starts filling its Roche lobe and at the same time the orbit starts to shrink. Its mass decreases slightly due to the wind mass loss. At the point where the primary Roche lobe filling factor reaches  $\sim 0.9$ , an unstable mass transfer is initiated during which the primary loses most of its envelope. By this point the orbit is already circularized by tidal friction. The orbit shrinks until the mass inversion occurs, at which point the orbital separation is still large (6.5 AU). After the mass inversion, the orbit starts to widen again;

Table 3.2: Parameter ranges in the grid of binary evolution models. The grid is a two-resolution grid and includes both parameter ranges in the two parts of the table.

Parameter	Range of values
Primary mass	$[1.5, 1.6, \dots, 5.0] M_{\odot}$
Companion mass	$[1.0, 1.1, \dots, m_1] M_{\odot}$
Orbital separation	$[1000, 1200, \dots, 2400] R_{\odot}$
Eccentricity	$[0.0, 0.1, \dots, 0.5]$
Primary mass	$[3.6, 3.7, \dots, 4.0] M_{\odot}$
Companion mass	$[1.5, 1.6, \dots, 1.9] M_{\odot}$
Orbital separation	$[1700, 1710, \dots, 1900] R_{\odot}$
Eccentricity	$[0.00, 0.05, \dots, 0.50]$

however, this process is interrupted by the onset of the common envelope stage and the orbital separation drops to its present value of 1.7 AU. By the end of the common envelope stage, the system consists of a white dwarf and a main-sequence companion.

Further evolution is triggered when the companion evolves off the main sequence, which happens after 1.6 Gyr. However, the companion never reaches the thermally pulsing AGB stage. Instead, unstable RLOF and the onset of the common envelope occur when it is still at the early AGB stage, 210 Myr later. After the common envelope, the mass of the companion is  $0.55 M_{\odot}$ . The system ends as a pair of white dwarfs on a short orbit with a separation  $\sim 0.07$  AU. The evolution of the system parameters is plotted in Figure 3.7, and a magnified part around the first mass transfer is shown in Figure 3.8.

### 3.4 Conclusions

V390 Vel is a post-AGB binary system, where the primary has lost most of its hydrogen envelope and its mass is close to that of a white dwarf. The companion is a main-sequence star with a mass of  $\sim 1.9 M_{\odot}$ . The likely age of the system is  $\sim 240$  Myr. According to the best-fit binary evolution model, the system went through a common envelope stage, after which its orbital separation decreased by a factor of  $\sim 5$ . The present eccentricity of the system is 0.22, therefore, if the binary evolution model is correct, it is most likely a result of the eccentricity pumping due to the interaction with the circumbinary disk.

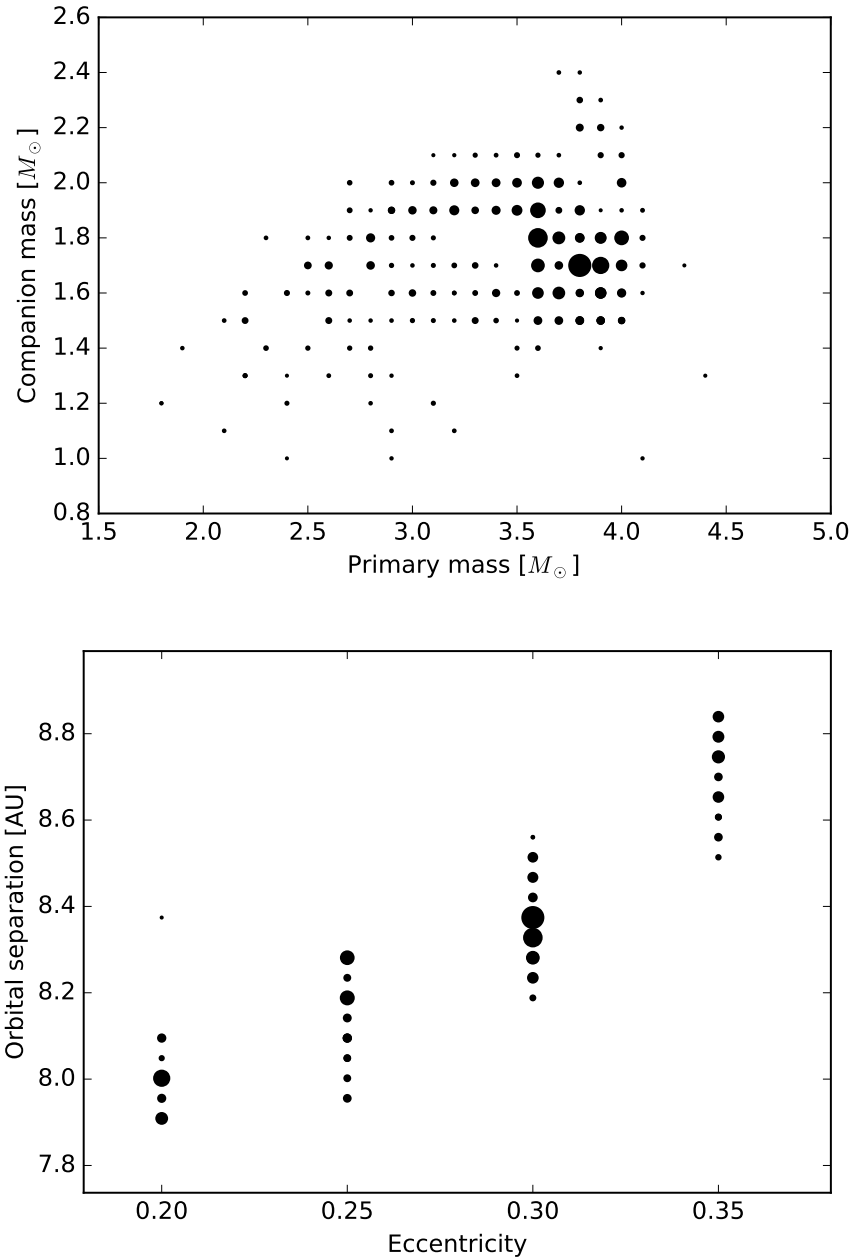


Figure 3.6: Correlations between parameters of best-fit models (within  $2\sigma$ ) from the binary evolution grid. The size of the marker is inversely proportional to the  $\chi^2$  value, i.e. better-fitting models have larger marker sizes.

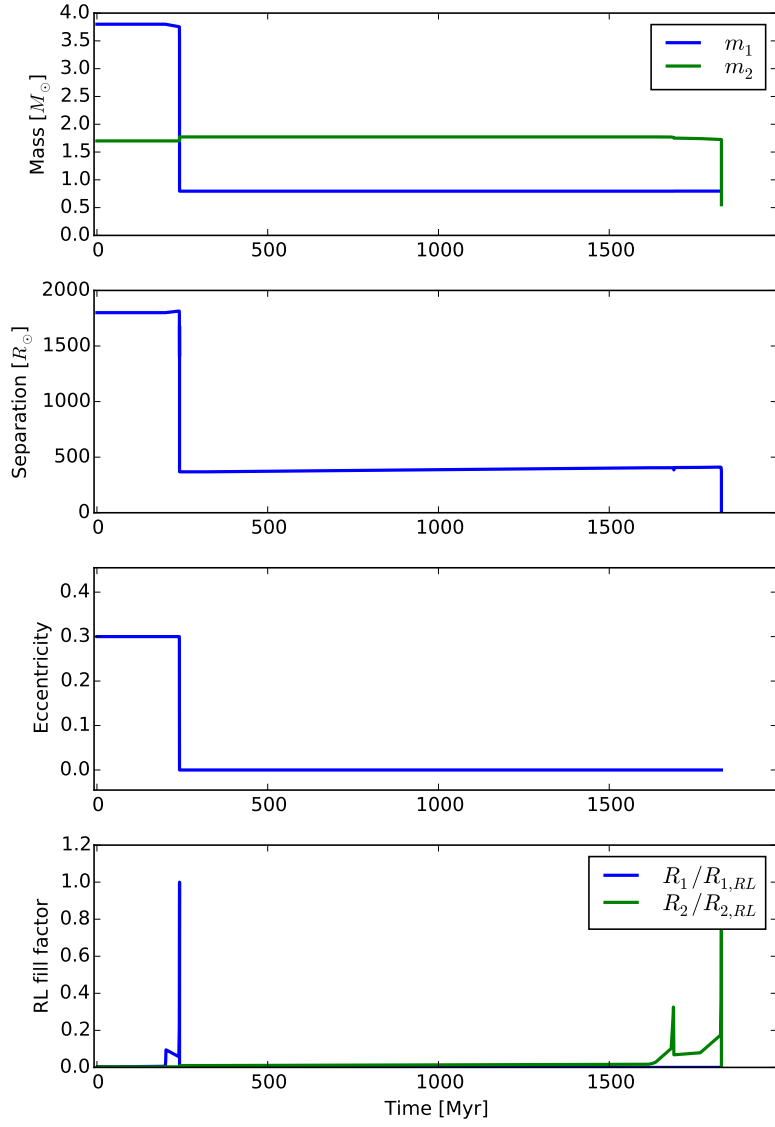


Figure 3.7: Binary evolution history of V390 Vel according to the best-fit **binary\_c** model. From top to bottom: masses, orbital separation, eccentricity, Roche lobe filling factor.

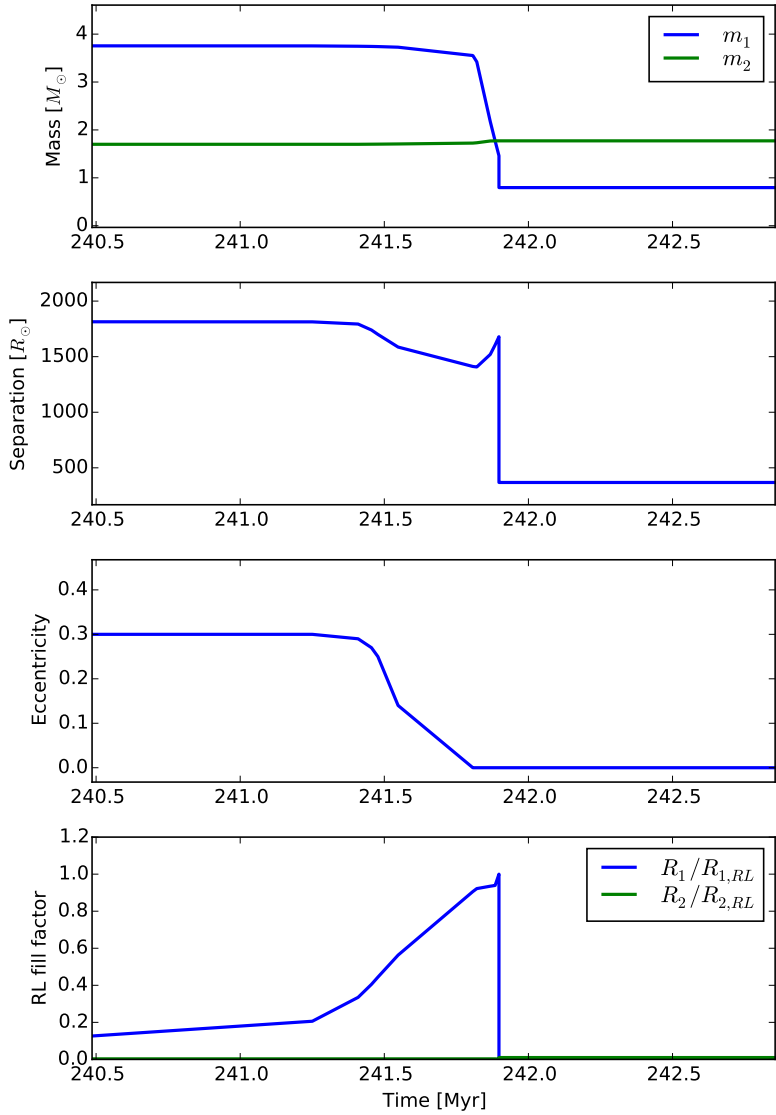


Figure 3.8: Binary evolution history of V390 Vel according to the best-fit **binary\_c** model, magnified to the first Roche lobe overflow. From top to bottom: masses, orbital separation, eccentricity, Roche lobe filling factor.

# Chapter 4

## Micro-scale physical processes in the disk: dust sublimation and interaction with gas

Our working hypothesis that can potentially explain the observed brightness asymmetry of the disk around V390 Vel is that the azimuthal temperature distribution in the disk is asymmetric due to the irradiation by the primary, which is always located off the barycenter of the binary system, closer to one side of the disk. Before we can proceed with the radiative transfer modeling of the entire disk, it is necessary to understand the interaction between the components of the disk – gas and dust – on the micro-level. Of particular interest are the timescales of thermal equilibration of the dust grains with the radiation field, and cooling of the dust grains by the gas. Understanding these thermal timescales is important to make a decision on whether it is necessary to model the dynamics of heat transfer in the disk, or it is sufficient to model the steady state temperature distribution. This decision depends on whether these thermal timescales are shorter or longer than the orbital period of the binary. In addition, we have to determine whether the changing irradiation from the primary as it moves along the orbit can lead to the sublimation of the dust grains in the inner rim of the disk, thus shifting the position of the rim. If we find that the inner rim shifts in response to the motion of the primary, our working hypothesis can be dismissed without further investigation.

### 4.1 Asymmetric irradiation of the disk by the primary

Since the central source illuminating the disk is a binary, the amount of radiation received by different parts of the disk is not equal at any point in time. Assuming

that the center of mass of the disk coincides with the barycenter of the binary, we can calculate the maximum difference in equilibrium temperature along the inner rim of the disk. The equilibrium temperature at a distance  $r$  from the star is given by:

$$T_{eq}(r) = W(r)^{\frac{1}{4}} T_{\star} \quad (4.1)$$

where  $W(r)$  is the geometric dilution factor:

$$W(r) = \frac{1}{2} \left\{ 1 - \left[ 1 - \left( \frac{R_{\star}}{r} \right)^2 \right]^{1/2} \right\} \quad (4.2)$$

The radial distance of the primary from the barycenter at the periastron and apoastron is given by:

$$r_{ap} = A_1(1 + e) \quad (4.3)$$

$$r_{peri} = A_1(1 - e) \quad (4.4)$$

where  $A_1$  is the semi-major axis of the primary barycentric orbit. The minimum and maximum equilibrium temperature at the opposite sides of the disk can be calculated for two positions of the primary. When the primary is at periastron, these are given by:

$$T_{\max,peri} = T_{eq}(r_{rim} - r_{peri}) \quad (4.5)$$

$$T_{\min,peri} = T_{eq}(r_{rim} + r_{peri}) \quad (4.6)$$

When the primary is at apoastron, the temperatures are:

$$T_{\max,ap} = T_{eq}(r_{rim} - r_{ap}) \quad (4.7)$$

$$T_{\min,ap} = T_{eq}(r_{rim} + r_{ap}) \quad (4.8)$$

where  $r_{rim}$  is the radial distance to the inner rim of the disk ( $r_{rim} \approx 8.25$  AU according to Kluska et al, 2018). Furthermore, the equilibrium temperature can be translated into the intensity of the emitted radiation, assuming that the dust emits as a blackbody:

$$I = B_{\lambda}(T) = \frac{2hc^2}{\lambda^5} \frac{1}{e^{hc/\lambda kT} - 1} \quad (4.9)$$

Results of the calculations for the two positions of the primary are given in Table 4.1. The intensity ratio is the most important parameter, because it determines whether it is theoretically possible to explain the brightness (intensity) asymmetry of the disk found in observations. The calculations show that the intensity ratio varies from 2.5 when the primary is at periastron to 4.2 when it is at apoastron. The intensity ratio is calculated for the wavelength  $\lambda = 1.6 \mu\text{m}$ , which is

Table 4.1: Minimum and maximum distances of the primary to the inner rim of the disk, temperature and intensity ratios for the two positions of the primary.

Parameter	At periastron	At apoastron
$r_{\min}$	7.3 AU	6.8 AU
$r_{\max}$	9.2 AU	9.7 AU
$T_{\min}$	1057 K	1028 K
$T_{\max}$	1185 K	1230 K
$T_{\max}/T_{\min}$	1.121	1.196
$I_{\max}/I_{\min}$ at $\lambda = 1.6 \mu\text{m}$	2.5	4.2

equal to the wavelength of interferometric observations. The azimuthal variation of the disk brightness found in observations is from 0.35 to 0.85 (arbitrary flux units) at approximately opposite sides of the disk, or the brightness ratio of  $\approx 2.4$  (from Figure 9 in Kluska et al, 2018). It is therefore *theoretically possible* that the asymmetric irradiation by the primary can cause such asymmetry in the observed disk brightness. The rest of this chapter is aimed at the detailed modeling of the physical processes in the disk in order to test if the asymmetric irradiation can actually produce the observed disk brightness asymmetry. The asymmetric irradiation alone is not a sufficient factor to produce the brightness asymmetry, because it is necessary to show that the local temperature of the disk can adjust to the changing flux quickly enough, i.e. on a timescale shorter than the orbital period. The rate of the temperature adjustment is determined by the rate of the heat transfer from the inner rim to the deeper layers of the disk: the local warming of the dist in the inner rim is only possible if the heat transfer rate is not high enough to cool it down. In addition, the eccentricity of the binary orbit causes one side of the disk to regularly receive a larger amount of flux than the other side, on the average over a large number of orbital periods. Can this also contribute to the asymmetry in the disk temperature, hence brightness? The answer to this question depends on the heat storage capacity of the disk and its rate of cooling via radiation into the empty space.

## 4.2 Thermal interaction between dust, gas and radiation

The aim of this section is to estimate the rates of energy transfer between the two constituents of the disk (dust and gas), and the radiation field of the primary.

### 4.2.1 Dust-radiation equilibrium

The luminosity of a dust grain with the radius  $a$  and temperature  $T_d$  is given by:

$$L_d = 4\pi a^2 \sigma T_d^4 \quad (4.10)$$

The power absorbed by the grain at a distance  $r$  from the primary is:

$$E_{abs} = \frac{L_\star}{4\pi r^2} \pi a^2 = F \pi a^2 \quad (4.11)$$

The rate of change in the internal energy  $Q$  of the dust grain is the difference between the absorbed and irradiated power:

$$\frac{dQ}{dt} = E_{abs} - L_d = \pi a^2 (F - 4\sigma T_d^4) \quad (4.12)$$

The rate of change in the grain temperature depends on the mass and heat capacity of the grain, assuming that the heat is transferred instantaneously from the surface to the centre of the grain:

$$\frac{dT_d}{dt} = \frac{1}{m_g C_d} \frac{dQ}{dt} \quad (4.13)$$

where  $m_g$  is the mass of the grain,  $m_g = (4/3)\pi a^3 \rho$ ;  $C_d$  is the specific heat capacity of the grain material in [erg/g/K]. The rate of the temperature change is therefore given by:

$$\frac{dT_d}{dt} = \frac{F - 4\sigma T_d^4}{(4/3)a\rho C_d} \quad (4.14)$$

The result of a numerical integration of the last equation for a 1 mm size grain is given in Figure 4.1, which shows that the grain achieves thermal equilibrium with radiation on a timescale of 10 seconds, which is 9 orders of magnitude faster than the orbital timescale ( $1.6 \times 10^{10}$  s). The rate of heating is inversely proportional to the grain size, hence smaller grains heat up even faster. Therefore we can assume that, for the practical purposes of disk modeling, the dust achieves equilibrium with radiation instantaneously.

### 4.2.2 Collisional heat transfer between dust and gas

Next we want to estimate how fast the gas can cool the dust grains by virtue of heat conduction. This is important since, if the gas can provide an efficient heat sink for the dust grains, we will need to take this into account in further modeling. The energy carried by an atom of an ideal monoatomic gas is

$$E = \frac{3}{2}kT_g \quad (4.15)$$

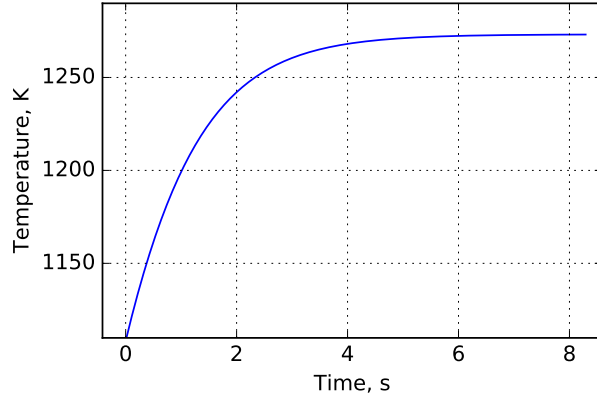


Figure 4.1: Thermal response of a 1 mm radius grain with a specific heat capacity of  $5 \times 10^6$  erg/g/K and a density of 3 g/cm<sup>3</sup>.

where  $k$  is the Boltzmann constant. When a gas atom hits a dust grain, it comes in with the energy  $(3/2)kT_g$  and leaves with the energy  $(3/2)kT_d$ , on average, where  $T_g$  and  $T_d$  are the gas and dust temperatures respectively. The amount of energy transferred in one collision is therefore

$$\Delta E = \frac{3}{2}k(T_d - T_g) \quad (4.16)$$

The rate of collisions of gas atoms with a dust grain of radius  $a$  is

$$R_{coll} = \pi a^2 n_H \langle v \rangle \quad (4.17)$$

where  $n_H$  is the number density and  $\langle v \rangle$  is the average thermal velocity of the gas atoms,

$$\langle v \rangle = \left( \frac{8kT_g}{\pi\mu} \right)^{1/2} \quad (4.18)$$

The rate of energy transfer between gas and a dust grain is given by the product of the collision rate and the amount of energy transferred in one collision:

$$\frac{dQ}{dt} = \pi a^2 n_H \langle v \rangle \frac{3}{2}k(T_d - T_g) \quad (4.19)$$

The rate of heating of the gas due to the heat transfer from dust is the product of the heat transfer rate for one grain by the number density of dust grains:

$$\frac{dT_g}{dt} = \frac{n_d}{\rho C_H} \frac{dQ}{dt} = n_d \pi a^2 \langle v \rangle (T_d - T_g) \quad (4.20)$$

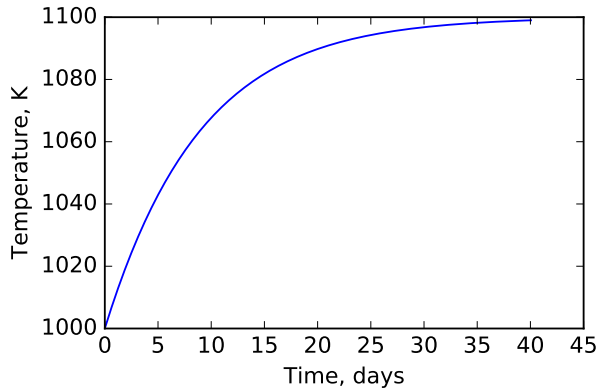


Figure 4.2: Heating of the gas from dust grains in typical conditions at the mid-plane of the disk with a surface density  $100 \text{ g/cm}^2$  and a scale height 3 AU. The radius of the dust grains is  $0.1 \mu\text{m}$ .

Numerical integration of this equation for typical gas density at the densest part of the midplane of a disk is shown in Figure 4.2. The time required for the gas temperature to reach equilibrium with dust (in the absence of radiation) is  $\sim 50$  days. This is 6 orders of magnitude slower than the timescale of dust-radiation eqilibration. It is therefore expected that the gas cannot cool the dust grains quickly enough to shift their temperature from the equilibrium with the radiation field. However, to make sure, in the next section we calculate the thermal equilibrium temperature of the dust grains with the radiation in the presence of the gas.

### 4.2.3 Radiation-dust-gas equilibrium

In the state of thermal equilibrium, the rate of energy transfer between radiation field and dust, given by Eq.(4.12), is equal to that between the dust and gas, which is given by Eq.(4.19). This yields the following equation for the dust temperature:

$$\pi a^2(F - 4\sigma T_d^4) = \pi a^2 n_H \langle v \rangle \frac{3}{2} k (T_d - T_g) \quad (4.21)$$

or, cancelling  $\pi a^2$

$$F - 4\sigma T_d^4 = n_H \langle v \rangle \frac{3}{2} k (T_d - T_g) \quad (4.22)$$

We solve this non-linear equation graphically, by plotting both sides as a function of the dust temperature. Figure 4.3 shows the plots for two different gas number density values: for typical conditions in a dense part of the disk ( $10^{12} \text{ cm}^{-3}$ ) and

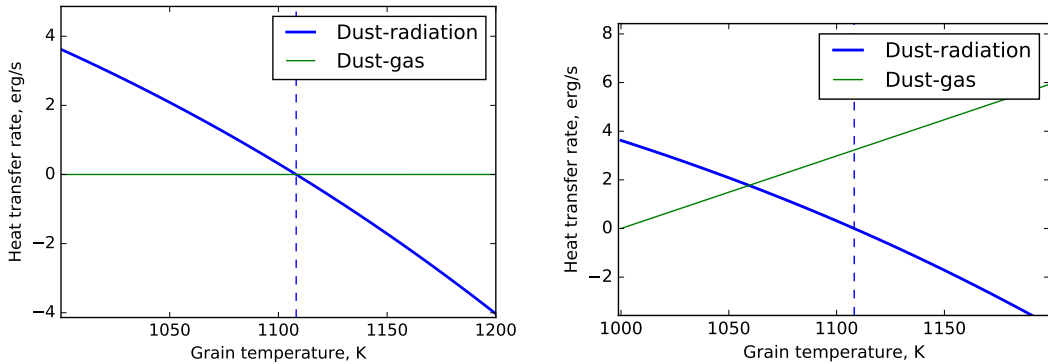


Figure 4.3: Thermal equilibrium between dust, gas and radiation: energy transfer rate as a function of temperature. The vertical dashed line shows dust-radiation equilibrium temperature, which would be achieved in the absence of gas. The two graphs are for different number density of gas atoms:  $10^{12} \text{ cm}^{-3}$  (left), which is typical for midplane of a dense part of the disk; and  $10^{16} \text{ cm}^{-3}$  (right).

four orders of magnitude higher density. According to these results, the presence of gas with a density typical for dense parts of the disk cannot shift the temperature of the dust to any significant degree. In order to make any effect on the dust temperature, four orders of magnitude higher gas density is required. This allows us to conclude that the dust in the disk exists in thermal equilibrium with the radiation field, with the cooling from the gas being negligible.

### 4.3 Disk cooling timescale

Finally, we need to check if the disk can accumulate any substantial amount of heat that could be released on the orbital timescale. Excluding this possibility will allow us to proceed with modeling only the steady-state thermal structure, without modeling the dynamics of the heat transfer with time-varying heat influx from the primary in its orbital motion. For this we estimate the time that it takes for the entire disk to cool, if the luminosity of the central source was to be dropped to zero. We consider a simple thermal disk structure defined by the following temperature profile as a function of the radial distance  $R$ :

$$T = T_{sub} \left( \frac{R}{R_{sub}} \right)^{-q} \quad (4.23)$$

where  $R_{sub}$  and  $T_{sub}$  are the radius and temperature of the sublimation front (inner rim). The luminosity of a ring  $dR$  at a radius  $R$  is

$$dL = 2\sigma T^4 2\pi R dR \quad (4.24)$$

The additional factor of 2 appears because the disk radiates from the two sides. The total luminosity is given by

$$L_{disk} = 4\pi\sigma T_{sub}^4 R_{sub}^{4q} \int_{R_{sub}}^{R_{max}} R^{1-4q} dR \quad (4.25)$$

where  $R_{max}$  is the radial extent of the disk. The integration yields

$$L_{disk} = 4\pi\sigma T_{sub}^4 R_{sub}^{4q} \frac{R_{max}^{2-4q} - R_{sub}^{2-4q}}{2 - 4q} \quad (4.26)$$

The heat capacity of the disk can be estimated from its mass and the specific heat capacity of atomic hydrogen. For hydrogen, assumed to be an ideal gas, the heat capacity is given by

$$C_H = \frac{3k}{2m_H} \approx 1.24 \times 10^8 \text{ erg/g/K} \quad (4.27)$$

The cooling timescale can be roughly estimated as

$$\tau_{cool} = \frac{C_H M_{disk} T_{disk}}{L_{disk}} \quad (4.28)$$

where  $T_{disk}$  is some average temperature of the disk used to estimate the amount of thermal energy stored in the disk; and  $M_{disk}$  is the disk mass. Calculation for a disk with parameters  $M_{disk}=0.02 M_\odot$ ,  $T_{disk}=1000$  K,  $R_{sub} = 8$  AU,  $R_{max} = 200$  AU,  $T_{sub} = 1500$  K,  $q=0.75$ , yields the cooling timescale of

$$\tau_{cool} \approx 1 \text{ day}$$

This timescale is two orders of magnitude shorter than the orbital timescale of the binary ( $P=500$  days), which shows that the asymmetry of the disk brightness cannot be produced by the thermal energy, accumulated and released by the disk on the orbital timescale.

## 4.4 Stability of the sublimation front

*This section is inspired by Evans (1994), “The dusty universe”.*

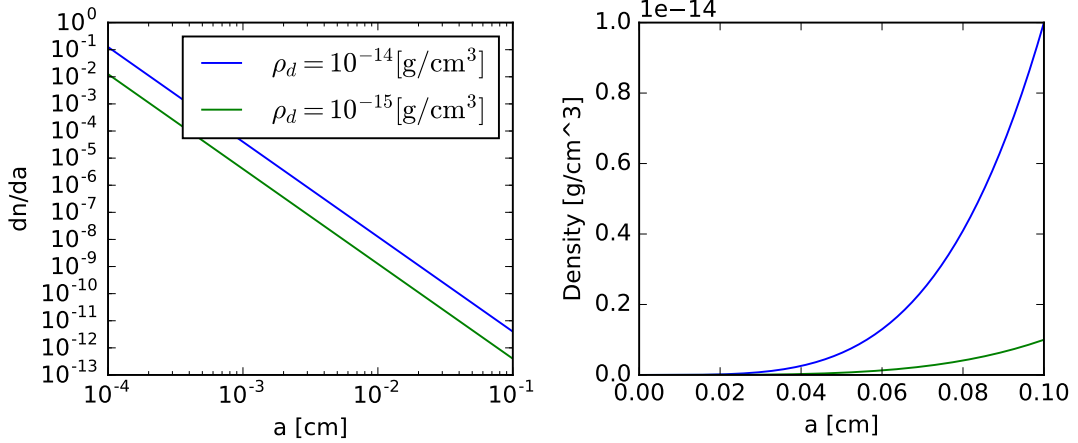


Figure 4.4: Two distributions of grain sizes with different total dust density  $\rho_d$  and maximum grain size 1 mm. *Left:* number density as a function of grain radius. The interval  $a \in [0, 1\mu\text{m}]$  is not shown because number density goes to  $\infty$  at  $a = 0$ . *Right:* cumulative density as a function of grain radius.

Table 4.2: Parameters of relevant dust materials; data from Evans (1994).

Material	$P_0$ [N/m <sup>2</sup> ]	$T_0$ [K]	$\rho$ [kg/m <sup>3</sup> ]
Graphite	$1.68 \times 10^{13}$	88880	2200
Silicate	$5.31 \times 10^{13}$	60560	3200...3500

Since the radius of the inner rim is determined by the sublimation physics, it is important to understand how fast can the sublimation front shift in response to the changing irradiation from the primary. In this section we derive equations that describe grain growth/evaporation and simulate the dynamics of the sublimation front in response to the thermal cycling induced by the orbital motion of the primary.

The size of dust grains is governed by the balance between growth and evaporation rates. The growth rate is determined by the accretion of the grain material from the gas phase via collisions:

$$\dot{a}_{acc} = \frac{m_X n_X \langle v \rangle}{4\rho} \quad (4.29)$$

The evaporation rate is determined by the vapor pressure of the condensing species, which is given by the Clausius-Clapeyron equation:

$$P_{vap}(T) = P_0 \exp(-T_0/T) \quad (4.30)$$

where  $P_0$ ,  $T_0$  are material constants; their values for graphite and silicate are given in Table 4.2. The rate of grain radius decrease due to evaporation is given by

$$\dot{a}_{evap} = \frac{P_{vap}(T)}{\rho} \left( \frac{m_X}{2\pi k T} \right)^{1/2} \quad (4.31)$$

The net rate of change for the grain radius is

$$\dot{a} = \dot{a}_{acc} - \dot{a}_{evap} \quad (4.32)$$

The grain size distribution is described by a power law function of the grain radius  $a$ :

$$dn = A_0 \left( \frac{a}{a_{\max}} \right)^{-p} da \quad (4.33)$$

where  $0 < a < a_{\max}$ ,  $p \approx 3.5$  (Mathis et al, 1977) and  $A_0$  is a scaling constant that depends on the total density of the material in the dust. In order to find the expression for the total density, consider a discrete distribution of grain sizes with  $k$  populations of grains, so that the total density is the sum of contributions from each of the populations:

$$\rho_d = \frac{4}{3}\pi a_1^3 \rho n_1 + \frac{4}{3}\pi a_2^3 \rho n_2 + \dots + \frac{4}{3}\pi a_k^3 \rho n_k \quad (4.34)$$

In the limit  $k \rightarrow \infty$  the density differential becomes

$$d\rho_d = \frac{4}{3}\pi a^3 \rho dn = \frac{4}{3}\pi a^3 \rho A_0 \left( \frac{a}{a_{\max}} \right)^{-p} da \quad (4.35)$$

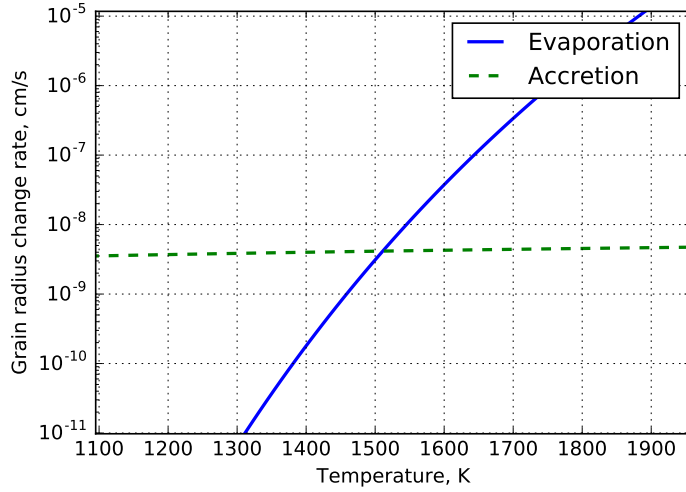


Figure 4.5: Accretion and evaporation rates as a function of temperature.

which can be easily integrated:

$$\rho_d = \frac{4}{3}\pi\rho A_0 a_{\max}^p \int_0^{a_{\max}} a^{3-p} da = \frac{4}{3}\pi\rho A_0 \frac{a_{\max}^4}{4-p} \quad (4.36)$$

The scaling constant  $A_0$  is then given by

$$A_0 = \left. \frac{3}{4} \frac{\rho_d}{\rho} \frac{4-p}{\pi a_{\max}^4} \right|_{t=0} \quad (4.37)$$

Let the density of the refractory elements in the gas phase be  $\rho_X$ . The total volumetric density  $\bar{\rho}_X$  of refractory elements is the sum of the material in the gas phase and in the solid phase:

$$\bar{\rho}_X = \rho_X + \rho_d \quad (4.38)$$

The gas phase density of the refractory elements is

$$\rho_X = \bar{\rho}_X - \frac{4}{3}\pi\rho A_0 \frac{a_{\max}^4}{4-p} \quad (4.39)$$

The equation for the maximum grain radius can therefore be written as

$$\dot{a}_{\max} = \frac{\bar{\rho}_X \langle v \rangle}{4\rho} - \frac{\pi}{3} A_0 \frac{a_{\max}^4}{4-p} \langle v \rangle - \dot{a}_{evap} \quad (4.40)$$

Note that the evaporation rate  $\dot{a}_{evap}$  does not depend on either  $a_{\max}$  or  $\rho_X$ . The equilibrium grain radius for a given temperature and total density can be found

from  $\dot{a}_{\max} = 0$ , which gives:

$$a_{\max,eq}^4 = (4 - p) \frac{3}{\pi A_0} \left( \frac{\bar{\rho}_X}{4\rho} - \frac{\dot{a}_{evap}}{\langle v \rangle} \right) \quad (4.41)$$

In order to study the behavior of the sublimation front in response to the thermal cycling, induced by the motion of the primary, we solve Eq.(4.40) for the maximum grain size on a one-dimensional radial grid extending from 4 AU to 10 AU and the number of grid points 300. The times step is fixed to 1 day. At the beginning of the simulation we set the uniform distribution of  $a_{\max}(r) = 1$  mm. After every time step, we recalculate the position of the primary by solving Kepler equation numerically, calculate  $\dot{a}_{\max}(r)$  for every grid point and update  $a_{\max}(r)$ . The temperature is calculated based on thermal equilibrium with the primary, without taking into account self-shielding of the dust; this represents a worst-case scenario, since self-shielding can only slow down the response of the sublimation front. We do the iterations for 26 orbits and plot  $a_{\max}(r)$  for selected epochs. During the first few orbits the sublimation front quickly propagates outwards (Figure 4.7), as the grains close to the primary evaporate. After 20 orbits the speed of the front propagation is noticeably slower (Figure 4.8), as the average temperature drops. Plots of  $a_{\max}(r)$  with 100 days interval after the first 20 orbits show that the position of the front is virtually unchanged within one orbital period (Figure 4.8). Therefore, we can conclude that the position of the sublimation front is stable on the orbital timescale and does not shift in response to the thermal cycling induced by the primary.

## 4.5 Conclusions

Based on the calculations presented in this chapter we can formulate the following conclusions:

1. The asymmetric irradiation by the primary is able to produce the temperature difference at the opposite sides of the disk, that results in the dust emission intensity differing by a factor of at least 2.5 when the primary is at periastron, i.e. at the farthest distance from the inner rim of the disk. This is approximately equal to the observed asymmetry in the disk brightness.
2. Dust grains achieve thermal equilibrium with radiation on a timescale of  $\sim 10$  s, which is negligible compared to the orbital timescale.
3. Cooling of the dust by gas via collisional heat transfer is negligible and cannot shift the temperature of the grains away from the point of equilibrium with the radiation.

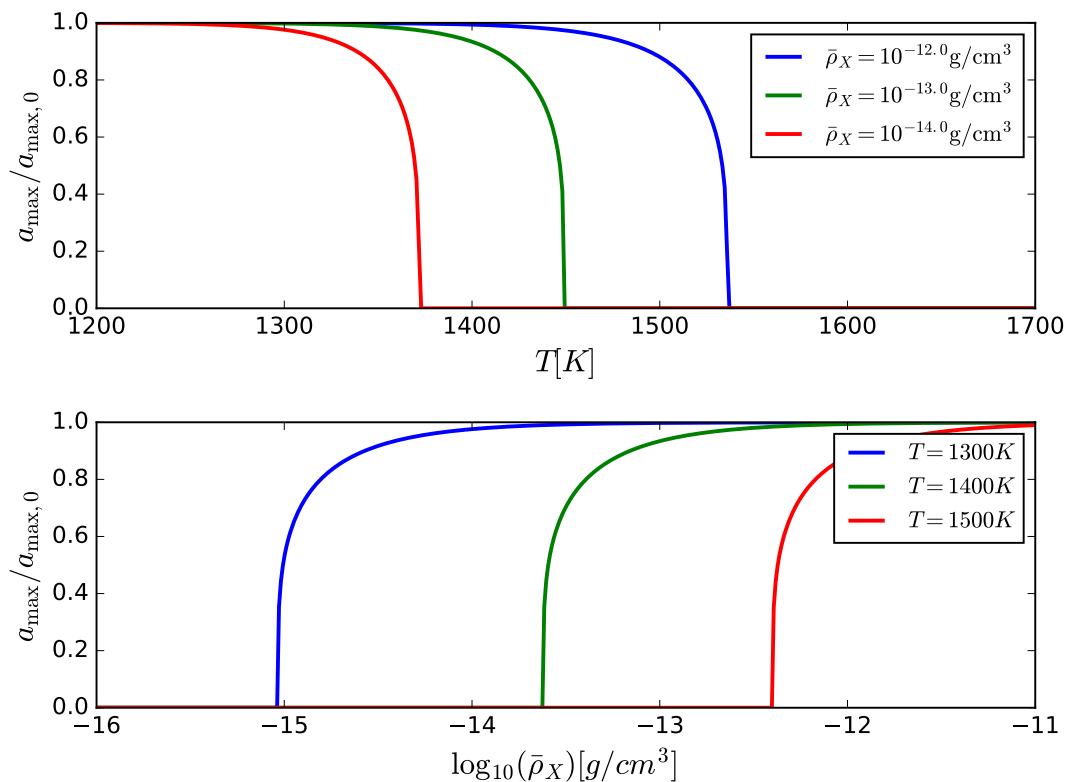


Figure 4.6: Equilibrium size of grains as a fraction of initial size, depending on temperature and density of refractory elements.

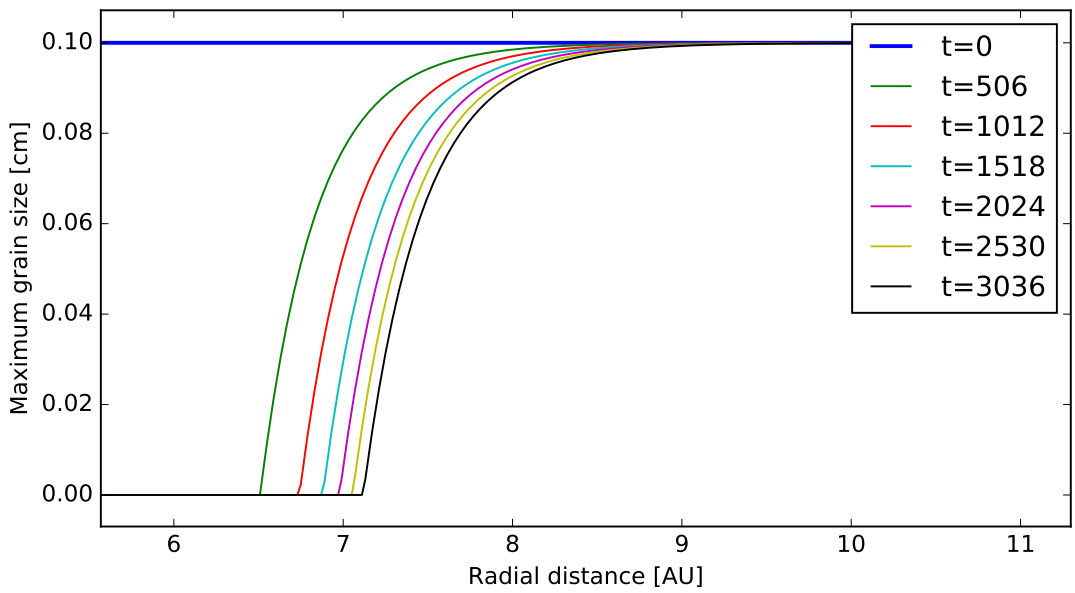


Figure 4.7: Dynamics of the sublimation front starting with homogeneous dust density distribution at  $t = 0$ , calculated for the first 6 orbits of the primary ( $P=506$  days). The time is in days.

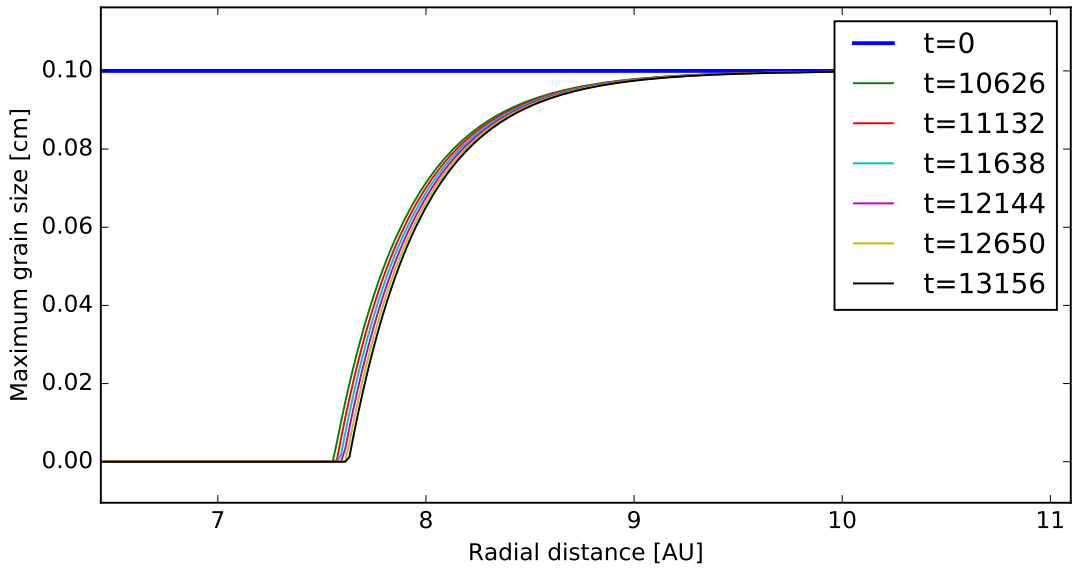


Figure 4.8: Dynamics of the sublimation front after the first 20 orbits, for 6 orbits afterwards.

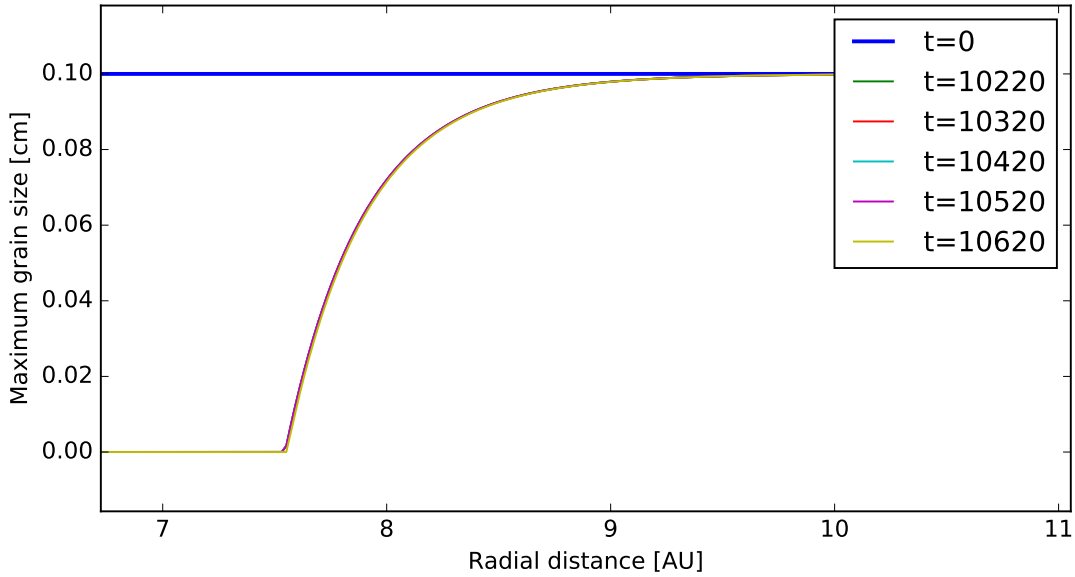


Figure 4.9: Dynamics of the sublimation front after the first 20 orbits, for 5 time intervals during a single orbit of the primary ( $P=500$  days). All the plots except for  $t = 0$  are indistinguishable.

4. The disk can radiate away its thermal energy on a timescale of  $\sim 1$  day, which shows that heat cannot be accumulated and released by the disk on the orbital timescale. Therefore, any observed asymmetry of the disk brightness must be a result of the thermal equilibrium with the radiation from the primary.
5. The position of the inner rim, which is determined by the dust sublimation physics, is stable against the variations in temperature induced by the primary.

The above conclusions allow us to proceed with modeling the thermal structure of the disk in a static setting, without considering the dynamics of heat transfer on the orbital timescale. The last conclusion shows that the inner rim of the disk can also be considered static, and fixed at the position determined by the dust sublimation temperature.

# Chapter 5

## Modeling the radiative transfer in the disk

In this chapter we construct a model of the dusty disk around V390 Vel, with the aim to simulate propagation of radiation inside the disk and render synthetic images of the disk. The model includes three components: disk density structure, position of the primary in the orbit, and the radiative transfer algorithm. The primary is the only light source in the model; it is located off-center relative to the center of mass of the disk, due to the fact that it is a part of a binary. The density structure is a set of equations that describe the dust density distribution inside the disk. We consider two density models: a centrally symmetric density structure, and a structure with spiral density waves. The density structure determines optical depths along different paths inside the disk.

### 5.1 Disk structure

We model the disk structure in cylindrical coordinate system  $(r, \phi, z)$ . The origin of the coordinate system coincides with the barycenter of the binary, and the midplane of the disk is aligned with the binary orbital plane. The disk structure is defined by the dust density distribution. For an axially symmetric disk, the dust density is modeled as a product of the radial and vertical density distributions:

$$\rho_{symm}(r, \phi, z) = \rho_r(r)\rho_v(z) \quad (5.1)$$

In case of a disk with a spiral density enhancement, an additional factor describing the geometry of the spiral waves is present:

$$\rho_{spiral}(r, \phi, z) = \rho_s(r, \phi)\rho_r(r)\rho_v(z) \quad (5.2)$$

In the rest of this section, each component of the disk structure is described in details.

### 5.1.1 Vertical structure

*This section is based on the lecture notes of Prof. Alex De Koter, “Formation of stars and planetary systems”, Chapter 9: “Properties of circumstellar disks”.*

The vertical disk structure is determined by the balance between the vertical component of the gravitational acceleration and the vertical pressure gradient:

$$\frac{1}{\rho} \frac{\partial P}{\partial z} + \frac{GM}{r^2 + z^2} \sin \theta = 0 \quad (5.3)$$

In thin disk approximation, where  $z \ll r$ :

$$\frac{1}{\rho} \frac{\partial P}{\partial z} + \frac{GM}{r^3} z = 0 \quad (5.4)$$

In order to obtain an analytical solution, a further simplifying assumption of vertically isothermal structure is needed, in which case the pressure gradient is a function of the density gradient:

$$\frac{\partial P}{\partial z} = \frac{k}{\mu m_p} T \frac{\partial \rho}{\partial z} \quad (5.5)$$

so that the vertical balance equation is written as

$$\frac{GM}{r^3} z dz + \frac{k}{\mu m_p} T \frac{d\rho}{\rho} = 0 \quad (5.6)$$

or

$$\frac{d\rho}{\rho} = -\frac{z dz}{H^2} \quad (5.7)$$

Here  $H$  is the scale height of the disk, which can be expressed in terms of the sound speed

$$c_s^2 = \frac{kT}{\mu m_p} \quad (5.8)$$

and Keplerian angular velocity

$$\Omega_K^2 = \frac{GM}{r^3} \quad (5.9)$$

as

$$H(r) = \frac{c_s}{\Omega_K} = \sqrt{\frac{kT}{\mu m_p}} \sqrt{\frac{r^3}{GM_*}} \quad (5.10)$$

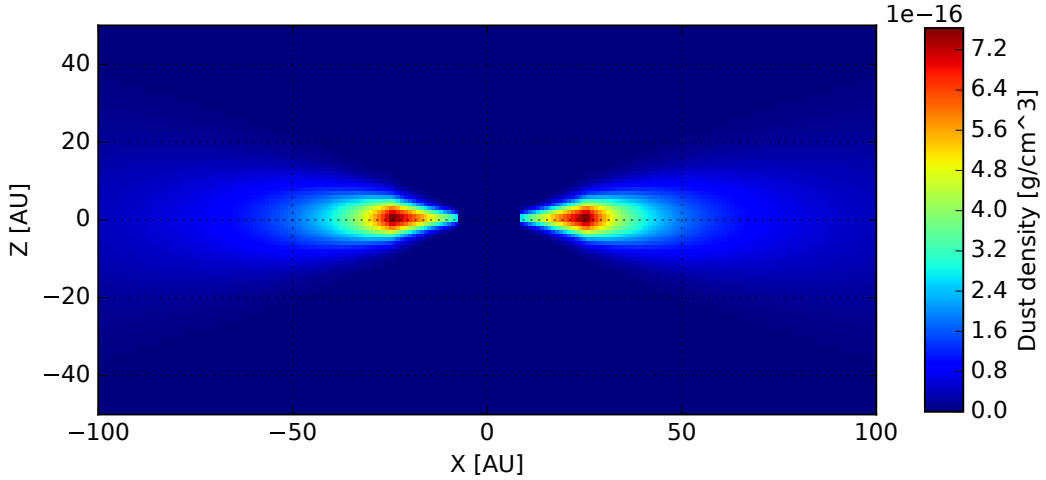


Figure 5.1: Model dust density distribution inside the disk. A cross-section through the axis of symmetry (rotation axis).

For the temperature we adopt a power-law distribution, following Kluska et al (2012):

$$T_{approx}(r) = T_{sub} \left( \frac{R_{sub}}{r} \right)^{0.75} \quad (5.11)$$

where  $T_{sub} = 1100$  K is the temperature at the sublimation rim (based on calculations of temperature in Table 4.1);  $R_{sub}$  is the radius of the sublimation rim. This temperature distribution is only used to calculate the scale height when initializing the disk structure. Later, when we do the radiative transfer, the temperature distribution is recalculated based on the radiative heating from the primary.

The vertical structure equation (5.7) can now be integrated to yield

$$\rho_v(z) = \rho_0 \exp \left( -\frac{z^2}{2H^2} \right) \quad (5.12)$$

Here  $\rho_0$  is the midplane density, which is given by

$$\rho_0 = \frac{\Sigma}{\sqrt{2\pi}H} \quad (5.13)$$

where  $\Sigma$  is the surface density of the disk [ $\text{g}/\text{cm}^2$ ], defined in the next section.

### 5.1.2 Radial structure

The radial structure of the disk is modeled following Kluska et al (2018) as a double power law for the surface density:

$$\Sigma(r) = \begin{cases} \Sigma_{\max} \left( \frac{r}{R_{mid}} \right)^{p_1}, & r < R_{mid} \\ \Sigma_{\max} \left( \frac{R_{mid}}{r} \right)^{p_2}, & R_{mid} < r < R_{\max} \end{cases} \quad (5.14)$$

For the power constants we adopt values  $p_1 = 2$  and  $p_2 = 1$ . The  $\Sigma_{\max}$  parameter is the surface density at the point where the density reaches a maximum, which occurs at the radial distance  $R_{mid}$ . The parameters  $\Sigma_{\max}$  determines the total mass of dust in the disk. It is therefore important to set it so that the mass is equal to an empirical value, derived from observations. Bujarrabal et al (2018) determined the mass of matter (gas and dust) around V390 Vel to be  $0.02M_{\odot}$ . To find the total mass for our disk structure, we need to integrate the structure equation along the radial coordinate. The mass differential is given by:

$$dm = 2\pi r \Sigma(r) dr \quad (5.15)$$

Mass of the inner part of the disk:

$$M_{in} = \int_0^{R_{mid}} \Sigma_{\max} \left( \frac{r}{R_{mid}} \right)^{p_1} 2\pi r dr = 2\pi \Sigma_{\max} \frac{R_{mid}^2}{p_1 + 2} \quad (5.16)$$

Mass of the outer part of the disk:

$$M_{out} = \int_{R_{mid}}^{R_{\max}} \Sigma_{\max} \left( \frac{R_{mid}}{r} \right)^{p_2} 2\pi r dr = 2\pi \Sigma_{\max} \frac{R_{mid}^{p_2}}{2 - p_2} (R_{\max}^{2-p_2} - R_{mid}^{2-p_2}) \quad (5.17)$$

The total mass of the disk:

$$M = M_{in} + M_{out} = 2\pi \Sigma_{\max} \left[ \frac{R_{mid}^2}{p_1 + 2} + \frac{R_{mid}^{p_2}}{2 - p_2} (R_{\max}^{2-p_2} - R_{mid}^{2-p_2}) \right] \quad (5.18)$$

For  $p_1 = 2$  and  $p_2 = 1$ :

$$M = 2\pi \Sigma_{\max} (R_{mid} R_{\max} - 3R_{mid}^2/4) \quad (5.19)$$

The expression for the  $\Sigma_{\max}$  parameter is therefore:

$$\Sigma_{\max} = \frac{M_{disk}}{2\pi (R_{mid} R_{\max} - 3R_{mid}^2/4)} \quad (5.20)$$

For the adopted disk parameters  $R_{mid} = 25\text{AU}$ ,  $R_{\max} = 200\text{AU}$ , we get  $\Sigma_{\max} = 6.2 \text{ g/cm}^2$ .

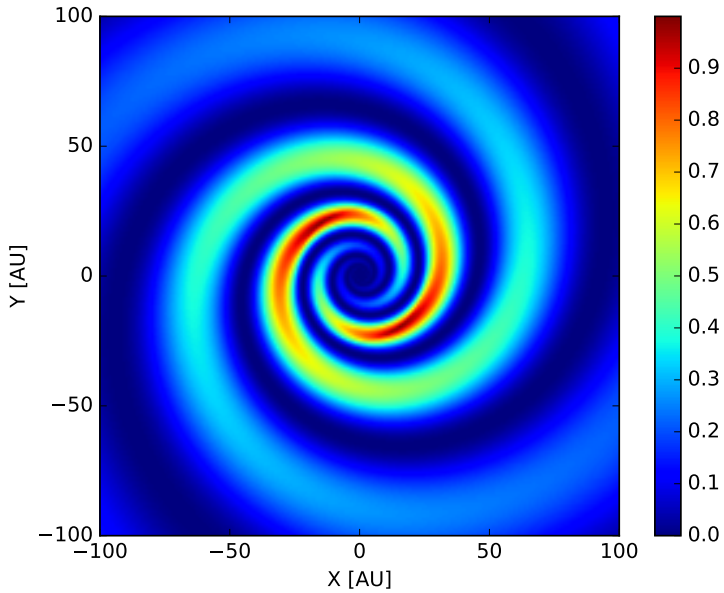


Figure 5.2: Spiral density model, normalized to unity. Cross-section through the midplane of the disk.

The dust is assumed to constitute a fixed fraction of gas  $\xi = 0.01$ . The radius of the dust sublimation rim is set to  $R_{sub} = 8.25$  AU, as determined by Kluska et al (2018). Within this radius, the dust is assumed to be completely evaporated. The expression for the dust density structure is therefore given by:

$$\rho_{dust}(r, z) = \begin{cases} \xi \frac{\Sigma(r)}{\sqrt{2\pi}H} \exp[-0.5(z/H)^2], & r > R_{sub} \\ 0, & r < R_{sub} \end{cases} \quad (5.21)$$

This dust density distribution is shown in Figure 5.1.

### 5.1.3 Spiral density waves

The spiral density waves in the disk are modeled following Homan et al (2016), as a geometrical model of density enhancement, described by the following equation:

$$\rho_{gas}(r, \phi, z) = \frac{1}{2} [\sin(2\phi + k_w \log_{10}(r)) + 1] \frac{\Sigma(r)}{\sqrt{2\pi}H} \exp[-0.5(z/H)^2] \quad (5.22)$$

The factor  $k_w$  determines the winding density of the spiral. We find that  $k_w = 20$  produces a structure most resembling a typical spiral pattern around AGB systems (see e.g. Ramstedt et al, 2014). The spiral density pattern according to this model is shown in Figure 5.2.

## 5.2 Position of the primary

*This section is based on Hilditch (2001), “An introduction to close binary stars”.*

The position of the primary in the orbit is calculated as follows. First, the Kepler equation is solved numerically to obtain the eccentric anomaly  $E$ :

$$E - e \sin(E) = 2\pi(t - T_0)/P \quad (5.23)$$

where  $e$  is the eccentricity,  $P$  is the orbital period and  $T_0$  is the time of periastron passage (see Table 2.1). The eccentric anomaly is used to calculate the true anomaly  $\theta$ :

$$\tan(\theta/2) = \sqrt{\frac{1+e}{1-e}} \tan(E/2) \quad (5.24)$$

The true anomaly gives the angular position of the primary relative to the barycenter. The radial position is calculated as follows:

$$r = \frac{A_1(1-e^2)}{1+e \cos(\theta)} \quad (5.25)$$

where  $A_1$  is the semi-major axis of the primary. The Cartesian coordinates  $(X_p, Y_p)$  of the primary in the orbital plane are calculated with the usual transformations:

$$X_p = r \cos(\theta) \quad (5.26)$$

$$Y_p = r \sin(\theta) \quad (5.27)$$

## 5.3 Radiative transfer

*This section is inspired by: lecture notes of Rob Rutten, “Radiative transfer in stellar atmospheres”; contents of the course “Stellar atmospheres and stellar winds” by Prof. Leen Decin; and Dullemond & Turolla (2000).*

### 5.3.1 Formulation of the lambda-operator

To model the propagation of radiation inside the disk, we use lambda-operator formalism. Lambda-operator class of radiative transfer methods was originally developed for stellar atmosphere modeling and later adopted to other radiative transfer problems including dusty disks. An example application to the modeling of dusty disks can be found in (Dullemond & Turolla, 2000). A lambda-operator is a functional that computes mean intensity  $J$  from the source function distribution

$S$  over the problem domain. Analytically, lambda-operator can be defined as follows:

$$\Lambda[S_\nu] = \frac{1}{4\pi} \int_{4\pi} d\Omega \int_0^\tau S_\nu(\tau') e^{\tau' - \tau} d\tau' \quad (5.28)$$

where  $\Omega$  is the solid angle and  $\tau$  is the optical depth. The problem of radiative transfer in a disk with a central source can be expressed, using lambda-operator, as follows:

$$J_\nu = \Lambda[S_\nu] + J_\nu^* \quad (5.29)$$

Here the first term on the right-hand side represents self-irradiation by the disk and the second term represents irradiation by the central source. The source function has contribution from the emission as well as scattering, which is expressed as:

$$S_\nu = (1 - \varepsilon)J_\nu + \varepsilon B_\nu \quad (5.30)$$

where  $B_\nu$  is the Planck function. Here  $\varepsilon$  is the photon destruction probability, given by:

$$\varepsilon = \frac{\kappa_s}{\kappa_s + \kappa_a} \quad (5.31)$$

where  $\kappa_s$  and  $\kappa_a$  are the scattering and absorption mass attenuation coefficients, respectively. Equation (5.30) provides a closure condition that can be used to eliminate  $J_\nu$  in Eq.(5.29):

$$[1 - (1 - \varepsilon)\Lambda]S_\nu = (1 - \varepsilon)J_\nu^* + \varepsilon B_\nu \quad (5.32)$$

In order to solve this equation we discretise the problem and the lambda-operator on a cylindrical grid, so that the source function distribution is described by a vector  $\mathbf{S}$ , where each element of the vector gives the value of the source function at a node in the grid. Equation (5.32) then translates into a system of linear equations:

$$[\mathbf{I} - (1 - \varepsilon)\Lambda_\nu]\mathbf{S}_\nu = (1 - \varepsilon)\mathbf{J}_\nu^* + \varepsilon\mathbf{B}_\nu \quad (5.33)$$

where  $\mathbf{I}$  is the identity matrix (not to be confused with intensity) and  $\Lambda_\nu$  is the discrete version of the lambda operator, usually called lambda-matrix. Traditionally, this equation is solved using lambda-iteration and accelerated lambda-iteration class of methods (ALI), which yield an approximate solution. The reason for this is the computational costs associated with inverting the matrix on the left-hand side. However, we find that for a not too large grid ( $\sim 10^4$  nodes) and with the use of sparse matrix representation, the linear system of equations (5.33) can be solved directly. Most of the computational costs is associated with the construction of the lambda-matrix itself, rather than with solving the system (5.33).

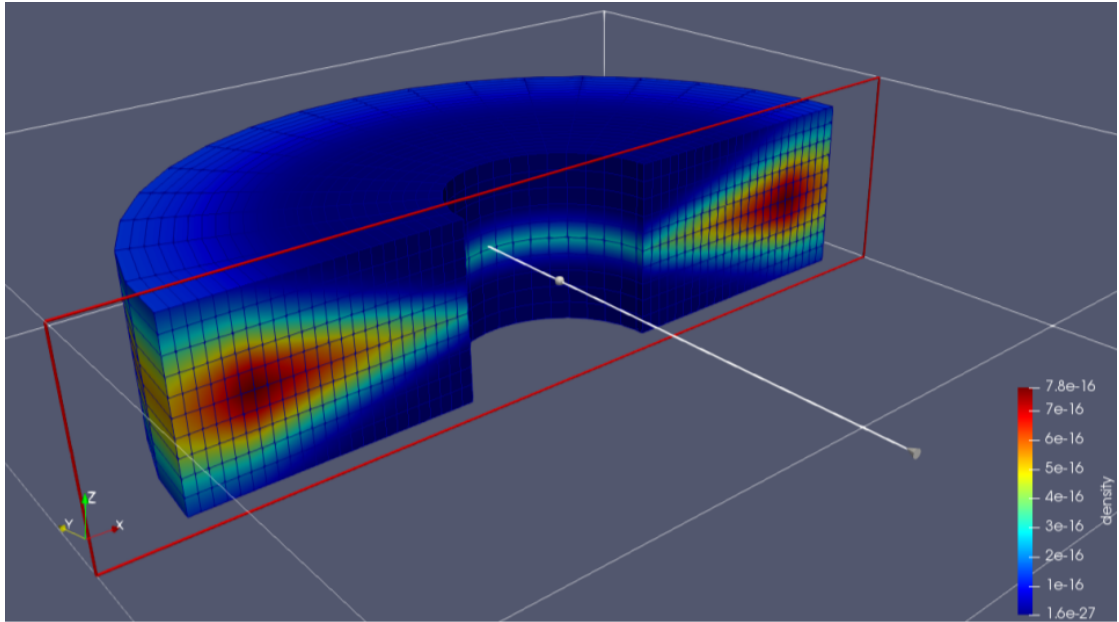


Figure 5.3: The cylindrical grid used for the radiative transfer problem. The color shows the dust density in g/cm<sup>3</sup>.

### 5.3.2 Computation grid and the interpolation of the source function

We do the calculations on a cylindrical grid (Figure 5.3) with linear spacing along all three coordinates (radial  $r$ , axial  $z$  and azimuthal  $\phi$ ). Linear spacing along the radial coordinate was chosen instead of more conventional logarithmic spacing, in order to simplify interpolation. The source function is interpolated using second order polynomials using the values of a central node and the six adjacent nodes, as follows:

$$S(r, \phi, z) = b_0 + b_r r + b_\phi \phi + b_z z + b_{rr} r^2 + b_{\phi\phi} \phi^2 + b_{zz} z^2 \quad (5.34)$$

where  $r$ ,  $\phi$  and  $z$  are local coordinates defined on  $[-1, 1]$  interval each. The values of the source function at the nodes are:

$$S_0 = S(0, 0, 0) \quad (5.35)$$

$$S_{r-} = S(-1, 0, 0) \quad (5.36)$$

$$S_{r+} = S(1, 0, 0) \quad (5.37)$$

$$S_{\phi-} = S(0, -1, 0) \quad (5.38)$$

$$S_{\phi+} = S(0, 1, 0) \quad (5.39)$$

$$S_{z-} = S(0, 0, -1) \quad (5.40)$$

$$S_{z+} = S(0, 0, 1) \quad (5.41)$$

where  $S_0$  is the value at a central node and  $S_{r-}, S_{r+}, S_{\phi-}, S_{\phi+}, S_{z-}, S_{z+}$  are the values at the adjacent nodes. The interpolated source function can then be expressed as:

$$\begin{aligned} S(r, \phi, z) &= S_0(1 - r^2 - \phi^2 - z^2) + \frac{1}{2}S_{r+}(r^2 + r) + \frac{1}{2}S_{r-}(r^2 - r) \\ &\quad + \frac{1}{2}S_{\phi+}(\phi^2 + \phi) + \frac{1}{2}S_{\phi-}(\phi^2 - \phi) + \frac{1}{2}S_{z+}(z^2 + z) + \frac{1}{2}S_{z-}(z^2 - z) \end{aligned} \quad (5.42)$$

In addition to the spatial grid, a direction grid is also required, in order to perform integration over the full solid angle in Eq.(5.28). The direction grid is a set of unit vectors representing directions of rays, and is constructed to achieve approximately uniform coverage of the full  $4\pi$  solid angle. The grid is defined by a single parameter  $\alpha$ , which represents spacing of the angles along both polar and azimuthal coordinates in a spherical coordinate system. The number of intervals along the polar coordinate is  $n_\theta = \lceil \pi/\alpha \rceil$  and along the azimuthal coordinate is  $n_\phi(\theta) = \lceil \sin(\theta)/\alpha \rceil + 1$ , so that the azimuthal spacing remains approximately constant when approaching the poles of the spherical coordinate system (at  $\theta = 0, \pi$ ).

### 5.3.3 Construction of the lambda-matrix

The lambda-matrix is constructed row by row; each row of the lambda-matrix allows calculating mean intensity at a node corresponding to the position of the row in the matrix based on the source function values everywhere in the disk. For each direction in the orientation grid, a ray is propagated from the node up to the maximum optical depth  $\tau_{\max}$ . The ray is propagated in equal increments of the optical depth  $\Delta\tau$ , which means that in general the physical lengths of the ray segments are different. The propagation uses a predictor-corrector algorithm to achieve equal steps in optical depth. First, an initial estimate of the increment is calculated as

$$\Delta s_1 = \frac{\Delta\tau}{\kappa_\nu \rho_0} \quad (5.43)$$

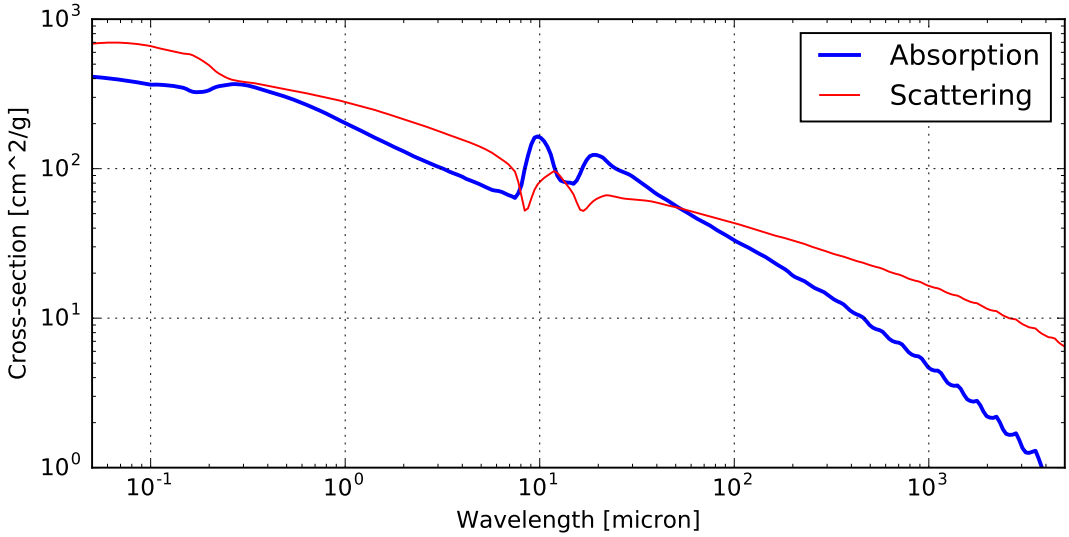


Figure 5.4: Dust opacity for absorption and scattering as a function of wavelength. Data from the DIANA project (Woitke et al, 2016).

where  $\kappa_\nu$  and  $\rho_0$  are the dust mass absorption coefficient and density at the initial position respectively. After that, the dust density  $\rho_1$  at the position of the initial increment is found and the corrected increment is calculated as

$$\Delta s_2 = \frac{2\Delta\tau}{\kappa_\nu(\rho_0 + \rho_1)} \quad (5.44)$$

This process is repeated until the optical depth  $\tau_{\max}$  is reached. After every increment, a check is performed on whether the last point went outside the grid, in which case the propagation of the ray is stopped. This procedure yields a set of points inside the grid, along a ray and with equal spacing in terms of the optical depth. We refer to this set of points as optical depth grid.

An element of the lambda-matrix is calculated as a sum of the coefficients for the interpolated source function, given by Eq.(5.42), over the elements of the direction grid  $\{\Omega\}$  and the optical depth grid  $\{\tau\}$ :

$$\Lambda_{i,j} = \sum_{\{\Omega\}} \sum_{\{\tau\}} C_j \exp(-\tau_{i,j}) \quad (5.45)$$

where  $C_j$  is the source function at node  $j$  and  $\tau_{i,j}$  is the optical depth between nodes  $i$  and  $j$ .

### 5.3.4 Temperature structure

Before the equation (5.33) can be solved, it is necessary to find the temperature distribution in the disk, which determines the  $\varepsilon\mathbf{B}_\nu$  term. We find the temperature through the following iterative process (see Figure 5.5). We start with zero source function  $\mathbf{S}_\nu^{(0)} = 0$  (the superscript labels the iteration number), so that the mean intensity is only coming from the central source,  $\mathbf{J}_\nu^{(1)} = \mathbf{J}_\nu^*$ . From the mean intensity we find the source function based on the radiative equilibrium condition:

$$\int_0^\infty S_\nu^{(1)} \kappa_\nu d\nu = \int_0^\infty J_\nu^{(1)} \kappa_\nu d\nu \quad (5.46)$$

where  $\kappa_\nu$  is the dust opacity; we use opacity data from the DIANA project (Woitke et al, 2016). The dust opacities (for the absorption and scattering) as a function of wavelength are shown in Figure 5.4. The equation (5.46) is solved numerically, by pre-computing the left-hand side for a range of temperatures ( $S_\nu = B_\nu(T)$ ) from 10 K to  $10^4$  K. After the right-hand side is calculated, the temperature is found by searching numerically for the temperature value corresponding to the value of the integral and linearly interpolating between the pre-computed points. A new value of the mean intensity is then calculated using the lambda-matrix:

$$\mathbf{J}_\nu^{(2)} = \mathbf{\Lambda}_\nu \mathbf{S}_\nu^{(1)} + \mathbf{J}_\nu^* \quad (5.47)$$

This procedure is repeated until convergence of the temperature is achieved. Usually it requires no more than 15 iterations to achieve convergence, after which the temperature does not change anymore up to the precision of the floating point. After the  $\varepsilon\mathbf{B}_\nu$  term is found, the system of linear equations (5.33) is solved directly, yielding the source function values  $\mathbf{S}_\nu$  at the nodes of the grid.

### 5.3.5 Synthetic images

Synthetic images of the disk are computed by considering a virtual detector, defined by the dimensions in pixels, field of view (in mas) and distance to the system (in kpc). Based on these parameters, the physical scale of a pixel is calculated. The detector is projected onto the sky so that each pixel has physical coordinates  $P=(x_{sky}, y_{sky}, 0)$ . Each pixel represents a line of sight with the starting point at  $P$  and the direction vector  $D=(0,0,-1)$ , i.e. the observer is looking at the disk from the positive z direction. The observed intensity is calculated through the following four steps:

1. The line of sight vector is transformed from the coordinate system of the sky into the coordinate system of the binary orbit, in which the disk is also defined.

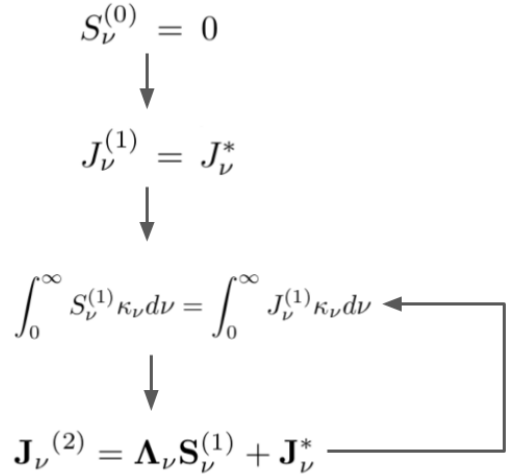


Figure 5.5: Iterative procedure for finding the temperature distribution inside the disk.

2. Intersection points of the transformed line of sight vector with the surface of the grid are calculated and a point is selected as the entry point into the model domain.
3. Starting from the entry point, a ray is propagated along the line of sight until a specified optical depth is reached (we used  $\tau_{\max} = 2.0$ ) or the ray reaches the exit point; the propagation is done using the algorithm described in § 5.3.3.
4. The emerging intensity is calculated by numerically integrating the radiative transfer equation along the ray.

The disk is defined in the coordinate system of the binary orbit. Orientation of an orbit in space is specified by the three angles: inclination ( $i$ ), longitude of the ascending node (LAN) and the argument of periastron ( $\omega$ ). Transformation of a vector from the coordinate system of the sky into the coordinate system of the binary is performed using the following rotation matrix:

$$M_R = \begin{bmatrix} c_1c_3 - c_2s_1s_3 & -c_1s_3 - c_2c_3s_1 & s_1s_2 \\ c_3s_1 + c_1c_2s_3 & c_1c_2c_3 - s_1s_3 & -c_1s_2 \\ s_2s_3 & c_3s_2 & c_2 \end{bmatrix} \quad (5.48)$$

where  $c_1 = \cos(\text{LAN})$ ,  $c_2 = \cos(i)$ ,  $c_3 = \cos(\omega)$ ,  $s_1 = \sin(\text{LAN})$ ,  $s_2 = \sin(i)$ ,  $s_3 = \sin(\omega)$ .

Intersection points of the line of sight with the grid are found by representing the grid surface with four analytical surfaces: inner and outer cylinders, top and bottom planes. Line-cylinder intersection points are found by solving a quadratic equation

$$At^2 + Bt + C = 0 \quad (5.49)$$

with the coefficients

$$A = D_x^2 + D_y^2 \quad (5.50)$$

$$B = 2(P_x D_x + P_y D_y) \quad (5.51)$$

$$C = P_x^2 + P_y^2 - R^2 \quad (5.52)$$

where  $P$ ,  $D$  are the vectors defining the line of sight in the coordinate system of the grid,  $R$  is the cylinder radius. If the quadratic equation has solutions  $(t_1, t_2)$ , then an intersection point  $Q$  is found as  $Q = P + Dt$ . An intersection point with a plane orthogonal to the  $z$  axis is found as

$$t = (Z_p - P_z)/D_z \quad (5.53)$$

where  $Z_p$  is the  $z$ -coordinate of the plane.

The intensity  $I$ , emerging along a line of sight is found by numerically integrating the source function  $S$ :

$$I = \int_0^\tau S(\tau') \exp(\tau' - \tau) d\tau' \quad (5.54)$$

## 5.4 Results

The radiative transfer calculations were performed on a cylindrical grid with a radial extent [8.25 AU, 30 AU] and a vertical extent [-7 AU, 7 AU]. The outer radial limit of 30 AU was chosen so that to reduce computational costs and make the problem tractable while maintaining a sufficient grid resolution at the inner edge of the disk, which is of the most interest. The number of grid nodes were: 25 along the radial coordinate, 36 along the azimuthal coordinate and 11 along the vertical coordinate. The total number of nodes in the grid is 9900. The direction grid was constructed with an angle increment of  $\pi/7$  and contained 48 direction vectors in total (see §5.3.2 for the details). The wavelength grid is a logarithmic grid that contains 15 points and covers a range [0.5  $\mu$ m, 50  $\mu$ m]. This wavelength grid was chosen so that the numerical error in integrating a Planck function with a temperature of 1500 K is below 0.5% compared to the exact value.

The density distribution inside the model was set up as described in §5.1, as a double-power law with a maximum surface density at a radial position of 25 AU.

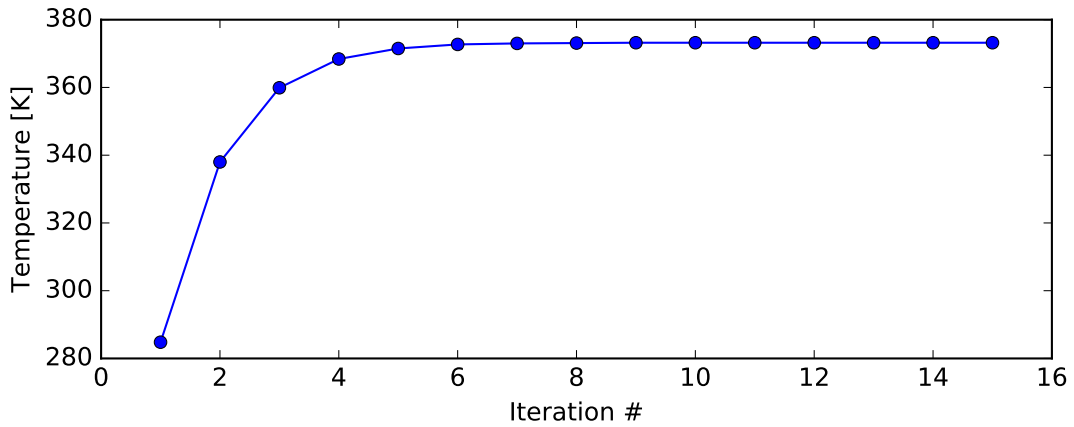


Figure 5.6: Evolution of the temperature at a node during the iterative procedure for calculating the temperature distribution in the disk. The node is located in the midplane of the disk, at a radial distance of 12.7 AU.

The lambda-matrix is constructed with  $\tau_{\max} = 2.0$  and  $\Delta\tau = 0.1$ . The temperature distribution inside the model was computed using the iterative procedure described in §5.3.4, with 15 iterations. The evolution of temperature at a selected node during the iterations is shown in Figure 5.6.

The simulated images were computed for a wavelength of 1.6  $\mu\text{m}$ , which is the average wavelength of the interferometric observations done in Kluska et al (2018).

#### 5.4.1 Symmetric disk structure

Synthetic images for the disk with a symmetric density structure (without spiral density waves) are shown in Figure 5.7. The images are for two primary orbital phases: periastron and apoastron, with two different LAN values for each phase. The intensity distributions in all the images show a thin ring of emission, which is centrally asymmetric and has a single maximum along the azimuthal direction. The maximum intensity is different and is higher where the hot side of the inner rim of the disk is viewed directly, rather than through the depth of the disk. There is no secondary intensity maximum, such as the one that is visible in the image reconstructed from interferometry (Figure 1.8).

#### 5.4.2 Disk with spiral density waves

Synthetic images for the disk with spiral density waves are shown in Figure 5.8 for the primary at periastron and in Figure 5.9 for the primary at apoastron.

Similarly to the images for the symmetric disk structure, they feature a ring of emission from the inner rim of the disk. However, for some of the combinations of the primary position and the LAN value, in addition to the primary azimuthal maximum of intensity, they show a secondary maximum. The secondary maximum is most pronounced for LAN= 90, 70 when the primary is at periastron, and for LAN= −90 when the primary is at apoastron.

## 5.5 Discussion

In our model of the disk, the vertical density structure is calculated based on the assumption of a constant temperature along the vertical coordinate, which may not hold in reality. A more accurate approach is to find the density structure through an iterative process, where the density distribution is calculated based on the temperature found from the radiative transfer, and the radiative transfer calculation is repeated with the updated density distribution. When the isothermal assumption of the vertical structure is relaxed, the equation for the hydrostatic equilibrium (5.5) becomes

$$\frac{\partial P}{\partial z} = \frac{k}{\mu m_p} \left( T \frac{\partial \rho}{\partial z} + \rho \frac{\partial T}{\partial z} \right) \quad (5.55)$$

and the equation for the density is given by

$$d \ln \rho = -\tilde{H}^2 (T z dz + d \ln T) \quad (5.56)$$

where

$$\tilde{H}^2 = \frac{GM}{r^3} \frac{\mu m_p}{k} \quad (5.57)$$

Equation (5.56) can be directly integrated to obtain an expression for the density, provided that the temperature as a function of the vertical coordinate is known.

This iterative approach has to be applied with caution and the awareness of micro-scale physical processes in the disk. The vertical density structure is determined by the gas pressure, which depends on the temperature of the gas, heated by the central source. However, the gas is coupled to the radiation not directly, but through the dust, which transfers heat to the gas via collisions of gas atoms with dust grains. As it was shown in the previous chapter, this is an inefficient, slow process, which acts on a timescale comparable to the orbital period. Therefore, in order to properly account for the effect of gas temperature on the vertical density distribution, the simulation would have to be done in a dynamic setting, so that the heat transfer from the dust to the gas is modeled explicitly, together with the varying heating of dust due to the orbital motion of the primary.

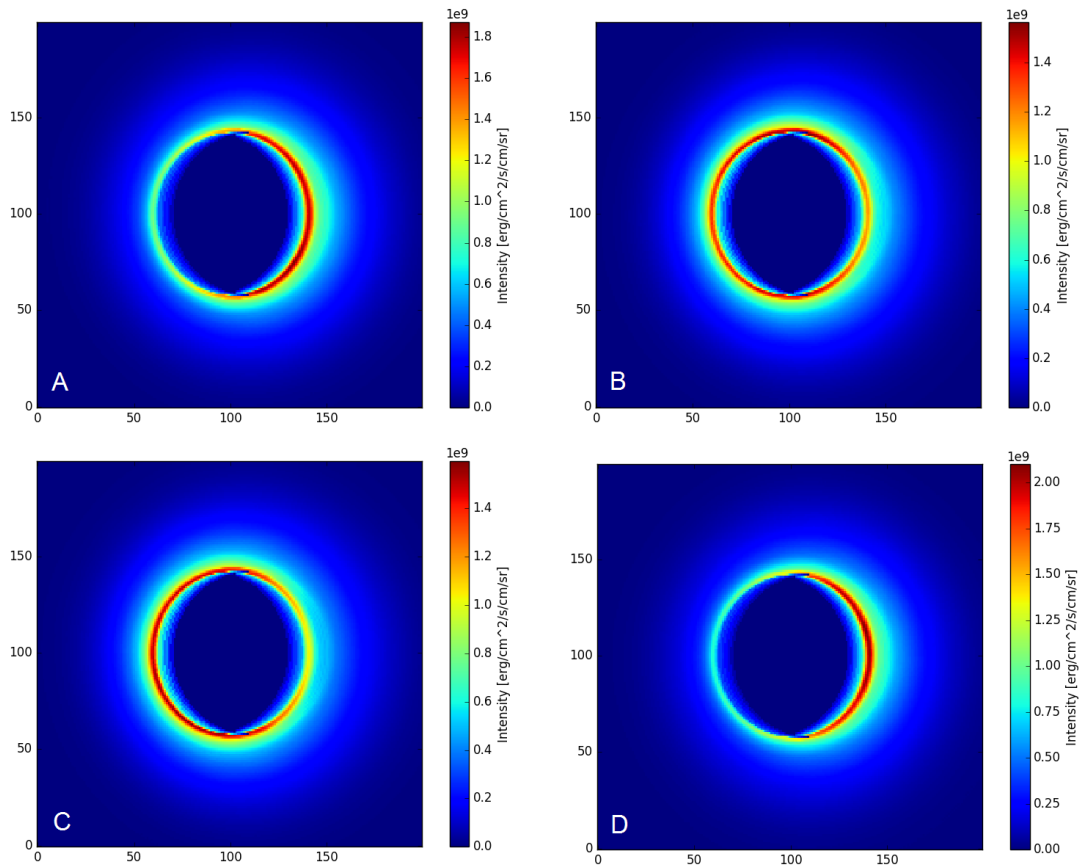


Figure 5.7: Synthetic images for an axially-symmetric disk (without spiral density waves). A: primary at periastron, LAN =  $-90^\circ$ ; B: primary at periastron, LAN =  $90^\circ$ ; C: primary at apoastron, LAN =  $-90^\circ$ ; D: primary at apoastron, LAN =  $90^\circ$ . Inclination of the disk is  $19^\circ$  in all cases.

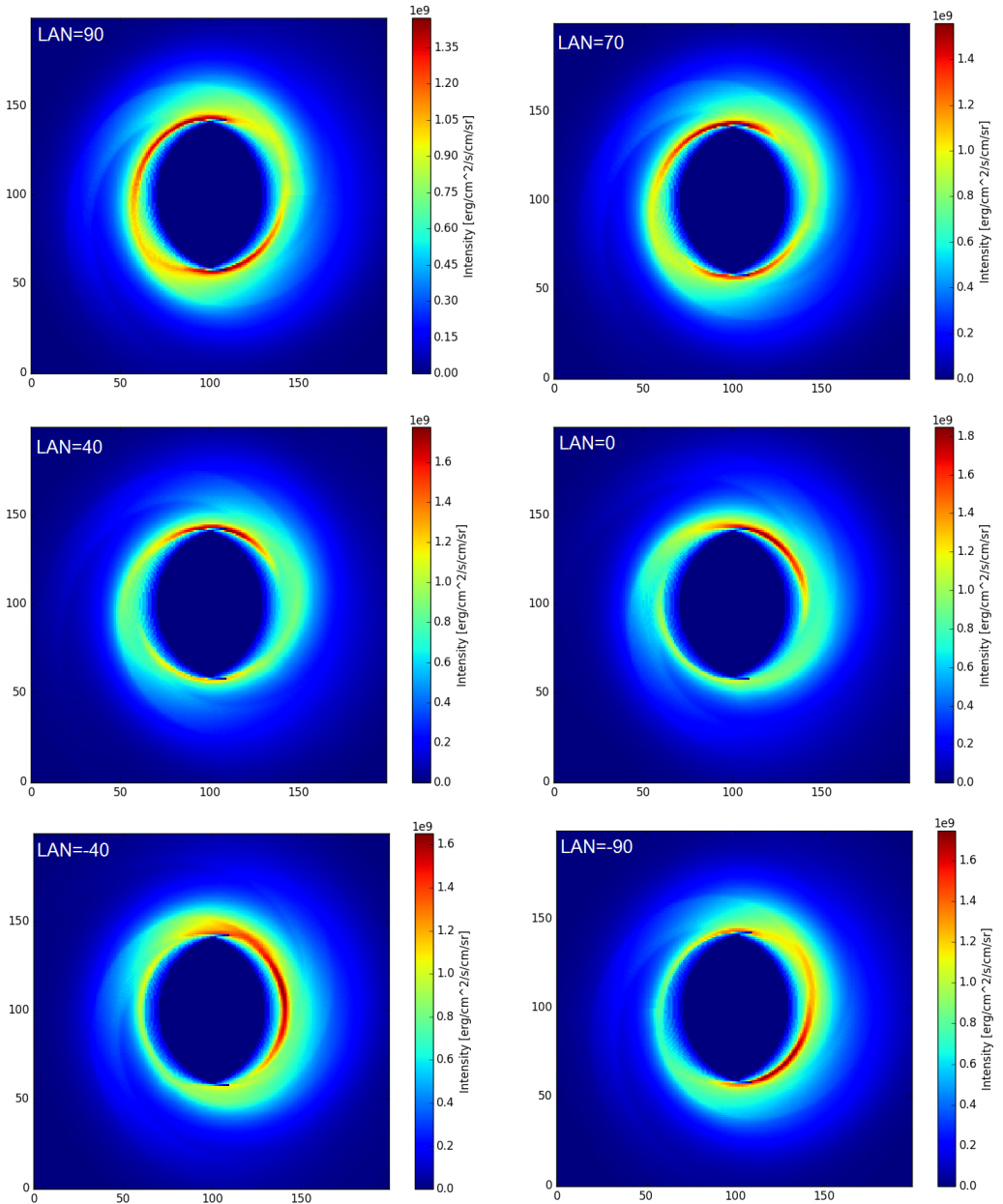


Figure 5.8: Synthetic images for a disk with spiral density waves and the position of primary at periastron. LAN (longitude of the ascending node, in degrees) is given in the top left corner of each image. Inclination of the disk: 19°.

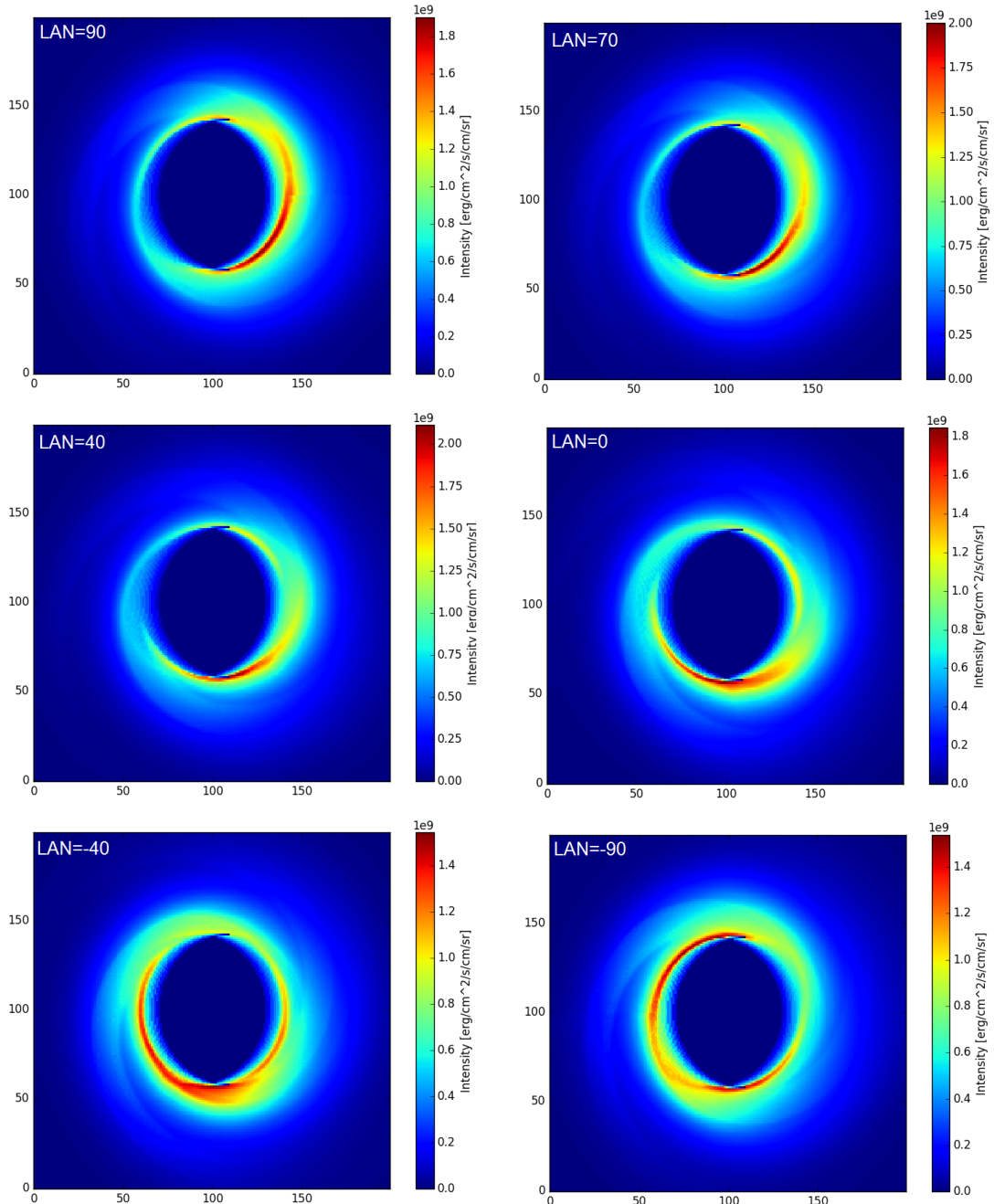


Figure 5.9: Synthetic images for a disk with spiral density waves and the position of primary at apoastrom. LAN (longitude of the ascending node, in degrees) is given in the top left corner of each image. Inclination of the disk:  $19^\circ$ .

The radial disk structure and the spiral density enhancements are represented by analytical functions that, although based on hydrodynamic simulations done in literature, are not directly connected to the physical parameters of a particular system, such as binary mass ratio or eccentricity. In chapter 3 we reconstructed the past evolution and estimated initial parameters of V390 Vel. A more physically-based approach to the modeling of the disk structure would be to perform a hydrodynamic simulation of the disk formation starting from the initial conditions, so that the present disk structure is a result of evolution, rather than a static model, not connected to the initial conditions.

Another simplification in the model is the treatment of dust grain size distribution, which is assumed to be uniform across the disk. In reality, the dust is inevitably subject to fractionation, caused by the difference in terminal velocity of grains moving relative to the gas. The ram pressure from gas is proportional to the cross-section of a grain, whereas gravitational force is proportional to its volume. As a consequence, larger grains achieve higher terminal velocities compared to smaller grains, so that with time the distribution of grain sizes becomes inhomogeneous, where larger and smaller grains are spatially segregated. One example of this process is dust settling, where the dust in the midplane of a disk consists of larger grains than the dust above the midplane, because of the vertical component of the gravitational force from the central object, which causes grains to “sink” to the midplane. Differential dust motion also occurs in the presence of radial pressure gradients, in which case the dust migrates in the direction of the pressure maximum.

Finally, our radiative transfer model assumes isotropic scattering of light by dust grains. Although, according to the DIANA data, anisotropy of scattering is relatively small, it might have some effect on the observed intensity distribution.

Nevertheless, we can argue that the simplicity of the model does not diminish its value or validity of the conclusions drawn based on it. In fact, according to the “Occam’s razor” principle, a more simple model is preferable to a more complex one, as long as the simple model reproduces all relevant properties of the object being modeled. In the case of present work, a relevant property is the azimuthal asymmetry of brightness, which is indeed reproduced by our simple model. The benefit of simplicity is that it shows more clearly what factors are responsible for the observed brightness asymmetry, i.e. asymmetric irradiation and the presence of spiral structures in the disk, which would not be that obvious if the model included numerous additional factors that could potentially play a role. At the same time, it would be erroneous to conclude that the solution we found is unique, i.e. to exclude the possibility that the observed asymmetry can be reproduced by a completely different model.

# Chapter 6

## Conclusions and future research

### 6.1 Conclusions

The results of the radiative transfer modeling of a dusty disk, similar to that around the post-AGB binary V390 Vel, showed that the observed asymmetry of the disk brightness in V390 Vel can be reproduced with a model of the disk containing spiral density waves and irradiated asymmetrically by the primary. The asymmetric irradiation by the primary, in the absence of spiral density waves, produces a single maximum in the observed azimuthal intensity of the emission from the inner rim of the disk, but it cannot reproduce the secondary maximum. Addition of the spiral density waves to the disk structure allows reproducing the secondary azimuthal intensity maximum, for certain combinations of the primary orbital phase and disk orientation in the sky coordinate system.

In the course of this study, the following conclusions were also reached, related to the micro-scale physical processes in the disk:

1. Dust grains of millimeter size or smaller achieve thermal equilibrium with radiation on a timescale that is much shorter compared to the orbital timescale.
2. Cooling of the dust by gas via collisional heat transfer is negligible and cannot shift the temperature of the grains away from the point of equilibrium with the radiation.
3. The disk can radiate away its thermal energy on a timescale of  $\sim 1$  day, which shows that heat cannot be accumulated and released by the disk on the orbital timescale. Therefore, any observed asymmetry of the disk brightness must be a result of the thermal equilibrium of the dust with the radiation from the primary.
4. The position of the inner rim, which is determined by the dust sublimation

physics, is stable against the variations in temperature induced by the orbital motion of the primary.

## 6.2 Future research

In §5.5 we discuss assumptions and simplifications that were used in the modeling of the disk, including vertical density structure and dust grain size distribution. One possible direction of the future research is to refine the model of the disk so that to improve treatment of the mentioned aspects of the model. A different and, in our opinion, more interesting approach, is to set the density structure of the disk based on hydrodynamical simulations of the disk formation. Although computationally intensive, hydrodynamical simulations of binary evolution are not intractable. In a series of papers titled “Double-Core Evolution”,<sup>1</sup> authors perform two and three-dimensional hydrodynamical simulations of the common envelope evolution of binary systems, being able to reproduce such processes as inspiral and envelope ejection. Simulations of disk formation as a result of the envelope ejection during the common envelope phase could potentially constrain some parameters of the common envelope phase, which is currently the least studied phase of binary evolution. The availability of high-resolution interferometry data for post-AGB binaries such as V390 Vel makes the inference of common envelope parameters possible through radiative transfer modeling, which connects the end state of hydrodynamical simulations with the observed structure of a disk.

As we also mention in §5.5, there may exist other models of the disk structure that could match the observations. It is therefore important to further explore the parameters space of possible disk models. V390 Vel is currently being actively studied with interferometry, with new data coming in, reflecting the disk structure in different wavelengths and at different epochs. Time-resolved interferometric data can provide a valuable information about the effect of the primary position on the observed brightness distribution. Observations in longer wavelengths allow to probe the disk structure at larger radial distances from the center. All these data can be used to further constrain the model parameters and infer more details about the disk structure.

---

<sup>1</sup>See Taam et al.(1978); Bodenheimer & Taam(1984); Taam & Bodenheimer(1989); Taam & Bodenheimer(1991); Terman et al.(1994); Taam et al.(1994); Terman et al.(1995); Yorke et al.(1995); Terman & Taam(1996); Sandquist et al.(1998).

# Bibliography

- [Abate et al.(2015)] Abate, C., Pols, O. R., Stancliffe, R. J., et al. 2015, A&A, 581, A62
- [Bodenheimer & Taam(1984)] Bodenheimer, P., & Taam, R. E. 1984, ApJ, 280, 771
- [Bondi & Hoyle(1944)] Bondi, H., & Hoyle, F. 1944, MNRAS, 104, 273
- [Bujarrabal et al.(2015)] Bujarrabal, V., Castro-Carrizo, A., Alcolea, J., & Van Winckel, H. 2015, A&A, 575, L7
- [Bujarrabal et al.(2017)] Bujarrabal, V., Castro-Carrizo, A., Alcolea, J., et al. 2017, A&A, 597, L5
- [Bujarrabal et al.(2018)] Bujarrabal, V., Castro-Carrizo, A., Winckel, H. V., et al. 2018, A&A, 614, A58
- [Casassus et al.(2015)] Casassus, S., Wright, C. M., Marino, S., et al. 2015, ApJ, 812, 126
- [Claeys et al.(2014)] Claeys, J. S. W., Pols, O. R., Izzard, R. G., Vink, J., & Verbunt, F. W. M. 2014, A&A, 563, A83
- [Clayton(1996)] Clayton, G. C. 1996, PASP, 108, 225
- [Cummings et al.(2018)] Cummings, J. D., Kalirai, J. S., Tremblay, P.-E., Ramirez-Ruiz, E., & Choi, J. 2018, ApJ, 866, 21
- [Danilovich et al.(2015)] Danilovich, T., Teyssier, D., Justtanont, K., et al. 2015, A&A, 581, A60
- [de Laverny & Mékarnia(2004)] de Laverny, P., & Mékarnia, D. 2004, A&A, 428, L13
- [de Mink et al.(2014)] de Mink, S. E., Sana, H., Langer, N., Izzard, R. G., & Schneider, F. R. N. 2014, ApJ, 782, 7

- [de Ruyter et al.(2006)] de Ruyter, S., van Winckel, H., Maas, T., et al. 2006, A&A, 448, 641
- [Dermine et al.(2013)] Dermine, T., Izzard, R. G., Jorissen, A., & Van Winckel, H. 2013, A&A, 551, A50
- [Dullemond & Penzlin(2018)] Dullemond, C. P., & Penzlin, A. B. T. 2018, A&A, 609, A50
- [Dullemond & Turolla(2000)] Dullemond, C. P., & Turolla, R. 2000, A&A, 360, 1187
- [Eddington(1941)] Eddington, A. S., Sir 1941, MNRAS, 101, 182
- [Eggleton(1983)] Eggleton, P. P. 1983, ApJ, 268, 368
- [Evans(1994)] Evans, A. 1994, The dusty universe, Chichester ; New York : J. Wiley ; Chichester : In association with Praxis Pub., Ltd., 1994.,
- [Frankowski(2003)] Frankowski, A. 2003, A&A, 406, 265
- [Frankowski & Jorissen(2007)] Frankowski, A., & Jorissen, A. 2007, Baltic Astronomy, 16, 104
- [Frankowski & Tylenda(2001)] Frankowski, A., & Tylenda, R. 2001, A&A, 367, 513
- [Freytag & Höfner(2008)] Freytag, B., & Höfner, S. 2008, A&A, 483, 571
- [Gezer et al.(2015)] Gezer, I., Van Winckel, H., Bozkurt, Z., et al. 2015, MNRAS, 453, 133
- [Gielen et al.(2008)] Gielen, C., van Winckel, H., Min, M., Waters, L. B. F. M., & Lloyd Evans, T. 2008, A&A, 490, 725
- [Gielen et al.(2009)] Gielen, C., van Winckel, H., Reyniers, M., et al. 2009, A&A, 508, 1391
- [Giridhar et al.(2005)] Giridhar, S., Lambert, D. L., Reddy, B. E., Gonzalez, G., & Yong, D. 2005, ApJ, 627, 432
- [Hilditch(2001)] Hilditch, R. W. 2001, An Introduction to Close Binary Stars, by R. W. Hilditch, pp. 392. ISBN 0521241065. Cambridge, UK: Cambridge University Press, March 2001., 392

- [Hillen et al.(2016)] Hillen, M., Kluska, J., Le Bouquin, J.-B., et al. 2016, A&A, 588, L1
- [Homan et al.(2016)] Homan, W., Boulangier, J., Decin, L., & de Koter, A. 2016, A&A, 596, A91
- [Hony et al.(2003)] Hony, S., Waters, L. B. F. M., & Tielens, A. G. G. M. 2003, Planetary Nebulae: Their Evolution and Role in the Universe, 209, 299
- [Hoyle & Lyttleton(1939)] Hoyle, F., & Lyttleton, R. A. 1939, Proceedings of the Cambridge Philosophical Society, 35, 592
- [Huang(1963)] Huang, S.-S. 1963, ApJ, 138, 471
- [Hurley et al.(2000)] Hurley, J. R., Pols, O. R., & Tout, C. A. 2000, MNRAS, 315, 543
- [Hurley et al.(2002)] Hurley, J. R., Tout, C. A., & Pols, O. R. 2002, MNRAS, 329, 897
- [Hut(1981)] Hut, P. 1981, A&A, 99, 126
- [Izzard et al.(2004)] Izzard, R. G., Tout, C. A., Karakas, A. I., & Pols, O. R. 2004, MNRAS, 350, 407
- [Izzard et al.(2006)] Izzard, R. G., Dray, L. M., Karakas, A. I., Lugardo, M., & Tout, C. A. 2006, A&A, 460, 565
- [Izzard et al.(2009)] Izzard, R. G., Glebbeek, E., Stancliffe, R. J., & Pols, O. R. 2009, A&A, 508, 1359
- [Izzard & Jermyn(2018)] Izzard, R., & Jermyn, A. 2018, Galaxies, 6, 97
- [Kama et al.(2009)] Kama, M., Min, M., & Dominik, C. 2009, A&A, 506, 1199
- [Kamath et al.(2014)] Kamath, D., Wood, P. R., & Van Winckel, H. 2014, MNRAS, 439, 2211
- [Kepler et al.(2007)] Kepler, S. O., Kleinman, S. J., Nitta, A., et al. 2007, MNRAS, 375, 1315
- [Kippenhahn et al.(2012)] Kippenhahn, R., Weigert, A., & Weiss, A. 2012, Stellar Structure and Evolution: , Astronomy and Astrophysics Library. ISBN 978-3-642-30255-8. Springer-Verlag Berlin Heidelberg, 2012,

- [Kluska et al.(2012)] Kluska, J., Malbet, F., Berger, J.-P., et al. 2012, Proc. SPIE, 8445, 84450O
- [Kluska et al.(2014)] Kluska, J., Malbet, F., Berger, J.-P., et al. 2014, A&A, 564, A80
- [Kluska et al.(2018)] Kluska, J., Hillen, M., Van Winckel, H., et al. 2018, A&A, 616, A153
- [Lattanzio & Wood(2004)] Lattanzio, J. C., & Wood, P. R. 2004, Asymptotic Giant Branch Stars, 23
- [Lines et al.(2015)] Lines, S., Leinhardt, Z. M., Baruteau, C., Paardekooper, S.-J., & Carter, P. J. 2015, A&A, 582, A5
- [Livio & Soker(1988)] Livio, M., & Soker, N. 1988, ApJ, 329, 764
- [Lovelace et al.(1999)] Lovelace, R. V. E., Li, H., Colgate, S. A., & Nelson, A. F. 1999, ApJ, 513, 805
- [Lovelace & Romanova(2014)] Lovelace, R. V. E., & Romanova, M. M. 2014, Fluid Dynamics Research, 46, 041401
- [Maas et al.(2003)] Maas, T., Van Winckel, H., Lloyd Evans, T., et al. 2003, A&A, 405, 271
- [Maercker et al.(2012)] Maercker, M., Mohamed, S., Vlemmings, W. H. T., et al. 2012, Nature, 490, 232
- [Martinez et al.(2002)] Martinez, P., Kilkenny, D. M., Cox, G., et al. 2002, Monthly Notes of the Astronomical Society of South Africa, 61, 102
- [Mathis et al.(1977)] Mathis, J. S., Rumpl, W., & Nordsieck, K. H. 1977, ApJ, 217, 425
- [Min et al.(2009)] Min, M., Dullemond, C. P., Dominik, C., de Koter, A., & Hovenier, J. W. 2009, A&A, 497, 155
- [Miranda & Rafikov(2018)] Miranda, R., & Rafikov, R. R. 2018, ApJ, 857, 135
- [Monnier et al.(2019)] Monnier, J. D., Harries, T. J., Bae, J., et al. 2019, arXiv:1901.02467
- [Montesinos et al.(2016)] Montesinos, M., Perez, S., Casassus, S., et al. 2016, ApJ, 823, L8

- [O'Keefe(1939)] O'Keefe, J. A. 1939, ApJ, 90, 294
- [Olofsson et al.(1998)] Olofsson, H., Bergman, P., Lucas, R., et al. 1998, A&A, 330, L1
- [Oomen et al.(2018)] Oomen, G.-M., Van Winckel, H., Pols, O., et al. 2018, A&A, 620, A85
- [Podsiadlowski(2001)] Podsiadlowski, P. 2001, Evolution of Binary and Multiple Star Systems, 229, 239
- [Podsiadlowski(2008)] Podsiadlowski, P. 2008, RS Ophiuchi (2006) and the Recurrent Nova Phenomenon, 401, 63
- [Pols et al.(1998)] Pols, O. R., Schröder, K.-P., Hurley, J. R., Tout, C. A., & Eggleton, P. P. 1998, MNRAS, 298, 525
- [Raghavan et al.(2010)] Raghavan, D., McAlister, H. A., Henry, T. J., et al. 2010, ApJS, 190, 1
- [Ramstedt et al.(2014)] Ramstedt, S., Mohamed, S., Vlemmings, W. H. T., et al. 2014, A&A, 570, L14
- [Saladino et al.(2018)] Saladino, M. I., Pols, O. R., van der Helm, E., Pelupessy, I., & Portegies Zwart, S. 2018, A&A, 618, A50
- [Sana et al.(2009)] Sana, H., Gosset, E., & Evans, C. J. 2009, MNRAS, 400, 1479
- [Sandquist et al.(1998)] Sandquist, E. L., Taam, R. E., Chen, X., Bodenheimer, P., & Burkert, A. 1998, ApJ, 500, 909
- [Sawada et al.(1986)] Sawada, K., Matsuda, T., & Hachisu, I. 1986, MNRAS, 219, 75
- [Schwarzschild & Härm(1965)] Schwarzschild, M., & Härm, R. 1965, ApJ, 142, 855
- [Schwarzschild(1975)] Schwarzschild, M. 1975, ApJ, 195, 137
- [Suárez et al.(2006)] Suárez, O., García-Lario, P., Manchado, A., et al. 2006, A&A, 458, 173
- [Szczerba et al.(2007)] Szczerba, R., Siódmiak, N., Stasińska, G., & Borkowski, J. 2007, A&A, 469, 799

- [Taam et al.(1978)] Taam, R. E., Bodenheimer, P., & Ostriker, J. P. 1978, ApJ, 222, 269
- [Taam et al.(1994)] Taam, R. E., Bodenheimer, P., & Rozyczka, M. 1994, ApJ, 431, 247
- [Taam & Bodenheimer(1989)] Taam, R. E., & Bodenheimer, P. 1989, ApJ, 337, 849
- [Taam & Bodenheimer(1991)] Taam, R. E., & Bodenheimer, P. 1991, ApJ, 373, 246
- [Tauris & van den Heuvel(2006)] Tauris, T. M., & van den Heuvel, E. P. J. 2006, Compact stellar X-ray sources, 39, 623
- [Terman et al.(1994)] Terman, J. L., Taam, R. E., & Hernquist, L. 1994, ApJ, 422, 729
- [Terman et al.(1995)] Terman, J. L., Taam, R. E., & Hernquist, L. 1995, ApJ, 445, 367
- [Terman & Taam(1996)] Terman, J. L., & Taam, R. E. 1996, ApJ, 458, 692
- [Thun et al.(2017)] Thun, D., Kley, W., & Picogna, G. 2017, A&A, 604, A102
- [van Winckel(2003)] van Winckel, H. 2003, ARA&A, 41, 391
- [Van Winckel(2018)] Van Winckel, H. 2018, arXiv:1809.00871
- [Van Winckel & Reyniers(2000)] Van Winckel, H., & Reyniers, M. 2000, A&A, 354, 135
- [Vassiliadis & Wood(1993)] Vassiliadis, E., & Wood, P. R. 1993, ApJ, 413, 641
- [Vassiliadis & Wood(1994)] Vassiliadis, E., & Wood, P. R. 1994, ApJS, 92, 125
- [van der Marel et al.(2013)] van der Marel, N., van Dishoeck, E. F., Bruderer, S., et al. 2013, Science, 340, 1199
- [von Helden et al.(2000)] von Helden, G., Tielens, A. G. G. M., van Heijnsbergen, D., et al. 2000, Science, 288, 313
- [Wagner et al.(2018)] Wagner, K., Dong, R., Sheehan, P., et al. 2018, ApJ, 854, 130
- [Waters et al.(1992)] Waters, L. B. F. M., Trams, N. R., & Waelkens, C. 1992, A&A, 262, L37

- [Whitelock et al.(2000)] Whitelock, P., Marang, F., & Feast, M. 2000, MNRAS, 319, 728
- [Wittkowski et al.(2017)] Wittkowski, M., Hofmann, K.-H., Höfner, S., et al. 2017, A&A, 601, A3
- [Woitke et al.(2016)] Woitke, P., Min, M., Pinte, C., et al. 2016, A&A, 586, A103
- [Yorke et al.(1995)] Yorke, H. W., Bodenheimer, P., & Taam, R. E. 1995, ApJ, 451, 308
- [Zahn(1977)] Zahn, J.-P. 1977, A&A, 57, 383
- [Zorotovic et al.(2010)] Zorotovic, M., Schreiber, M. R., Gänsicke, B. T., & Nebot Gómez-Morán, A. 2010, A&A, 520, A86

**Department of Physics and Astronomy**

Celestijnenlaan 200d - bus 2412

3001 Leuven, Belgium

tel. +32 16 3 27124

[www.kuleuven.be](http://www.kuleuven.be)

